UNIVERSIDADE FEDERAL DO CEARÁ
CENTRO DE TECNOLOGIA
DEPARTAMENTO DE ENGENHARIA DE TELEINFORMÁTICA
PROGRAMA DE PÓS-GRADUAÇÃO EM ENGENHARIA DE TELEINFORMÁTICA

GABRIEL CARLINI MONTE DA SILVA

BEYOND THE WIRED BACKHAUL: A SYSTEM-LEVEL PERSPECTIVE OF HETEROGENEOUS NETWORKS WITH WIRELESS BACKHAUL FOR 5G AND BEYOND

FORTALEZA
2024

GABRIEL CARLINI MONTE DA SILVA

BEYOND THE WIRED BACKHAUL: A SYSTEM-LEVEL PERSPECTIVE OF HETEROGENEOUS NETWORKS WITH WIRELESS BACKHAUL FOR 5G AND BEYOND

Dissertação apresentada ao Curso de Mestrado em Engenharia de Teleinformática da Universidade Federal do Ceará, como parte dos requisitos para obtenção do Título de Mestre em Engenharia de Teleinformática. Área de concentração: Sinais e Sistemas

Orientador: Prof. Dr. Victor Farias Monteiro

Coorientador: Prof. Dr.-Ing. Tarcisio Ferreira Maciel

FORTALEZA
2024

Dados Internacionais de Catalogação na Publicação
Universidade Federal do Ceará
Sistema de Bibliotecas
Gerada automaticamente pelo módulo Catalog, mediante os dados fornecidos pelo(a) autor(a)

S58b Silva, Gabriel Carlini Monte da.
Beyond the wired backhaul: a system-level perspective of heterogeneous networks with wireless backhaul for 5G and beyond / Gabriel Carlini Monte da Silva. – 2024.
87 f. : il. color.

Dissertação (mestrado) – Universidade Federal do Ceará, Centro de Tecnologia, Programa de Pós-Graduação em Engenharia de Teleinformática, Fortaleza, 2024.
Orientação: Prof. Dr. Victor Farias Monteiro.
Coorientação: Prof. Dr. Tarcisio Ferreira Maciel.

1. Integrated access and backhaul. 2. Network-controlled repeater. 3. Reconfigurable intelligent surface. 4. Unmanned aerial vehicle. 5. Wireless backhaul. I. Título.

CDD 621.38

GABRIEL CARLINI MONTE DA SILVA

BEYOND THE WIRED BACKHAUL:
A SYSTEM-LEVEL PERSPECTIVE OF HETEROGENEOUS NETWORKS WITH WIRELESS BACKHAUL FOR 5G AND BEYOND

Dissertação apresentada ao Curso de Mestrado em Engenharia de Teleinformática da Universidade Federal do Ceará, como parte dos requisitos para obtenção do Título de Mestre em Engenharia de Teleinformática. Área de concentração: Sinais e Sistemas

Aprovado em: 19/07/2024.

BANCA EXAMINADORA

Prof. Dr. Victor Farias Monteiro (Orientador)
Universidade Federal do Ceará (UFC)

Prof. Dr.-Ing. Tarcisio Ferreira Maciel (Coorientador)
Universidade Federal do Ceará (UFC)

Prof. Dr. Fco. Rodrigo Porto Cavalcanti
Universidade Federal do Ceará (UFC)

Dr. Arthur Sousa de Sena
University of Oulu

Ao meu pai, à minha mãe,
à minha irmã, à minha namorada.

AGRADECIMENTOS

Essa parte da dissertação será a mais difícil de ser escrita. Toda vez que olho, sempre acho que não representa exatamente o que merece ser dito. Talvez por não ter processado completamente o que significa a conclusão desse ciclo.

Todo fechamento de ciclo ocorre em conjunto com uma grande quantidade de emoções. Emoções essas que foram evoluindo a partir da escolha do futuro programa de mestrado até a finalização dele. Entretanto, há um desses sentimentos que se sobressai, o de gratidão.

Agradeço imensamente ao Prof. Victor Monteiro e ao Prof. Tarcisio Maciel por confiarem em um completo desconhecido, como eu. Agradeço não só pela excelente orientação, mas, principalmente, por todo acolhimento desde o primeiro e-mail que eu enviei e por toda compreensão dos dilemas de um estrangeiro em terras cearenses.

Queria agradecer ao Darlan Moreira e Prof. Diego Sousa pelas várias ajudas computacionais em qualquer horário possível e impossível de se reunir. Apesar de não ter tido uma interação tão direta com Prof. Fco. Rafael Lima, seus comentários e revisões foram importantíssimos para evolução dos trabalhos.

Também agradeço a toda equipe do GTEL, que foi fundamental para conclusão desse trabalho. Em especial, os professores com quem eu tive aula, como Prof. Igor Guerreiro, Prof. Charles Cavalcante e Prof. Walter Freitas, à Livia e à toda equipe do TI. Além disso, as amizades criadas no laboratório foram fundamentais para manter a leveza e a serenidade em momentos de dificuldades, particularmente, as amizades do Ezequias, Raul, Erik e Kenneth.

Agradeço a todas as pessoas próximas a mim que compreenderam a minha decisão de fazer um mestrado fora de Recife. Em especial, gostaria de agradecer a Lucas Soares, Lucas Pontes e Brianne que sempre se mostraram presentes e preocupados comigo mesmo com a distância. Além deles, agradeço a tia Nena, tio Marinho, Ceça, Marilene e Juninho por sempre comemorarem minhas conquistas como se fossem as suas.

Há quatro pessoas que não sei se terei formas materiais e imateriais para conseguir agradecer um dia o quanto elas merecem, por isso dedico esse trabalho a elas. São elas, meu pai, minha mãe, minha irmã e minha namorada. Sem essas pessoas, esse trabalho não existiria. Ao meu pai e à minha mãe, agradeço por todo carinho, preocupação, confiança e apoio que me deram a todo momento. À minha irmã, agradeço por sempre acreditar em mim. À minha namorada, agradeço a presença e o companheirismo inesgotáveis.

Por fim, agradeço ao apoio financeiro e técnico da CAPES e da Ericsson Research ao longo de todo o desenvolvimento desse mestrado.

"Assim falou Zaratustra e prosseguiu seu caminho, pensativo e ainda mais lentamente que antes: pois fazia a si mesmo muitas perguntas e não conseguia facilmente encontrar-lhes resposta."

(Friedrich Nietzsche)

RESUMO

A densificação de redes celulares de quinta geração (5G) tem sido considerada como uma das soluções para mitigar as maiores perdas de propagação presentes na faixa de ondas milimétricas em comparação com o espectro sub-6 GHz. Para isso, redes heterogêneas têm sido implantadas. Três exemplos de novos nós que têm sido considerados são: nós com acesso e *backhaul* integrados (IAB, do inglês *integrated access and backhaul*); repetidores controlados pela rede (NCRs, do inglês *network-controlled repaters*); e superfícies reconfiguráveis inteligentes (RISs, do inglês *reconfigurable intelligent sufaces*). IAB é um nó de decodificação e retransmissão, enquanto NCR é um nó de amplificação e retransmissão. RIS é um dispositivo que manipula ondas eletromagnéticas incidentes usando uma camada de metamaterial. A presente dissertação apresenta uma visão geral sobre esses nós. Eles têm sido implantados com diferentes níveis de mobilidade, por exemplo, fixo, nômade e móvel. Assim, este trabalho também apresenta uma visão geral sobre veículos aéreos não tripulados (UAVs, do inglês *unmanned aerial vehicles*), que podem ser implantados junto com esses nós para lhes dar mobilidade aérea. Além disso, é definido um modelo em nível de sistema que permite uma avaliação de desempenho desses nós. Neste contexto, avalia-se o impacto da implantação destes nós visando melhorar o desempenho de uma rede utilizada para cobrir um evento esportivo ao ar livre. Também avalia-se o impacto em IAB e NCR fixos da mudança do enlace do *backhaul* com linha de visada (LOS, do inglês *line of sight*), para sem linha de visada (NLOS, do inglês *non line of sight*). Por fim, também é analisado o impacto da variação da posição de um NCR tanto no desempenho da célula onde está instalada quanto em células vizinhas devido à interferência causada. Resultados de simulações computacionais mostram a melhoria na razão entre sinal e interferência mais ruído, dos equipamentos de usuários (UEs, do inglês *user equipments*), e na taxa de bits devido à implantação desses nós. No cenário considerado, de forma geral, IAB apresentou o melhor desempenho seguido por NCR e RIS. No entanto, houve situações em que NCR superou IAB devido ao maior nível de interferência causado por este último. Além disso, a implantação destes nós em UAVs também obteve ganhos de desempenho, porém suas limitações energéticas os impediram de alcançar resultados tão bons quanto os alcançados pela sua implantação fixa. A mudança na condição de *backhaul* de LOS para NLOS afetou o desempenho dos nós IAB e NCR fixos. NCR foi o que mais sofreu. Destaca-se assim a importância de um bom planejamento de rede. Caso os nós fixos apresentem más condições de *backhaul*, deverá ser avaliada a implantação de nós UAV. Finalmente, os resultados também mostraram que não necessariamente quanto mais perto um NCR estiver de um UE melhor será o desempenho deste último. Além disso, constatou-se que a interferência causada pelo NCR em células vizinhas pode ser minimizada pelo gerenciamento de feixes do NCR, similar a uma filtragem espacial.

Palavras-chave: acesso e *backhaul* integrados, repetidor controlado pela rede, superfície reconfigurável inteligente, veículo aéreo não tripulado, 5G, cobertura, backhaul sem fio.

ABSTRACT

The fifth generation (5G) of cellular wireless networks incorporated the millimeter waves. One of the drawbacks of these higher frequencies is the severe propagation losses compared to sub-6 GHz spectrum. One possible solution to mitigate that is the network densification, which is the deployment of more nodes in the environment. For this, heterogeneous networks (HetNets) have been deployed. HetNets are different types of nodes beyond traditional next generation node B (gNB). Three examples of new nodes that have been considered are integrated access and backhaul (IAB) nodes, network-controlled repeaters (NCRs) and reconfigurable intelligent surfaces (RISs). IAB is a decode and forward node, while NCR is an amplify and forward node. RIS is a device that manipulates impinging electromagnetic waves using a metamaterial layer. This master thesis presents an overview regarding these nodes. They have been deployed with different levels of mobility, e.g, fixed, nomadic and mobile. Thus, this work also presents an overview regarding unmanned aerial vehicles (UAVs) that can be deployed together with these nodes to give them aerial mobility. Furthermore, a system level model is defined allowing a performance evaluation of these nodes. Moreover, it is evaluated the impact of deploying these nodes aiming at enhancing the performance of a network used to cover an outdoor sport event. It is also evaluated the impact on fixed IAB and NCR of the change on the backhaul link from line of sight (LOS) to non-line of sight (NLOS). This work also analyzes the performance improvement due to deployment of NCR on a given cell and its interference impact on neighbor cells. Simulation results show the improvement in user equipments (UEs)' signal to interference-plus-noise ratio and throughput due to the deployment of these nodes. In the considered scenario, in general, IAB presented the best performance followed by NCR and RIS. However, there were situations where NCR outperformed IAB due to higher level of interference caused by the latter. Moreover, the deployment of these nodes in UAVs also achieved performance gains, however their energy limitations prevented them from reaching results as good as the ones achieved by their fixed deployment. The change in backhaul condition from LOS to NLOS affected the performance of fixed IAB and NCR. NCR was the one which suffered the most. It highlights the importance of a good network planning. If fixed nodes present challenging backhaul conditions, it should be considered the deployment of UAV nodes. Finally, the results also showed that the negative impact on neighbor UEs of receiving interference from NCR signals of other cells was not enough to put them on outage. Besides, this interference can be mitigated by proper NCR beam management.

Keywords: integrated access and backhaul (IAB), network-controlled repeater (NCR), reconfigurable intelligent surface (RIS), unmanned aerial vehicle (UAV), fifth generation (5G), coverage, wireless backhaul.

LIST OF FIGURES

LIST OF TABLES

LIST OF ABBREVIATIONS AND ACRONYMS

3D	three-dimensional
3GPP	3rd generation partnership project
4G	fourth generation
5G	fifth generation
A2A	air-to-air
A2G	air-to-ground
ACK	acknowledge
AF	amplify and forward
AI	artificial intelligence
AoA	angle of arrival
AoD	angle of departure
AR	autoregressive
B5G	beyond 5G
BAP	backhaul adaptation protocol
BD	beyond diagonal
BER	bit error rate
BLER	block error rate
BS	base station
C-link	control link
CBR	constant bit rate
CDF	cumulative distribution function
CN	core network
CNN	convolutional neural network
CP	control plane
CQI	channel quality indicator
CSI	channel state information
CSI-RS	channel state information reference signal
CU	centralized unit
DAG	directed acyclic graph
DF	decode and forward
DFT	discrete fourier transform
DL	downlink
DU	distributed unit
EM	electromagnetic
EPA	equal power allocation
ETSI	european telecommunications standards institute

FD	full duplex
FL	federated learning
Fwd	forwarding
GA	genetic algorithm
gNB	next generation node B
GR	group report
GTEL	Wireless Telecommunications Research Group
HAP	high altitude platform
HD	half duplex
HetNet	heterogeneous network
IAB	integrated access and backhaul
ID	identification
IP	internet protocol
ISD	inter-site distance
LAP	low altitude platform
LOS	line of sight
LSTM	long short-term memory
LTE	long term evolution
MAC	medium access control
MCS	modulation and coding scheme
MILP	mixed integer linear programming
MIMO	multiple input multiple output
MINLP	mixed integer nonlinear programming
MISO	multiple input single output
mmWave	millimeter wave
MRT	maximum ratio transmission
MT	mobile termination
NACK	no acknowledge
NCR	network-controlled repeater
NLOS	non-line of sight
NN	neural network
NOMA	non-orthogonal multiple access
NR	new radio
O2I	outdoor-to-indoor
OAM	Operation and Maintenance
OFDM	orthogonal frequency division multiplexing
PDCP	packet data convergence protocol
PHY	physical
PIN	positive-intrinsic-negative

PPP	Poisson point process
PRB	physical resource block
PSO	particle swarm optimization
PtmP	point-to-multi-point
PtP	point-to-point
QoS	quality of service
RB	resource block
RF	radio frequency
RIS	reconfigurable intelligent surface
RL	reinforcement learning
RLC	radio link control
RR	round robin
RRC	radio resource control
RRM	radio resource management
RSRP	reference signal received power
SDAP	service data adaptation protocol
SDM	space-division multiplexing
SE	spectral efficiency
SIC	successive interference cancellation
SINR	signal to interference-plus-noise ratio
SISO	single input single output
SNR	signal to noise ratio
SSB	synchronization signal block
STAR	simultaneously transmitting and reflecting
TDD	time division duplex
TDM	time division multiplexing
TDMA	time division multiple access
TR	technical report
TS	technical specification
TTI	transmission time interval
UAV	unmanned aerial vehicle
UE	user equipment
UL	uplink
UMa	urban macro
UMi	urban micro
UP	user plane

SUMMARY

1 INTRODUCTION

1.1 Motivation

The ever-growing number of connected devices and data traffic is pushing the boundaries of existing wireless networks. By the end of 2029, the data traffic is expected to achieve 563 exabytes per month [1]. Compared to the data traffic at the end of 2023, i.e., 160 exabytes [1], this represents an increase by a factor of 3.5. One of the reasons for this increase is the widespread adoption of new innovative applications, such as virtual and augmented reality, autonomous vehicle and holographic projection.

To accommodate this increase in data traffic and serve a larger number of user equipments (UEs), the fifth generation (5G) of cellular wireless networks has expanded beyond the already loaded sub-6 GHz spectrum, traditionally used by previous cellular generations and referred as FR1. More specifically, 5G networks have considered a subset of frequencies in the spectrum of millimeter waves (mmWaves) [2], referred as FR2, which includes frequencies from 24.25 GHz to 71 GHz. Furthermore, for beyond 5G (B5G), it is supported to occupy the FR3, that includes frequencies from 7.125 GHz to 24.25 GHz.

One advantage of deploying 5G systems in FR2, compared to FR1, is the larger bandwidth available in FR2. Furthermore, since antenna elements are usually separated by a distance of half-wavelength, it is possible to increase the number of antenna elements in a given antenna array when operating under FR2 frequencies [3]. As a consequence, higher antenna gains with narrower beams can be achieved. However, mmWave spectrum has its own set of challenges. Signal propagation at these frequencies suffers from significant path loss and struggles to penetrate buildings and other obstacles, including foliage and rain [4, 5]. Therefore, a limitation of mmWave band is its smaller coverage range compared with sub-6 GHz spectrum. To address this aspect, network densification with new strategically placed heterogeneous nodes are a viable solution for extending a cell coverage area, reducing inter-site distance and boosting network capacity.

The primary solution to densify the network is to deploy more 5G base stations (BSs), i.e., namely next generation nodes B (gNBs), with fiber-based backhaul. However, building from scratch an entire new wired backhaul infrastructure might not be economically viable. Besides, it takes time, and, in certain locations such as historical areas, trenching may be prohibited [6].

In 3rd generation partnership project (3GPP) long term evolution (LTE) Release 10, wireless backhaul was explored with LTE relay, but it lacked commercial traction [7]. There are also wireless backhaul in popular technologies, such as satellite and microwave point-to-point (PtP)/point-to-multi-point (PtmP), but with low throughput [8]. However, nowadays, it experiences higher interest from a commercial point-of-view, because serving nodes equipped with wireless backhaul were demonstrated as a viable alternative to achieve more than 100 Gbps [9].

Furthermore, it is a flexible solution and has a good cost-effectiveness [10]. Some of the nodes with wireless backhaul that are considered as interesting solutions to replace wired-based backhaul nodes are integrated access and backhaul (IAB) nodes, network-controlled repeaters (NCRs), and reconfigurable intelligent surfaces (RISs) [3].

Regarding an IAB node, it has functionalities similar to a regular gNB, however instead of been connected to the core network (CN) via fiber, it is wireless attached to another network node, which is responsible to provide connectivity to the CN. In other words, not only the access links are wireless but also the backhaul link. IAB nodes started to be standardized by 3GPP in Release 16 [11], where possible architectures, radio protocols, and physical layer aspects were addressed. Some characteristics of the IAB concept are multihop architecture, flexible topology adaptation, dynamic resource sharing, use of multiple input multiple output (MIMO) antenna arrays, and inband transmissions of backhaul and access links, i.e., the backhaul and access links shares the same spectrum resources [6, 12, 13].

Concerning NCRs, they were introduced by 3GPP in Release 18 [14]. NCRs can be seen as an enhancement of traditional radio frequency (RF) repeaters, because it can exchange side control information with its gNB. One of the improvements that NCRs incorporate compared to traditional RF repeaters is a beamforming capability managed by a gNB through a side control link [14]. Furthermore, unlike RF repeater, NCR is fully aware of downlink (DL)/uplink (UL) split in time division duplex (TDD) scheme [15].

With respect to RISs, they are made up of multiple antenna patches that use passive elements to introduce phase shifts to incoming signals [16]. More specifically, they are composed of a metamaterial layer controlled by a gNB. Specifically, the metamaterial is a surface consisting of reflecting elements with electrical thickness in the order of subwavelength of the signal to which it is designed to work with. This allows for programmable control of the wireless environment without requiring powerful amplifiers, making it cost-effective and energy-efficient [17].

To improve performance of the nodes with wireless backhaul, it is expected that these new nodes have a line of sight (LOS) backhaul. This challenge should be handled during the deployment phase. However, in some cases it can be impossible to have a LOS link between a serving gNB and an IAB/NCR/RIS. For example, in urban areas with high buildings and where an IAB/NCR/RIS is deployed some blocks far from its serving gNB, it might not be possible to have a LOS link for the backhaul. To overcome this problem, one envisioned solution is to mount them in unmanned aerial vehicles (UAVs). Another advantage of deploying them in UAVs is to give them mobility. Important to highlight that regarding the standardization, 3GPP has already standardized fixed and mobile IAB nodes, while NCRs for instance can only be fixed and no standardization has been performed regarding RIS.

Finally, few works in the literature have simultaneously addressed these three nodes with wireless backhaul. In [3], the authors call the environment where these technologies will coexist as heterogeneous smart electromagnetic environment. They present an overview of each node, their industrial progress and their standardization status. They also present some insights

of application scenarios. However, they do not present simulation results comparing the nodes' performances. Regarding this aspect, they focus only on RIS. Another work recently published addressing these nodes is [18]. The authors also provide an outlook of each technology. It is presented the recent status of the standardization for IAB and NCR by 3GPP, and presented some reports from european telecommunications standards institute (ETSI) for RIS. However, as [3], [18] does not present any simulation result comparing these nodes with wireless backhaul.

In this context, the main contributions of the present master thesis are summarized in the next section.

1.2 Contributions

- **Overview of IAB, NCR, and RIS**: Their main characteristics are presented, e.g., their architectures and specific features. Furthermore, it is also addressed the different levels of mobility that they support, including the possibility of deployment on UAVs. In this context, a brief overview of UAVs as serving nodes is also presented.
- **Analyses of the impact on served UEs of deploying these nodes in scenarios**: Simulation results are presented to analyze the performance of these nodes when deployed either as fixed nodes or mounted on mobile UAVs. Their performances are compared with that of a scenario where there are only gNBs.
- **Evaluation of the impact of the interference caused by the deployment of these nodes**: It is addressed how the deployment of these nodes impact the system in DL and UL, and which are the most impacted nodes and links.
- **Discussion on the impact of having either LOS or non-line of sight (NLOS) links in the backhaul of IAB and NCR**: It is evaluated the impact that the change from LOS to NLOS causes in the performance of IAB and NCR.
- **Evaluation of the impact on neighbor cells of the interference caused by NCRs**: The interference caused by NCRs on UEs served by neighbor cells is also evaluated. Different NCR positions and values of its amplification gain are considered.

1.3 Organization

Chapters 2, 3 and 4 present an overview of IAB, NCR and RIS, respectively. These chapters mainly focus on the architectures and specific features of these nodes. For example: regarding IAB, chapter 2 presents the network procedures to integrate these nodes in the system; concerning NCR, chapter 3 addresses the side control information exchanged between a serving gNB and its controlled NCR; regarding RIS, chapter 4 presents aspects related to the RIS operation mode. Furthermore, these chapters also present an overview of the literature related to these topics and possible research areas.

Chapter 5 presents an overview of UAVs. The focus is on their use as an aerial BS/relay to serve UEs instead of focusing on UAVs as UEs. A literature review on this topic is presented.

Chapter 6 presents adopted models, and common link and system level concepts that were used in the computational simulations performed in this work. For example: 1) in terms of computational resources, it is presented the simulation toolbox that was used; 2) in terms of 5G new radio (NR) concepts, physical layer aspects are addressed, e.g., measurement metrics and resource allocation strategies.

Chapter 7 considers the scenario of an outdoor sport event and evaluates the UEs' performance improvement due to the deployment of IAB nodes, NCRs or RISs. Two types of deployments are considered for IAB and NCR, i.e., fixed and mounted on mobile UAVs, while RISs was considered only as fixed nodes. It is also analyzed how the interference impacts the entities. Furthermore, the impact of having either a LOS or a NLOS backhaul link for IAB and NCR is also evaluated.

Chapter 8 evaluates the interference on neighbor cells caused by the deployment of NCRs. Different NCR positions and values of its amplification gain are considered.

Finally, the conclusions of this master thesis are summarized in chapter 9.

1.4 Scientific Production

The content of this master thesis has been partially published with the following bibliographic information:

Conference Papers

- **Silva, G. C. M.**; Falcão, E. R. B.; Monteiro, V. F.; Moreira, D. C.; Sousa, D. A.; Maciel, T. F.; Lima, F. R. M.; Makki, B., "*System Level Evaluation of Network-Controlled Repeaters: Performance Improvement of Serving Cell and Interference Impact on Neighbor Cells*". XLI Brazilian Symposium on Telecommunications and Signal Processing (SBrT), 2023.

- **Silva, G. C. M.**; Sousa, D. A.; Monteiro, V. F.; Moreira, D. C.; Maciel, T. F.; Lima, F. R. M.; Makki, B., "*Impact of Network Deployment on the Performance of NCR-assisted Networks*". 19th International Symposium on Wireless Communication Systems (ISWCS), 2024.

Patent

- Monteiro, V. F.; Lima, F. R. M.; Sousa, D. A.; Maciel, T. F.; Moreira, D. C.; **Silva, G. C. M.**; Makki, B., "*Configuring a Repeater According to a Selection of a Communication Type to Use for a Communication Between Devices*". Mar, 2024. PCT/EP2024/055704. Patent Application.

The first part of the first chapter of results will be submitted to publication with the following bibliographic information:

Journal Paper

- **Silva, G. C. M.**; Monteiro, V. F.; Sousa, D. A.; Moreira, D. C.; Maciel, T. F.; Lima, F. R. M., "*Beyond the Wired Backhaul: a System-level Perspective of Heterogeneous Networks with Wireless Backhaul for 5G and Beyond*". (to be summited).

It is worth mentioning that this master thesis was developed under the context of Ericsson/UFC technical cooperation projects:

- UFC.49 - "*Integrated Backhaul and Beam Management in Evolved 5G Access*", December/2020 - November/2022;
- UFC.51 - "*Advanced Radio Access for the Evolution of 5G toward 6G*", December/2022 - November/2024;

in which four technical reports were delivered with the following information:

- **Silva, G. C. M.**; Sousa, D. A.; Monteiro, V. F.; Moreira, D. C.; Maciel, T. F.; Lima, F. R. M., "*NCR Deployment Impact on System Performance*". GTEL-UFC-Ericsson UFC.49. Fourth Technical Report.
- **Silva, G. C. M.**; Falcão, E. R. B.; Monteiro, V. F.; Moreira, D. C.; Sousa, D. A.; Maciel, T. F.; Lima, F. R. M., "*System Level Evaluation of Network-Controlled Repeaters: Performance Improvement of Serving Cell and Interference Impact on Neighbor Cells*". GTEL-UFC-Ericsson UFC.51. First Technical Report.
- **Silva, G. C. M.**; Monteiro, V. F.; Moreira, D. C.; Sousa, D. A.; Paiva, R. V. de O.; Maciel, T. F.; Lima, F. R. M., "*System-Level Performance Evoluation of Fixed and UAV Mounted IAB and NCR*". GTEL-UFC-Ericsson UFC.51. Second Technical Report.
- **Silva, G. C. M.**; Monteiro, V. F.; Sousa, D. A.; Moreira, D. C.; Maciel, T. F.; Lima, F. R. M., "*Beyond the Wired Backhaul: a System-level Perspective of Heterogeneous Network with Wireless Backhaul for 5G and Beyond*". GTEL-UFC-Ericsson UFC.51. Third Technical Report.

2 INTEGRATED ACCESS AND BACKHAUL

The standardization of IAB by 3GPP started as a study item of Release 15 in 2017. In the following 3GPP release, i.e., Release 16, a technical report (TR) [11] was delivered, in 2018, detailing some IAB system level aspects, e.g., topology management for single/multi-hop and redundant connectivity, route selection and optimization, dynamic resource allocation between the access and backhaul links, and high spectral efficiency while also supporting reliable transmission. Later on, in 2020, but still in Release 16, two technical specifications (TSs) started specifying IAB in 3GPP. More specifically, TS 38.300 [2] specified protocol layers and architecture of IAB, while TS 38.174 [19] presented the minimum RF characteristics and minimum performance requirements of NR IAB. In 2021, it was created, in Release 17, a work item entitled "Enhancements to Integrated Access and Backhaul for NR" [20]. The main enhancements were related to: 1) duplexing (IAB was constrained to half duplex (HD) mode, but it envisioned to support full duplex (FD) mode); 2) topology adaptation (procedures for inter-donor IAB node migration to enhance robustness and load balancing); and 3) routing and transport (improve multi-hop latency and congestion mitigation).

In the following, we present more details related to the IAB architecture, the procedure to integrate a new IAB node to the system and the wireless access and backhaul links management.

2.1 IAB architecture

Figure 2.1 illustrates a network where some of the serving nodes have a wireless backhaul. The serving nodes in a system with IAB can be classified into two types: IAB donor and IAB node. The IAB donor, represented by a gray gNB, is connected to the CN by a wired backhaul, while the IAB nodes, illustrated by blue gNBs, are connected to the IAB donor or another IAB node by a wireless backhaul. The UEs, depicted as mobile phones, can be served by both IAB node types.

The IAB network topology can be seen as either a spanning tree or a directed acyclic graph (DAG). The first one forces the child IAB node to have only one parent, while the second one does not have a restriction on the number of parents that serve an IAB node [21].

Figures 2.2 and 2.3 illustrate the protocol stack of user plane (UP) and control plane (CP), respectively. As presented in these figures, an IAB donor can be split in two parts transparent to the served nodes [2]: centralized unit (CU) and distributed unit (DU). As in a regular gNB, on the one hand the CU is responsible for less time-critical radio functionalities. On the other hand, the DU part is responsible for time-critical radio functionalities, such as scheduling and retransmission. This split is related to the possibility of deploying both parts in different geographical positions. For example, the DU close to the served nodes in order to reduce communication delay, and the CU in specific places with higher processing capability.

Figure 2.1 – Illustration of wireless backhaul between IAB donor and nodes in DL.

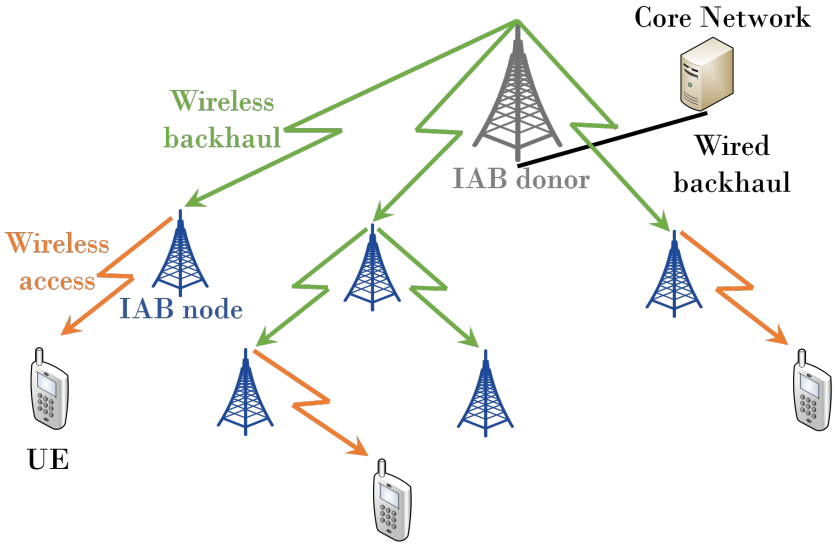

Source: [6].

Figure 2.2 – Protocol Stack - User plane.

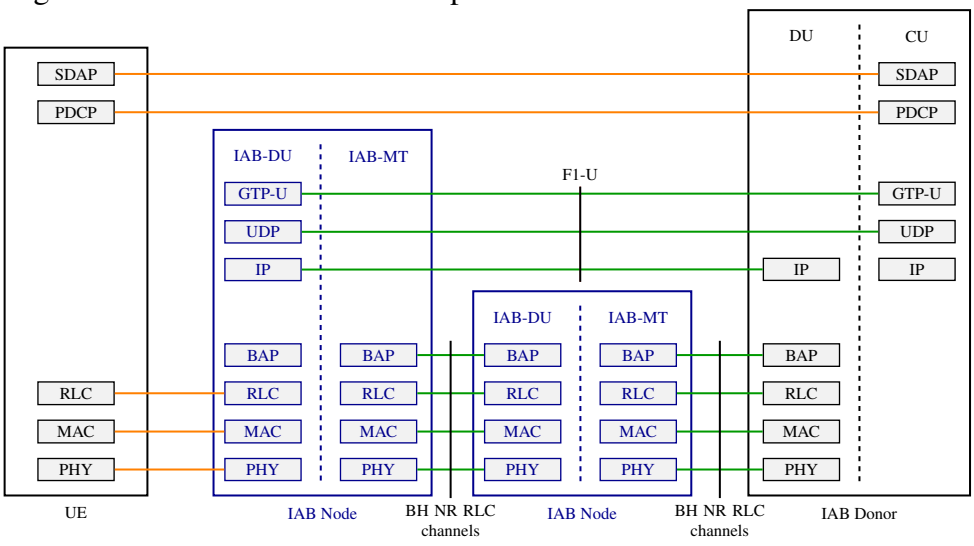

Source: [6].

Regarding their protocols, DU is responsible for lower layers, e.g., physical (PHY), medium access control (MAC) and radio link control (RLC); while CU is responsible for higher layers, e.g., packet data convergence protocol (PDCP) and radio resource control (RRC)/service data adaptation protocol (SDAP).

Regarding the IAB node, it is split in DU and mobile termination (MT). The DU and the MT are responsible for the access and the backhaul links, respectively. From a UE perspective, the DU acts as a regular gNB. From the perspective of an IAB donor, the MT acts as a regular UE.

As illustrated in figures 2.2 and 2.3, the information between the DU part of an IAB node and the CU part of an IAB donor is exchanged via F1 interface [22].

To handle the traffic between an IAB donor and multiple IAB nodes, it was introduced

Figure 2.3 – Protocol Stack - Control plane.

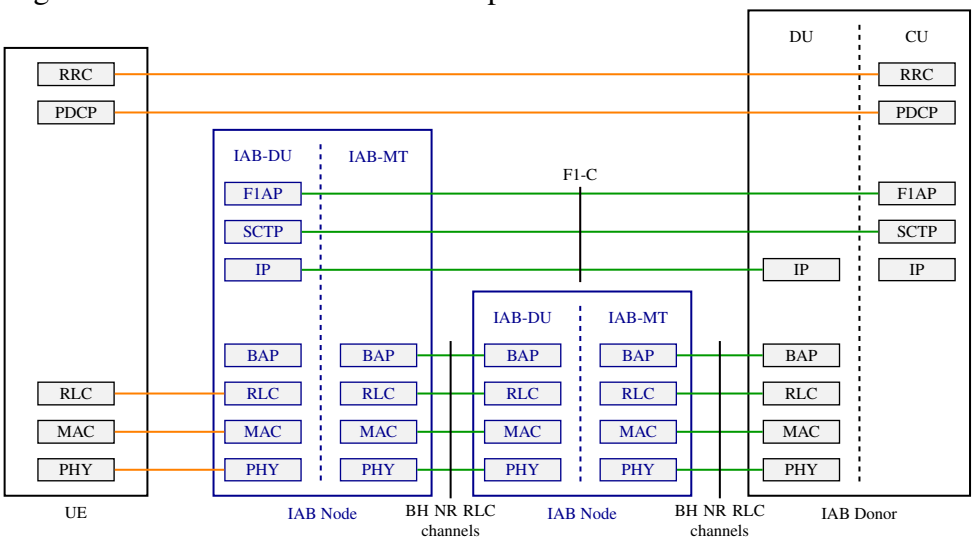

Source: [6].

a new sublayer called backhaul adaptation protocol (BAP) [23]. The IAB donor configures each IAB node with an unique BAP identification (ID) and a routing table that indicates its parent (for UL communication) and possible children (for DL communication). In DL, the IAB donor encapsulates PDCP packets including in the header the BAP routing ID. It consists of the BAP ID of the destination IAB node and the BAP path ID, i.e., the ID of the route that the packet should follow. Similarly, in UL, the header of a packet encapsulated by the BAP layer includes the BAP ID of the destination IAB donor and the BAP path ID.

In the following, we describe the procedure to integrate in the system a new IAB node using the presented protocol stack.

2.2 IAB node integration

Figure 2.4 illustrates the main steps to add an IAB node under a new IAB donor. This integration procedure is presented in more details in [24]. In the first step, the new IAB node sweeps the area to find a possible parent IAB. When it finds one, similar to a regular UE, the MT part of the IAB node set up an RRC connection with the CU of the candidate IAB donor to be verified and authenticated by the CN. At this moment, some of its configurations can be updated by the network using the Operation and Maintenance (OAM) functions. In the second step, it is set up the backhaul RLC channel and it occurs the F1 connection between the new IAB node and the candidate IAB donor. If a configuration update was not performed in the previous step with the OAM functions, it can happen now. In the next step, a routing update is performed. More specifically, an internet protocol (IP) address and a BAP ID is allocated to the arriving IAB node. Besides that, the BAP routing ID of all ancestral IAB nodes are reconfigured. At the final step, there is the establishment of an F1 connection between the IAB node DU and IAB donor CU.

Figure 2.4 – Steps of IAB node integration.

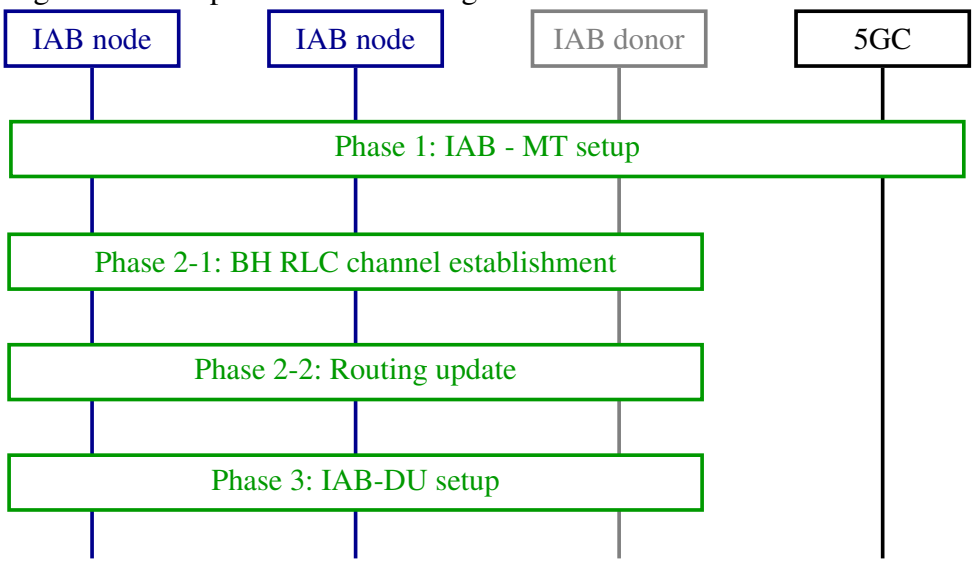

Source: [6].

2.3 IAB spectrum

The wireless backhaul of IAB operates in one of two modes, in-band or out-of-band. In out-of-band backhauling, backhaul and access links are allocated in different frequency bands. As a consequence, they do not interfere with each other.

In in-band backhauling, the same frequency resources are shared between the backhaul and access links. One of the advantages of in-band mode is its higher spectrum efficiency, since bakchaul and access share the same frequency resources. Nevertheless, a drawback of in-band backhauling is the possible self-interference that can occur when the DU part is transmitting and the MT part is receiving, or vice-versa. In order to avoid that, IAB nodes operate in HD mode, it means that DU and MT parts are either receiving or transmitting at the same time, i.e., they can not simultaneously operate in different directions. Moreover, multiplexing techniques, such as time division multiplexing (TDM) and space-division multiplexing (SDM), are recommended to be applied to decrease the impact of interference.

2.4 Literature review

Taking into account the presented technical features of IAB, many works have already investigated different aspects related to this topic. In the following, we present some of them.

An important aspect usually addressed is the impact of IAB node position in the system performance. Some of the works that have evaluated this point are: [13, 25, 26, 27, 28].

In [13], the authors consider a scenario where macro BSs, small BSs, and UEs are distributed by finite homogeneous Poisson point process (PPP) in a limited area. The backhaul link of the small BSs can be via fiber or wireless (in that case, it is an IAB node). Furthermore, the IAB network was submitted to blockage, tree foliage and rain. The objective of the study is to evaluate if the IAB nodes are able to serve the UEs with at least their minimum required

rate. Even when the deployment of IAB nodes was not optimized for reaching their maximum performance, they were able to achieve similar performance as a scenario with fiber-connected gNBs.

The study in [27] evaluates the same metric as the work in [13]. However, the aim of [27] is to optimize the deployment of IAB nodes considering a set of constraints, e.g., minimum inter-IAB node distance.

In [25] and [28], genetic algorithms (GAs) are utilized to place IAB nodes. The authors from [25] consider a scenario with temporary blockages and optimize via GA the IAB position to increase the service coverage probability. In [28], the authors study the cost-benefit between a scenario with only macro BSs and another with small BSs, like IAB nodes.

Another topic related to IAB systems is topology adaptation/routing. It is addressed in [21, 29, 30, 31]. The authors of [21] compare two types of path selection policies, i.e., highest-quality-first and wired-first. The highest-quality-first policy chooses as parent node the candidate BS with the highest signal to noise ratio (SNR), while the wired-first policy prefers choosing a fiber-connected BS, i.e., an IAB donor, instead of another IAB node, even if the IAB donor provides a channel link worse than the one provided by another IAB node. The advantage of the first strategy is the choice of top-notch backhaul links, while the second one reduces the number of intermediary hops. The paper shows that, in the considered scenario, the wired-first policy outperforms the other strategy in terms of latency.

In [29] and [30], the authors of both papers propose algorithms for topology adaptation and routing in the perspective of load balancing. They compare their proposals with existing solutions. In [29], the proposed solution is based on packet queue's length and uses graph theory to optimize the IAB network. The scenario varies the number of UEs, the data rate requirements of the UEs and mobility. The proposed algorithm increases the average throughput and the percentage of satisfied UEs. In [30], the algorithm aims at optimizing the trade-off between spectral efficiency and load balancing. It is evaluated through system level simulation with different amounts of UEs. In heavy data loading, the proposed solution outperforms the system rate in comparison with the other methods. For light data loading, all solutions have similar results.

The objective of [31] is to perform topology adaptation minimizing the end-to-end latency of a packet. It is considered an in-band IAB network with HD mode. The authors proposed a policy based on a Markov decision process that optimizes the longest route of the network. The proposed policy solution presents stable low latency in low to medium traffic conditions.

A third topic usually addressed by state-of-the-art IAB works is the in-band resource allocation of access and backhaul links. Examples of works addressing this topic are [32, 33, 34, 35, 36, 37].

In [33], the authors formulate a problem of spectrum resource allocation with the aim of maximizing the sum log-rate of all UE groups. Due to the challenge of finding a solution for a mixed integer nonlinear programming (MINLP) problem, they propose a deep reinforcement

learning method to reach real-time spectrum allocation satisfying the system requirements. The authors show that the proposed solution outperforms a static allocation strategy.

In [34], the authors' goal is to maximize the rate of the UEs. For this, they propose optimal and suboptimal algorithms to multiplex the UEs in frequency and space. They consider a power constraint scenario. The authors conclude that the optimal and the suboptimal algorithms have similar performance in the considered scenario.

The objective of [37] is to simultaneously solve three problems where the scenario has mobile IAB nodes. The problems are: 1) define IAB nodes positions; 2) define UE-IAB association; 3) in-band resource allocation of backhaul and access links. To solve them, the authors propose a two-level hierarchical multi-agent learning, i.e., a type of reinforcement learning (RL), which increases the sum of UEs' rate in up to 3.5 fold.

3 NETWORK CONTROLLED REPEATER

In previous generations of wireless cellular telecommunications, e.g., the fourth generation (4G), RF repeaters were used to improve the network coverage. An RF repeater works as an amplify and forward (AF) relay. On the one hand, since it does neither decode nor process the forwarded signal, the introduced latency can be disregarded. Moreover, it is a low-cost equipment with easy deployment. On the other hand, the lack of signal processing capability causes the forwarding of non-desired signals, i.e., interference signals [14, 15]. Furthermore, an RF repeater is not able to perform adaptive beamforming towards UEs [38].

In 3GPP Rel-18, a new type of repeater, called NCR, was standardized aiming at overcoming the drawbacks of traditional AF repeaters. NCR (also known as smart repeater) is an evolution of the traditional RF repeater. It can be controlled by the network via side control information. This capabillity allows it to operate with spatial diversity via beamforming controlled by the network [14, 39].

Besides the fact that NCRs operate as AF repeaters, while IAB nodes operate as decode and forward (DF) relays, there are other differences between them. For example, on the one hand, NCR was standardized to be deployed as a stationary single-hop node. On the other hand, IAB can operate as a mobile node in a multi-hop deployment. NCR is transparent for UE, while IAB node not [14].

Figures 3.1 and 3.2 present the RF repeater and NCR protocol stacks, respectively. The user plane protocol stack of RF repeater and NCR are similar, as can be seen in figures 3.1 and 3.2a. However, their control planes are different. As illustrated in figure 3.2b, there is a logical link between the gNB and the NCR through the PHY layer, which is not the case of the RF repeater (figure 3.1). It is through this link that side control information is exchanged between the gNB and the NCR in order to allow the gNB to control the NCR behavior.

3.1 NCR architecture

A NCR can be split into two functional entities, i.e., NCR-MT and NCR-forwarding (Fwd), as shown in figure 3.3. Similar to the IAB-MT part, the NCR-MT entity is used to communicate with its controller gNB through side control information exchange. This communication occurs via control link (C-link), through the NR Uu interface. The side control information is used to control the actions of NCR-Fwd. Regarding the NCR-Fwd, it is responsible for amplifying and forwarding the RF signals between a gNB and its serving UEs.

A common NCR deployment consists of having at least two antenna arrays, where one is responsible for receiving/transmisting control and bakhaul links, and another is responsible for the access links.

The next section presents information that can be exchanged through the side control

Figure 3.1 – RF repeater protocol stack (user and control plane).

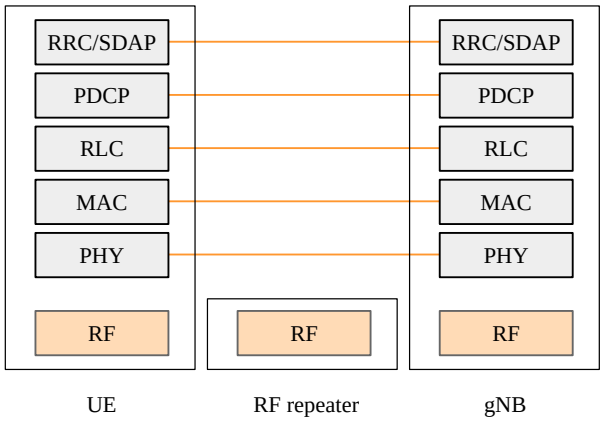

Source: Created by the author.

Figure 3.2 – NCR protocol stack.

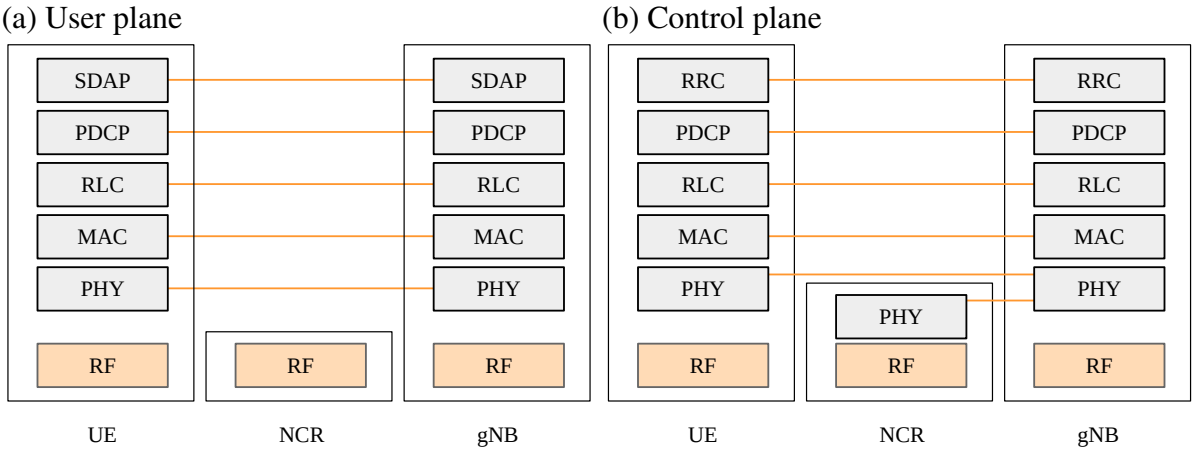

Source: Created by the author.

link, such as beamforming information, timing information, information on UL-DL TDD configuration and ON-OFF information [18]. These side control information are responsible for managing the NCR-Fwd functionalities.

3.2 Side control information

3.2.1 Beamforming information

Traditional RF repeaters perform omnidirectional transmissions, interfering with non-desired UEs and serving a target UE with less power than it could. In this context, the NCR capability of beamforming a transmission helps it to compensate the severe losses in mmWave. The configuration related to how beamforming a given signal is sent by the controller gNB through the side control information.

The way how a beam can be configured for the access link or for backhaul/control link varies. For the backhaul and control links, there are two possibilities, fixed and adaptive beamforming, due to the stationary characteristic of NCR. When NCR-MT and NCR-Fwd operate in the same frequency band, their large scale channel properties are similar. In this case, the

Figure 3.3 – NCR architecture.

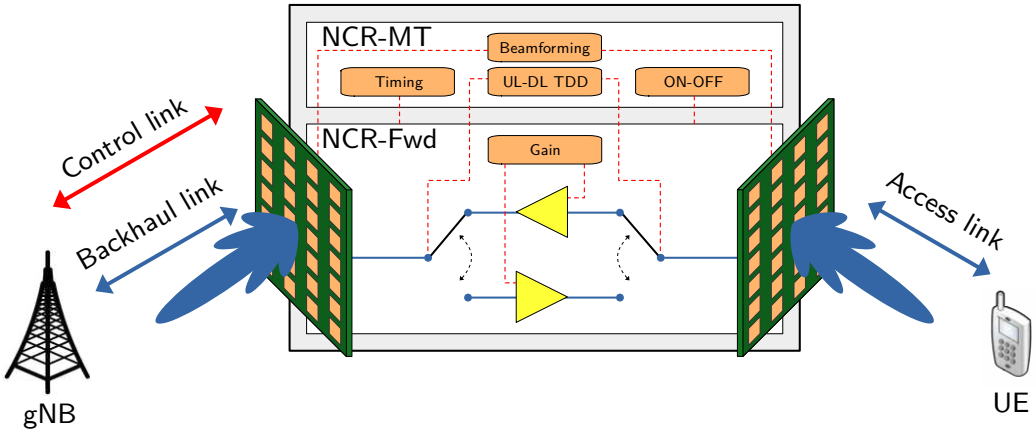

Source: Created by the author based on [18].

Figure 3.4 – Beam indication for access link.

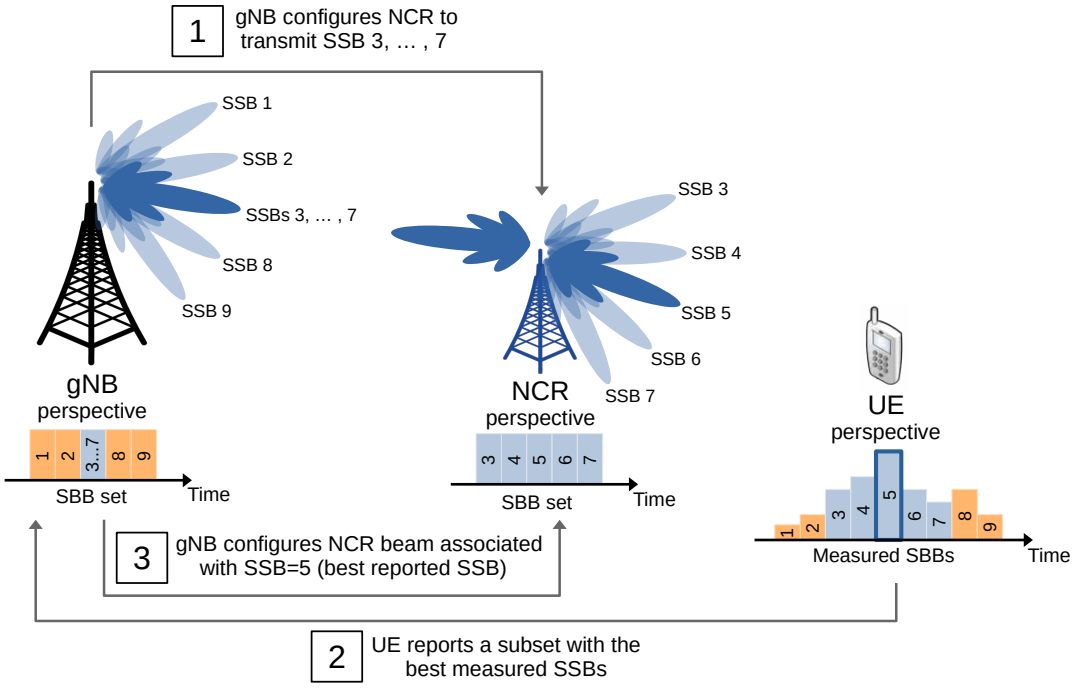

Source: Created by the author.

control link channel state information (CSI) can also be extrapolated for the backhaul link.

Concerning the access link, the identification of which beam to use can be dynamic or semi-static. On the one hand, the dynamic indication is preferable in situations where it is necessary a rapid adaptation of beamforming, e.g., due to UE mobility. On the other hand, the semi-static indication is preferable when not so often beamforming adaptation is required.

Figure 3.4 illustrates an example of how UE connects to gNB through NCR. In this example, the gNB has a set with nine synchronization signal blocks (SSBs). Four of them, i.e., SSBs 1, 2, 8 and 9, are sent in four different directions, while the remainder, i.e., SSBs 3 to 7, are transmitted in the same direction, i.e., towards the NCR. Despite the gNB does not completely know the NCR's beams characteristics, the gNB is aware of the number of beams supported by

Figure 3.5 – NCR timing.

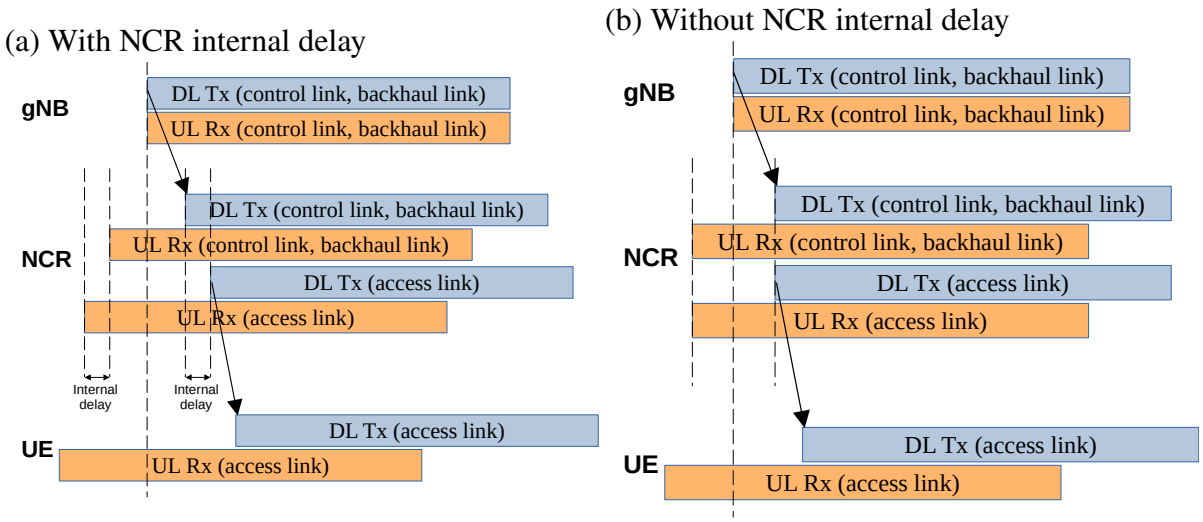

Source: created by the author based on [39].

the NCR. So, at step 1 of figure 3.4, the gNB configures the NCR to forward SSBs 3 to 7 in different directions and time instants. The UE measures the quality of each received SSB and sends a report with the best measured SSBs to the gNB (step 2 of figure 3.4). In this example, the strongest measured SSB was the number 5, which was forwarded by the NCR. Important to highlight, that the UE is not aware that some of the SSBs were amplified and forwarded by the NCR. In other words, the NCR is transparent to the UE. Based on the UE report, the gNB configures the NCR to transmit data through some of its beams. In this example, at step 3 of figure 3.4, the gNB configures the NCR to forward data in the same direction as SSB 5, i.e., the strongest SSB reported by the UE.

3.2.2 Timing information

Figure 3.5 illustrates, the temporal alignment of a communication in DL and UL between a gNB and an UE assisted by a NCR. More specifically, figures 3.5a and 3.5b, respectively, illustrate the cases when the NCR introduces or not a delay to the communication. In situations, as in figure 3.5a, where the NCR internal delay can not be neglected, reception and transmission must take this delay into account in order to avoid, e.g., interference between in sequence transmissions. The NCR is then configured by its controller gNB with timing information via the C-link [39].

3.2.3 Information on UL-DL TDD configuration

C-link is also used to configure the NCR with a TDD scheme. NCR supports semi-static TDD DL/UL for access, backhaul, and control links to reduce the signaling. The DL/UL TDD configuration is the same for access and backhaul links [39].

3.2.4 ON-OFF information

ON-OFF information is sent to NCR for turning on/off the NCR-Fwd part. The main goals of this functionality is to save power and to mitigate the interference in the environment improving the network performance. The default mode is assumed to be OFF. It stays in this state until a different gNB indication [14].

3.3 Literature review

In the following, we present some state-of-the-art works that have addressed different aspects related to NCR.

In [39], the authors present an overview on NCR. They discuss general aspects related to side control information. Furthermore, they bring forth a deliberation regarding 4 mechanisms for NCR identification and authentication. It is analyzed the performance of 3 scenarios. The scenarios are: 1) macro only; 2) macro + RF repeater; and 3) macro + NCR. The authors consider the impact of beam information on NCR's performance in relation to the other cases. They conclude that NCR has a superior performance.

The authors from [40] also provide an introduction about NCR. They discuss the main specifications of NCR in 3GPP Rel-18 and the challenges of NCR-assisted network, such as lack of testbed and cost-efficiency trade-off between IAB and NCR. Furthermore, two scenarios with different numbers of gNBs and NCRs are analyzed and compared. They conclude that depending on the characteristics of the scenario the introduction of NCR can improve the performance specially on UL and of cell-edge UEs.

In [41],[42],[43], the authors compare NCR and RIS from different perspectives. In [41], models using mixed integer linear programming (MILP) are proposed to maximize the reliability of network based on the considered scenario, position and configurations of NCR and RIS. In [42], NCR and RIS coverage are compared in realistic urban environments from physical layer perspectives. According to the authors, RIS is preferable for open areas, despite its lower capacity, while NCR is more suitable to narrow scenarios, e.g., roads. NCR and RIS are also compared in [43]. The authors take into account a NCR with and without power constraint for different values of its amplification gain, while for RIS, two algorithms of the passive beamforming are considered. Furthermore, hardware impairments for RIS are also considered. The authors show that NCR outperforms RIS in all scenarios and RIS with hardware impairments is the worst scenario.

In [44], it is proposed a NCR with two panels in access link. The authors' objective is to optimize a multi-user precoder to maximize the number of served UEs. Constraints on the number of time-frequency resources and on the value of the minimum required rate per UE are considered. According to the presented simulation results, in comparison with NCRs with only one antenna array in the access, the authors' proposal doubles the spectral efficiency (SE) and the number of served UEs.

The authors from [45] study the problem of beam squinting in NCR from a link and system level perspective in a MIMO scenario. It is considered that signaling and data transmission occur in different subbands. In this context, it is proposed a compensation method for NCR in order to avoid beam squinting due to the configuration of the NCR to transmit in a given subband based on measurements performed in another subband. The authors analyzed three situation: 1) different subbands for control and data plane without compensation; 2) different subbands for control and data plane with compensation; and 3) same subbands for control and data plane. The results show that, with the proposed compensation method, the NCR is able to perform as good as if control and data transmission happened in the same subband.

4 RECONFIGURABLE INTELLIGENT SURFACE

Up to this moment, 3GPP has not started a study item focused on RIS. There was an expectation that a study item would be discussed in Releases 18 and 19, however this possibility was not confirmed. In 2023, it was formulated by the ETSI a group report (GR) which deliberates about several aspects related to RISs, such as deployment scenarios, architectures, and communication model [16, 46, 47].

RIS emerged as a new paradigm for communication nodes. Unlike traditional nodes, RIS can dynamically or semi-statically manipulate electromagnetic (EM) properties of an incident wave. For this, a RIS is made of a thin metamaterial layer, which can be controlled by a gNB to reflect the incident wave in a desired direction. This allows to create a LOS link where there is not one. The metamaterial surface is a mixture of artificial materials, whose properties can be modeled. In the RIS context, these properties can be electronically tuned via coupled devices such as positive-intrinsic-negative (PIN) diodes or varactor diodes [17]. This allows to control reflection, refraction, absorption, or any combination of these effects. In a RIS default deployment, this control is performed by the gNB. However, a RIS is also envisioned to have a standalone deployment, where the RIS controller is integrated with the own RIS. The RIS transforms the wireless environment from a passive entity into a programmable intelligent agent. Furthermore, it is built of passive components with scattering capacity, known as unit-cells. This approach enables programmable control without resorting to high-power amplification, resulting in a cost-effective and energy-efficient design [16].

More specifically, a gNB controls the RIS to optimize signal propagation. It gathers data from the RIS and the UE to estimate their channels and computes the optimal beamforming. Based on this estimate, the gNB configures the RIS to adjust its properties in order to improve system performance. It is worth emphasizing that, in this RIS management, the gNB is responsible for the data processing, while the RIS only applies the instructions received via control signal. This lack of necessity of a processing unit at the RIS makes it cheaper to be produced.

RIS operational mode can be classified based on how it interacts with the incident waves, e.g., reflects, refracts, absorbs or backscatters. In the following we describe some of these operational modes [16]:

- Reflection mode empowers the surface to regulate the reflection behavior of EM waves. Notably, this enables decoupling the reflected and incident angles, unlike typical scenarios. This mode is typically envisioned to be used on RIS deployed on building facades.

- Refraction mode bends impinging EM waves in a way that defies Snell's law, allowing them to refract in other directions. This capability is particularly useful for outdoor-to-indoor (O2I) applications. By replacing traditional glass windows by RISs operating

Figure 4.1 – Same beamforming in TDD DL/UL in RIS communication between gNB and UE.

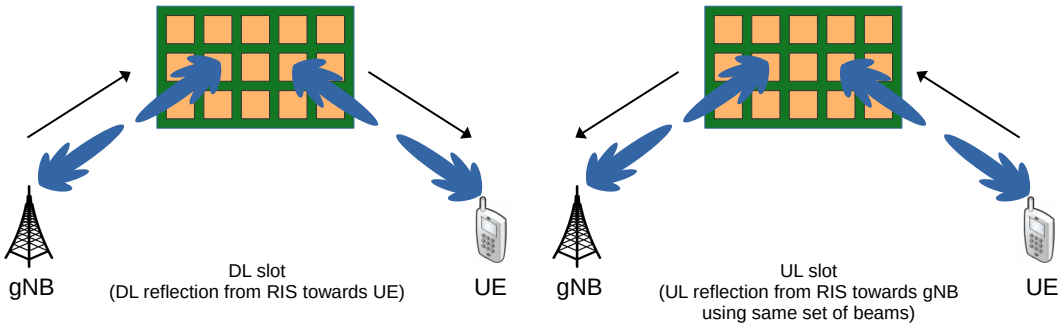

Source: Created by the author based on [16].

in refraction mode, signal strength can be enhanced within buildings.

- Absorption mode ideally isolates an area so that minimum information leaks out to another area due to the absorption and no reflection by the RIS of a certain carrier and bandwidth of impinging signal.

- Backscattering mode is used to perform a diffuse reflection compared to the reflection mode, where the incoming wave is reflected to an exact location. This mode is useful to serve a larger area.

In this work, it is considered the reflection mode.

Regarding duplexing mode, RIS operates in TDD. Due to channel reciprocity between DL and UL, RIS may preserve the same beam configuration. Thus, as illustrated in figure 4.1, in a DL slot, the signal transmitted by a BS hits the RIS in a given beam direction and is reflected by the RIS to an UE in another beam direction. When operating in an UL slot, the communication direction changes. The incident signal comes from the UE in a given beam direction and is reflected by the RIS in another beam direction towards the BS. Important to mention that channel reciprocity may not occur and the beam configuration in DL and UL may be independent [16].

4.1 RIS architecture

As illustrated in figure 4.2, RIS can be divided in two parts, i.e., RIS controller and RIS panel. The RIS controller dynamically adjusts the properties of its unit cells to manipulate incoming EM waves based on control signals received from the network. The RIS panel consists of an array of unit-cells that can manipulate various properties of the incident signal, such as frequency, amplitude, phase and polarization.

The RIS panel is composed by multiple layers with different functions. Figure 4.2 illustrates a simple model with 3 layers. The inner layer embeds a control circuit that is connected to the RIS controller. The RIS controller supplies power to the circuit and manages its response, enabling the outer layer's unit cells to interact with EM waves in a specific way. The middle layer

Figure 4.2 – RIS architecture.

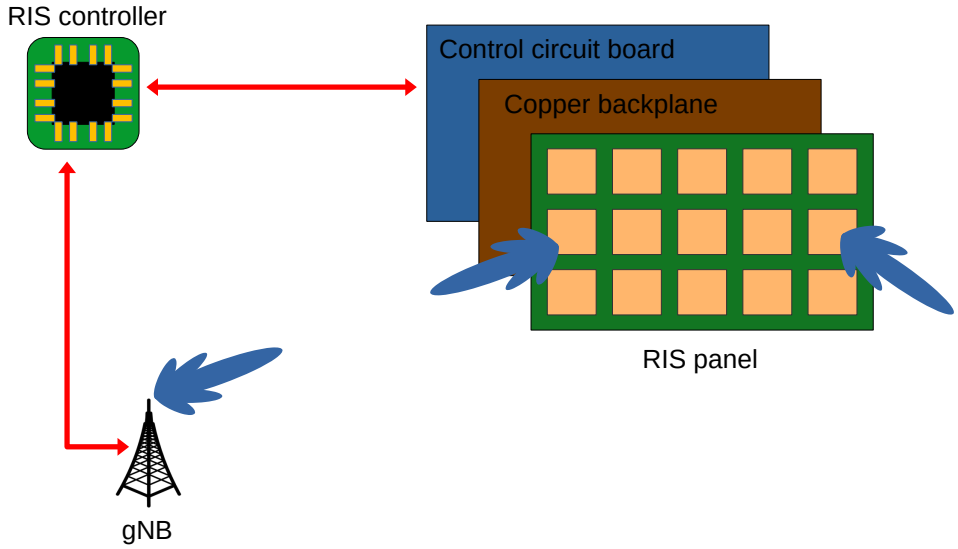

Source: Created by the author.

Figure 4.3 – RIS single-connected structure with 4 elements.

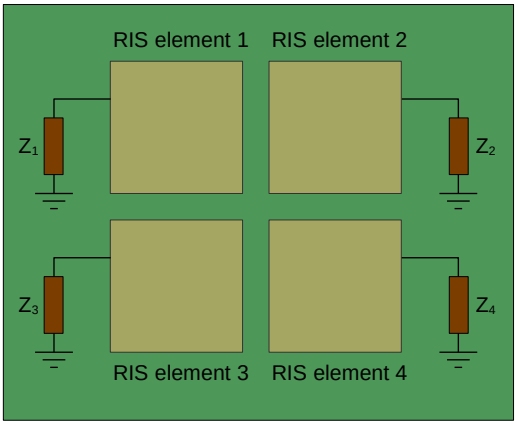

Source: Created by the author.

acts as a shield, preventing unwanted signal leakage through the RIS. Copper is typically used for this layer. Finally, the outermost layer consists of an array of metallic elements [46].

As it can be seen in figure 4.3, the design where each unit-cell of a RIS connects to a single impedance unit is called single-connected structure. Consider a RIS with N elements where element i is connected to an impedance Z_i. These impedances are responsible for determining the complex reflection coefficients θ_i, which $\|\theta_i\| \in \{0,1\}$, of the elements whose the incident signal is going to be reflected. The reflection coefficients θ_1, θ_2, ..., θ_N are based on Z_1, Z_2, ..., Z_N. The set of θ's are arranged in a diagonal matrix $\mathbf{\Theta}$, called reflection matrix, i.e., $\mathbf{\Theta} = \text{diag}(\theta_1, \theta_2, \ldots, \theta_N)$.

4.2 RIS path loss

Consider a far-field scenario where the transmitter and receiver are so far apart that the initially spherical wave essentially transforms into a plane wave as it approaches the receiver.

The separation between transmitter and receiver must exceed a distance equal to the radius R of a sphere centered at the transmitter antenna, with

$$R = \frac{2L^2}{\lambda}, \tag{4.1}$$

where L is the diameter of the smallest sphere that encloses the antenna and λ is the wavelength.

According to [47] and [48], a signal that is reflected by the RIS suffers with a path loss in far field given by

$$PL_{farfield} = \frac{64\pi^3 (d_1 d_2)^2}{G_t G_r G M^2 N^2 d_x d_y \lambda^2 F(\theta_t, \mu_t) F(\theta_r, \mu_r) A^2}, \tag{4.2}$$

where G_t and G_r are the transmitter and receiver gain; G is the scattering gain of a single RIS element; M and N represent the number of RIS elements in row and column, respectively; d_x and d_y are the width and length of a RIS element, respectively; θ_i and μ_i, where $i \in t, r$, are the elevation and azimuth angles from RIS to transmitter and receiver, respectively; $F(\theta_t, \mu_t)$ and $F(\theta_r, \mu_r)$ are the normalized radiation pattern of RIS element to transmitter and receiver, respectively; and $A \in [0, 1]$ is the maximum gain of the RIS. Finally, d_1 and d_2 represent the distance from the RIS to transmitter and receiver, respectively.

It is worth to highlight that the path loss in far field is proportional to $(d_1 d_2)^2/\lambda^2$, instead of $(d_1 d_2)^2/\lambda^4$. This implies that frequency-related effects only influence one of the two links, gNB-RIS or RIS-UE.

4.3 Literature review

The RIS researches are conducted across several areas. This section will explore some of these research topics and provide a brief overview of relevant papers.

One of the first investigated topics related to RIS was channel estimation. Some works that investigated this topic are [49, 50, 51, 52, 53].

In [49], researchers investigate a MIMO communication system aided by RIS, considering various physical imperfections like hardware-induced phase shift variations. They propose two tensor-based channel estimation algorithms using parallel factor analysis and analyze their computational complexity.

The authors of [50] highlight two critical limitations of many existing channel estimation algorithms: 1) their computational complexity increases rapidly with the number of RIS elements; 2) and they consider specific matrix structures. To address these limitations, they propose a novel algorithm based on unitary approximate message passing. The proposed algorithm is linearly proportional to the number of RIS elements. Besides, it does not depend on specific matrix structures.

In [51], it is proposed a deep learning strategy to estimate the angle of arrival (AoA)/angle of departure (AoD) to maximize the received power of a pilot transmitted with beamforming in time-varying mmWave system.

The authors from [53] propose a channel estimation based on convolutional neural network (CNN) and autoregressive (AR) predictor. Their solution is analyzed in a RIS-assisted multi-user MIMO with correlated fast-fading channel. The results show that their framework achieves a high prediction accuracy and an improvement in SE with a reduction on pilot overhead.

Another topic well investigated related to RIS is beam design and beam selection. Some of the works that address it are [54, 55, 56, 57]. The paper [57] is a survey about beamforming design in RIS-assisted wireless communication. It identifies research gaps and proposes new directions for future exploration.

In [54], it is considered a RIS-assisted multiple input single output (MISO) communication with single UE. The authors propose a low complexity adaptive beam selection scheme which: 1) employs two sub-optimal beamforming vectors for the transmitter; 2) calculates the RIS beamforming; and 3) selects the solution that maximizes the received signal strength.

The authors of [55] consider the problem of maximizing the sum-rate of all UEs in a MISO communication with multiples UEs in a RIS assisted network. They propose two solutions: a three-step convex optimization and a neural network (NN) scheme.

RIS channel modeling is addressed in [48, 58, 59, 60, 61]. In [48], it is formulated a closed-form expression for free-space path loss models in RIS-assisted single input single output (SISO) communication. Some aspects that are analyzed are the far-field and near-field beamforming. To validate their theoretical findings, they present measurements performed during an experiment in an anechoic chamber with three RISs.

In [58] and [60], RISs are deployed in mobile UAVs. Both works study the channel statistics in the considered scenario.

In [61], it is introduced a new method for calculating the scattered electric field generated by a RIS considering the mutual coupling of the unit-cells. The calculated scattered fields can also be integrated with ray tracing techniques to model wave propagation in real-world environments with multipath where RIS elements are deployed.

It is important to highlight that RIS is a huge area with different topics. Some of them are simultaneously transmitting and reflecting (STAR)-RIS [62], liquid-crystal RIS [63] and beyond diagonal (BD)-RIS [64]. This literature review do not have the intention to encompass all of them.

5 UNMANNED AERIAL VEHICLE

Recent years have seen a growth in UAV applications spanning different areas, e.g., delivery services, rescue, surveillance, military operations and telecommunications [65]. This rise in interest stems from UAVs' inherent advantages: rapid three-dimensional (3D) deployment, maneuverability and flexibility, which are qualities unmatched by traditional ground-based networks.

UAVs can function in one of two primary modes: aerial BS/relays or aerial UE. In the aerial BS/relay scenario, the goal is to provide reliable, fast-deployable, and on-demand wireless communication to designated areas. In contrast, aerial UEs are more suited for data collection, delivery tasks and surveillance [66].

Besides the type of operational mode, there are also other ways to classify UAVs. For example, they can be classified according to their altitude of operation [65]. In this class, we can mention at least two categories: low altitude platform (LAP) and high altitude platform (HAP). On the one hand, HAPs operate above 20 km and are quasi-stationary, meaning that they stay in a fixed position for long periods, often months [67]. On the other hand, LAPs fly at lower altitudes, typically up to tens of meters. LAPs are known for their fast deployment and mobility. They are suited for missions lasting several hours.

Beyond altitude, wing design defines another classification of UAVs. Fixed-wing UAVs resemble small airplanes with high speeds but that cannot hover. Rotary-wing UAVs, the most popular type, often take the form of quadcopters with lower speed than fixed-wing models. Rotary-wing UAVs usually can hover.

Recognizing the potential of UAVs, the 3GPP has undertaken extensive studies on UAV integration. TR 22.829 [68] explores UAV support for various applications and scenarios at low altitudes, while TR 36.777 [69] focuses on their integration with LTE networks. Additionally, TR 23.754 [70] and TS 23.256 [71] delve into the mechanisms for UAV identification, tracking, authorization, and authentication.

UAV offers some benefits described in [72, 73]. More specifically, due to their high altitudes, UAVs have a greater chance of establishing LOS links with ground gNB. This translates to more reliable data transmission compared to terrestrial networks with potential signal obstructions. Additionally, if the signal quality deteriorates, an UAV can adjust its position to find a better connection. UAVs boast dynamic deployment capabilities. They can autonomously reposition themselves in the air to meet real-time network requirements. This flexibility fosters a more robust network, adaptable to unexpected changes in signal conditions. In the event of natural disasters that damage ground infrastructure, UAVs can be rapidly deployed to serve affected UEs in the region. Unlike traditional infrastructure like towers and cables, UAVs require no site rentals or extensive setup. Multiple UAVs can be coordinated to form a swarm, significantly expanding network coverage in an area quickly and efficiently. However, it is important to note that UAVs

are best suited as temporary solutions due to battery limitations. This makes them ideal for brief events like sport events or festivals, and natural disasters.

5.1 UAV deployment

In a single UAV deployment scenario, a solitary UAV acts as either a relay or a BS. This UAV is connected to a ground-based BS that maintains control over its operations. To optimize the UAV's positioning within the sky, various performance metrics are considered. These metrics include SNR, throughput, and bit error rate (BER).

In scenarios involving multiple UAVs, these UAVs can self-organize themselves to enhance wireless communication capabilities. Their self-organization can be categorized into four main approaches [66, 73]:

- **Star (or centralized)**: in a star deployment, UAVs establish direct connections with the ground BS via air-to-ground (A2G) links. These UAVs do not directly communicate with each other. Instead, all communication must be routed through the central BS. This centralized approach offers a key advantage: control management is handled by a single powerful node, simplifying management tasks. However, there is a trade-off. Direct communication between UAVs becomes impossible, introducing latency as all data must pass through the BS. Additionally, this reliance on a single central node creates a vulnerability, as any disruption to the BS could damage communication for the entire network.

- **Multi-star (or distributed)**: this network consists of multiple clusters, each organized in a star-like fashion. Unlike a single-star network, each cluster in a multi-star has a designated UAV responsible for relaying communication between other UAVs in the cluster and the ground BS. This creates two types of links: air-to-air (A2A) for communication within the cluster and A2G for communication with the BS. However, a key limitation of this approach is that if the central UAV in a cluster malfunctions, the entire cluster's communication collapses because communication with the BS relies on this intermediary.

- **Mesh**: in this approach, UAVs can directly communicate with each other, and only one UAV needs a connection to the ground BS. The mesh network's flexibility allows for multi-hop routing, where data packets can find the most efficient path to their destination by hopping from one UAV to another. This redundancy also offers self-healing capabilities. If a single UAV fails, the remaining UAVs can automatically reconfigure the network to maintain communication. However, if the UAV, that are communicating with the controlling gNB, fails, the others one can not exchange information with the gNB.

- **Hierarchical mesh**: in this approach, clusters of UAVs are considered and within each cluster a mesh network is configured, allowing for direct communication between UAVs of the same cluster. Only a designated UAV in each cluster can connect with other designated UAVs of other clusters. Furthermore, only some of the UAVs have the capability to directly communicate with the ground BS, what creates the same limitation as multi-star and mesh.

5.2 Literature review

This section explores how UAV research is branching out into various fields and applications. It focuses on the synergy between UAVs and heterogeneous networks (HetNets) with wireless backhaul discussed earlier.

Several research papers explore UAV-IAB integration, including [74, 75, 76, 77]. The authors of [74] analyze the system-level impact of deploying UAV-IAB on the performance of mobile UEs. Their work compares the performance of static and mobile UAV-IAB. The mobility of the UAV-IAB is optimized using a particle swarm optimization (PSO) algorithm, considering three backhaul scenarios: 1) ideal (unlimited bandwidth); 2) backhaul-unaware (limited backhaul bandwidth, but not considered in the optimization); and 3) backhaul-aware (limited backhaul bandwidth, which rate limitation is considered in the optimization). The study evaluates UE throughput and Jain's fairness index for different numbers of deployed UAVs.

In [75], it is considered a public safety mission-critical scenario where the infrastructure of a region fails and an UAV-IAB node is used to cover this area. The UAV-IAB node receives the signal from a BS deployed nearby and operates in mid-band, allowing to cover a larger area compared to transmission at mmWave frequency band. The authors propose a solution based on RL to optimize the UAV-IAB 3D position and its electrical antenna tilt. They also present the required network architecture and signaling procedures to support the deployment of their solution. Their proposal is evaluated through system-level simulations, demonstrating improvements in throughput and reduction in the drop rate of UEs.

In [76], which is an extension of [77], the authors also address the 3D position optimization of UAV-IAB nodes. The proposed solution is based on deep learning and operates in real time taking into account the sharing of resources between fronthaul and backhaul.

To the best of my knowledge, there is currently no published research documenting the mounting of an NCR onto an UAV. This lack of documented applications suggests UAV-NCR technology has great space to be explored.

The works [78, 79, 80, 81] explore the use of RIS mounted on UAV to improve wireless communication performance. In [78], it is proposed a method for optimizing the RIS's phase vector and the allocated bandwidth for each UE using long short-term memory (LSTM) and federated learning (FL). This two-stage process involves the UAV first training a model to predict the phase vector, followed by the RIS controller maximizing the total achievable data rate.

The authors from [79] propose a model that leverages a combination of Q-learning

and Fourier feature mapping for a RIS-mounted UAV system. This model aims to simultaneously optimize the positioning of the UAV-RIS, the transmission beamforming, and the reflection beamforming of the RIS. The overall objective is to enhance the communication quality of service (QoS) and its reliability besides improving its security against eavesdroppers and jammers. The proposed solution maximizes the worst-case secrecy rate.

The study [80] explores integrating either a RIS or a FD relay into an UAV. The key aspect is that the UAV's trajectory optimization considers its remaining onboard energy. This research proposes a joint approach that optimizes both time division multiple access (TDMA) scheduling and the UAV's trajectory. The goal is to maximize the minimum data rate experienced by all served UEs and ensure fairness among them.

In [81], it is used an UAV-RIS to mitigate interference in a scenario where there is communication from ground, air and space. An artificial intelligence (AI)-based scheme calculates the precoders of: the satellite, the terrestrial terminals and the UAV-RIS. Three states of CSI are evaluated: no CSI, instantaneous CSI, and delayed CSI.

In the next chapter, we present common link and system level models allowing to evaluate the impact on system performance of deploying one of the presented nodes, i.e., IAB, NCR and RIS, either fixed on the ground or mounted on mobile UAVs.

6 COMMON LINK AND SYSTEM LEVEL MODELS

The system architecture adopted in this master thesis is based on 3GPP specification releases 15 to 18. Thus, for the sake of completeness, this chapter provides technical insights into some 5G NR features relevant for the understanding of the remaining of this document.

6.1 3GPP working process

3GPP is a global organization responsible for producing technical specifications on cellular telecommunications technologies, encompassing radio access, core network and service capabilities. It is the union of telecommunications industry manufactures, mobile service providers, and research institutions.

The process of technical specification's development is described in the following [82]. Figure 6.1 illustrates a high-level overview of 3GPP working process. In step 1, individual companies or organizations submit their proposals, e.g., early research and development documents, called Contributions. These Contributions propose new technologies for cellular systems. In step 2, there are 3GPP meetings to analyze and debate the Contributions and decide if they are going to be approved. In step 3, the accepted Contributions become one or more Study Items. In the Study Items, it is studied the feasibility on multiple proposed solutions. The result of a Study Item is a TR summarizing the agreed concepts. In step 4, based on the TR, a Work Item is initiated. This stage focuses on implementing features outlined in the TR. Convergence on these implementations leads to the publication of a TS. The TS can be a new specification or an update of an existing one. In step 5, with the published TS in hand, industries and academia can now compete to develop products based on the specifications.

6.2 GTEL's simulation toolbox

The simulation results presented in this master thesis were generated using a private simulation toolbox developed by the Wireless Telecommunications Research Group (GTEL). It is based on 3GPP standardizations. This simulation toolbox is a set of libraries that can be used by researchers to develop their own simulators. This toolbox contains channel models implementations, link adaptation solutions, traffic model implementations, radio resource management (RRM) algorithms, beam management methods, mobility management schemes, and so on.

Its key features for this work are:

- 3GPP channel model. More specifically, it is used an implementation [83] of the 3GPP documents [69, 84]. Some characteristics of the adopted channel model are:

Figure 6.1 – 3GPP working process.

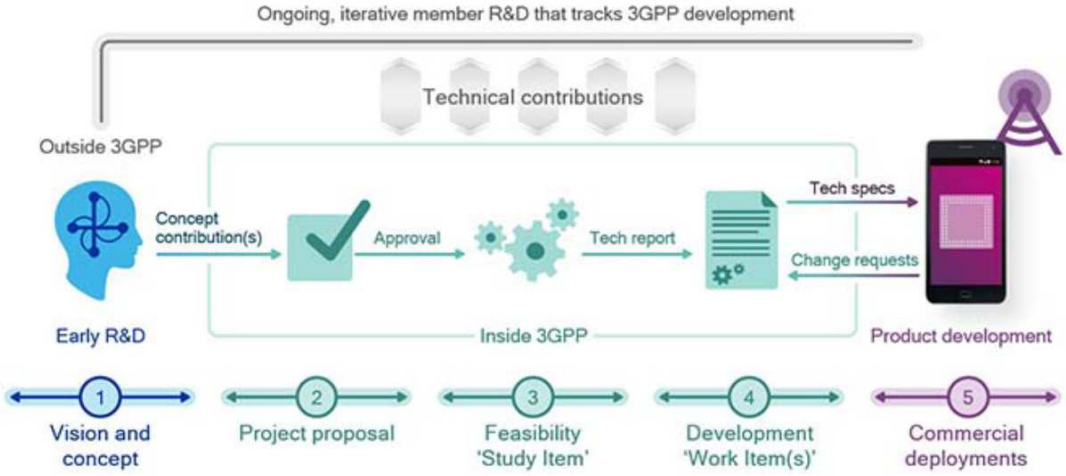

Source: [82].

spatially and time consistence samples, lognormal shadowing component, small-scale fading, and distance-dependent path-loss;

- Scenario layout based on Madrid Grid [85];
- Antenna array and multipanel node capability;
- IAB with topology adaptation and handover;
- NCR utilizing AF relaying combined with beamforming;
- RIS with reflection mode;
- UAV modeling.

The following sections delve deeper into the details of definitions and models of the toolbox utilized throughout this work.

6.3 Physical layer

Regarding the physical layer, the considered toolbox is flexible enough to simulate different structures. The one considered in this work was the 5G NR physical layer standardized by 3GPP [86]. In 5G NR, orthogonal frequency division multiplexing (OFDM) remains the chosen waveform for transmissions due to its resilience against time dispersion and the ability to leverage both time and frequency domains.

Unlike LTE, 5G NR has a flexible numerology as presented in table 6.1. In OFDM systems, a critical design choice is the numerology, which encompasses the subcarrier spacing and cyclic prefix length. A wider subcarrier spacing offers advantages. It makes transmissions less susceptible to frequency errors and phase noise. However, for a given cyclic prefix length, the relative overhead increases the larger the subcarrier spacing is and from this perspective a smaller subcarrier spacing would be preferable. The selection of the subcarrier spacing therefore needs

Table 6.1 – Supported transmission numerologies.

μ	**Subcarrier Spacing $2^{\mu} \cdot 15$ [kHz]**	**Cyclic Prefix [μs]**	**Slot Duration [ms]**	$\mathbf{N^{slot}_{symbol}}$	$\mathbf{N^{subframe}_{slot}}$	$\mathbf{N^{frame}_{slot}}$
0	15	4.7	1	14	1	10
1	30	2.3	0.5	14	2	20
2	60	1.2	0.25	14	4	40
3	120	0.59	0.125	14	8	80
4	240	0.29	0.0625	14	16	160

Source: [88]

to carefully balance overhead from the cyclic prefix against sensitivity to Doppler spread/shift and phase noise [87].

NR was designed to be adaptable enough to support different deployment scenarios, including deployments with transmissions in sub-6 GHz and mmWave ranges. In sub-6 GHz, the cell size is larger and it is necessary a cyclic prefix capable of handling the delay spread expected in this type of deployment (in the order of a couple of microsseconds). Consequently, it is needed a subcarrier spacing in the range of 15 - 30 kHz. MmWave presents a different set of challenges. Phase noise becomes a more significant issue, requiring a wider subcarrier spacing for improved resistance. However, mmWave deployments typically involve smaller cells due to the demanding propagation conditions at these high frequencies. This smaller cell size translates to a reduced delay spread. Consequently, mmWave transmissions benefit from a combination of wider subcarrier spacing and a shorter cyclic prefix.

Regarding the time domain, the NR physical layer is split in frames. As illustrated in figure 6.2, each frame lasts 10 milliseconds and is further divided into 10 subframes of 1 millisecond duration. Each subframe is composed of slots, containing $N^{slot}_{symbol} = 14$ OFDM symbols each slot. Since, when doubling the subcarrier spacing, the OFDM symbol duration halves due to the nature of OFDM, there are different numbers of slots $N^{subframe}_{slot}$ and N^{frame}_{slot} within one subframe and one frame, respectively, for each numerology, as presented in table 6.1 and in figure 6.2. Remark that the number of OFDM symbols in one subframe changes according to the value of subcarrier spacing. When using a subcarrier spacing of 15 kHz in NR, the structure of an NR slot becomes identical to an LTE subframe that uses a normal cyclic prefix. This overlap is advantageous because it simplifies the coexistence of NR and LTE technologies in the same network.

While some concepts/definitions are the same in LTE and NR, like the duration of frames and subframes, other aspects differ. In LTE, a subframe is the smallest unit for scheduling data transmission. This subframe is made of just 2 slots, each with 7 OFDM symbols. In NR, however, the minimum scheduling unit in the time domain is typically a slot, which contains 14 OFDM symbols, twice as many as an LTE slot [89].

Concerning the frequency domain, LTE and NR have subtle differences. Both use

Figure 6.2 – Frame, subframe and slots in NR.

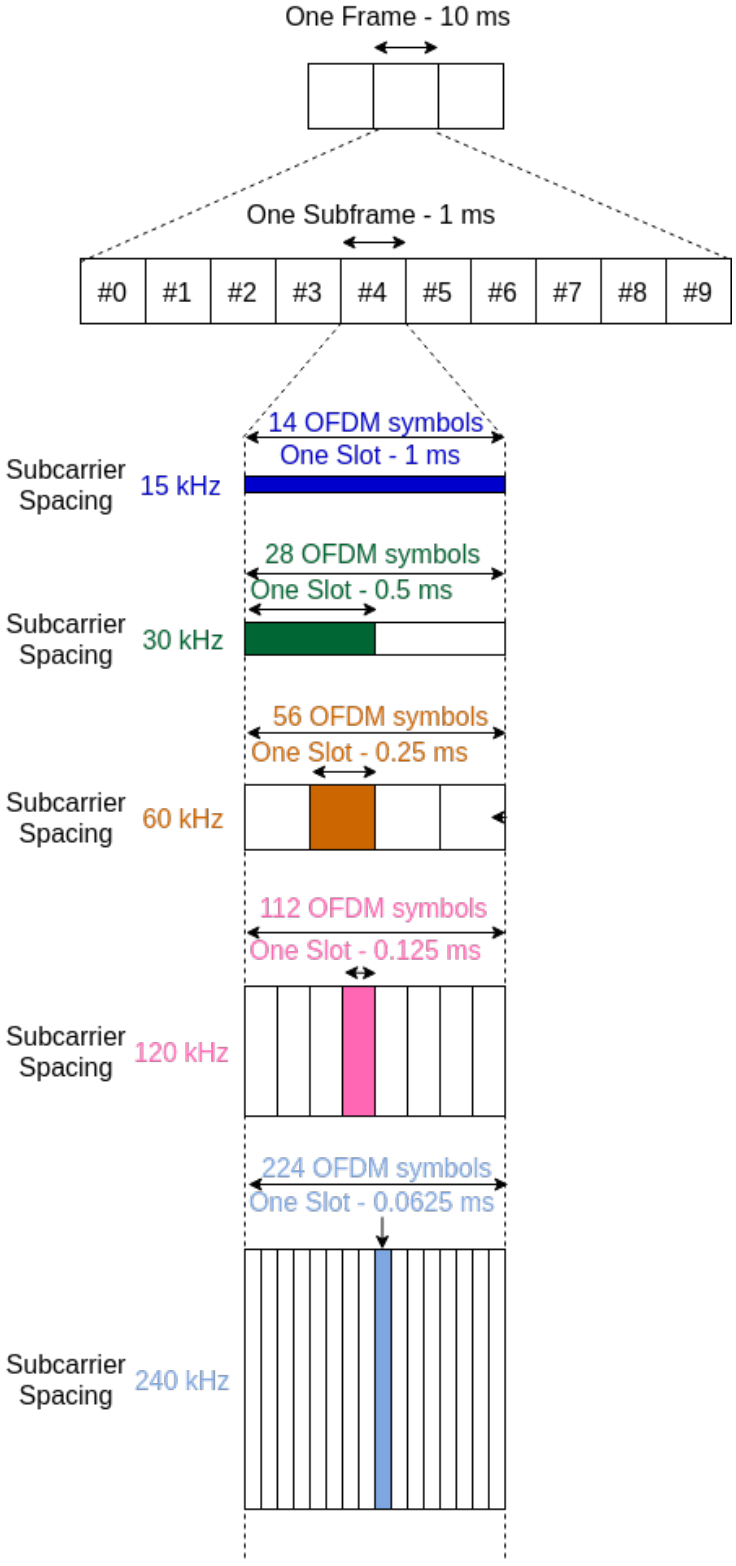

Source: [88]

resource element for a single subcarrier within an OFDM symbol. However, resource block (RB) has distinct meanings. While LTE defines a RB in two dimensions: 12 subcarriers in frequency and one slot in time, in NR, it is a one-dimensional term referring to a group of 12 consecutive subcarriers in the frequency domain. This difference in NR reflects the flexibility it offers in

Figure 6.3 – Resource element, RB and PRB in NR.

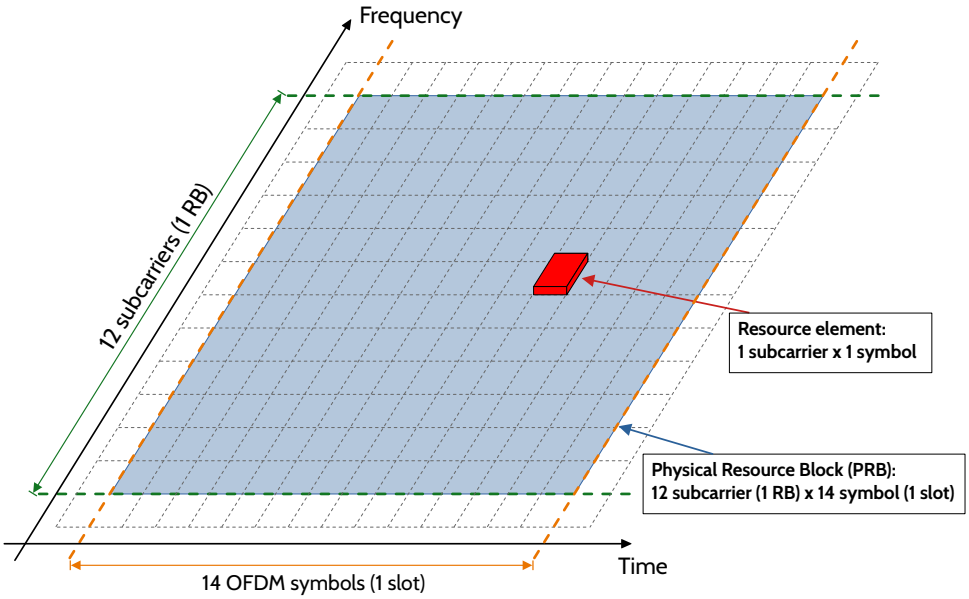

Source: Created by the author.

scheduling data transmissions with varying time durations.

Other important concept in NR is physical resource block (PRB). One PRB is composed of 12 subcarriers in the frequency domain, like an RB, and, in time domain, of 14 OFDM symbols or one time slot. Figure 6.3 illustrates a resource element, a RB and a PRB in NR.

6.4 Channel model

Regarding the links between the nodes in the system, in this work, they are modeled using the 3GPP channel model [84]. As previously mentioned, it is a spatially and time consistent model. It considers a distance-dependent path-loss, a lognormal shadowing component, and a small-scale fading component. It models the channel impulse response $h_{u,s}$ between transmit antenna element s and receive antenna element u as a sum of the LOS channel coefficient, $h_{u,s}^{\text{LOS}}$, and the NLOS channel impulse response, $h_{u,s}^{\text{NLOS}}$, scaled according to the Ricean K-factor K_R as:

$$h_{u,s}(\tau,t) = \sqrt{\frac{K_R}{K_R+1}} h_{u,s}^{\text{LOS}}(t)\delta(\tau-\tau_1) + \sqrt{\frac{1}{K_R+1}} h_{u,s}^{\text{NLOS}}(\tau,t), \tag{6.1}$$

where $\delta(\cdot)$ is the Dirac's delta function, t is time, and τ is delay.

Defining $F_{\text{rx},u,\widehat{\theta}}(\theta,\phi)$ and $F_{\text{rx},u,\widehat{\phi}}(\theta,\phi)$ as the field patterns of receive antenna element u in the direction of spherical basis vector $\widehat{\theta}$ and $\widehat{\phi}$, respectively, and $F_{\text{tx},s,\widehat{\theta}}$ and $F_{\text{tx},s,\widehat{\phi}}$ as the field patterns of transmit antenna element s in the direction of spherical basis vector $\widehat{\theta}$ and $\widehat{\phi}$, respectively, we arrange these field components in the vector:

$$\mathbf{f}_{b_1,b_2,[C]}^{[A]} = \begin{bmatrix} F_{[A],\theta}\left(\theta_{[C],b_1},\phi_{[C],b_2}\right) \\ F_{[A],\phi}\left(\theta_{[C],b_1},\phi_{[C],b_2}\right) \end{bmatrix}, \tag{6.2}$$

where $[C]$ is equal to either $[LOS]$ (when we refer to the LOS component) or $[n,m]$ (when we refer to the m-th NLOS component, from a total of M rays, that goes through scatter cluster n, from a total of N scatter clusters); and $\{[A],b_1,b_2\}$ is equal to either $\{[\text{rx},u],\text{ZOA},\text{AOA}\}$ or $\{[\text{tx},s],\text{ZOD},\text{AOD}\}$ where ZOA and AOA refer to the zenith and azimuth angles of arrival, while ZOD and AOD refer to the zenith and azimuth angles of departure.

Based on these definitions, $h_{u,s}^{\text{LOS}}(t)$ and $h_{u,s}^{\text{NLOS}}(\tau,t)$ are defined as:

$$h_{u,s}^{\text{NLOS}}(\tau,t) = \sum_{n=1}^{N}\sum_{m=1}^{M} h_{u,s,n,m}^{\text{NLOS}}(t)\delta(\tau-\tau_n) \tag{6.3}$$

and

$$h_{u,s}^{\text{LOS}}(t) = \left(\mathbf{f}_{\text{ZOA,AOA,[LOS]}}^{[\text{rx},u]}\right)^{\text{T}} \begin{bmatrix} 1 & 0 \\ 0 & -1 \end{bmatrix} \mathbf{f}_{\text{ZOD,AOD,[LOS]}}^{[\text{tx},s]} \times E_{-d_{3D}} E_{\widehat{r}_{\text{rx,LOS}}^{T}\cdot\overline{d}_{\text{rx},u}} E_{\widehat{r}_{\text{tx,LOS}}^{T}\cdot\overline{d}_{\text{tx},s}} E_{\widehat{r}_{\text{rx,LOS}}^{T}\cdot\overline{\nu}}, \tag{6.4}$$

where

$$E_a = \exp\left(j2\pi\frac{a}{\lambda_c}\right); \tag{6.5}$$

$h_{u,s,n,m}^{\text{NLOS}}(t)$ is defined as

$$\begin{aligned} h_{u,s,n,m}^{\text{NLOS}}(t) = & \\ & \sqrt{\frac{P_n}{M}} \left(\mathbf{f}_{\text{ZOA,AOA,}[n,m]}^{[\text{rx},u]}\right)^{T} \begin{bmatrix} \exp\left(j\Phi_{n,m}^{\theta\theta}\right) & \sqrt{\kappa_{n,m}^{-1}}\exp\left(j\Phi_{n,m}^{\theta\phi}\right) \\ \sqrt{\kappa_{n,m}^{-1}}\exp\left(j\Phi_{n,m}^{\phi\theta}\right) & \exp\left(j\Phi_{n,m}^{\phi\phi}\right) \end{bmatrix} \mathbf{f}_{\text{ZOD,AOD,}[n,m]}^{[\text{tx},s]} \\ & \times E_{\widehat{r}_{\text{rx},n,m}^{T}\cdot\overline{d}_{\text{rx},u}} E_{\widehat{r}_{\text{tx},n,m}^{T}\cdot\overline{d}_{\text{tx},s}} E_{\widehat{r}_{\text{rx},n,m}^{T}\cdot\overline{\nu}\cdot t} \end{aligned} \tag{6.6}$$

and P_n is the power of scatter cluster n; d_{3D} is the 3D distance between transmitter and receiver; $\overline{d}_{\text{tx},s}$ is the location vector of transmit antenna element s; $\overline{d}_{\text{rx},u}$ is the location vector of receive antenna element u; λ_c is the wavelength of the carrier frequency; $\overline{\nu}$ is the velocity vector with speed ν; $\{\Phi_{n,m}^{\theta\theta},\Phi_{n,m}^{\theta\phi},\Phi_{n,m}^{\phi\theta},\Phi_{n,m}^{\phi\phi}\}$ is the random initial phase for each ray m of each cluster n and for four different polarisation combinations $(\theta\theta,\theta\phi,\phi\theta,\phi\phi)$; $\kappa_{n,m}$ is the cross polarisation power ratio for each ray m of each cluster n and $\widehat{r}_{\text{rx},LOS}^{T}(\widehat{r}_{\text{tx},LOS}^{T})$ is the spherical unit vector with azimuth arrival (departure) angle $\phi_{\text{LOS,AOA}}(\phi_{\text{LOS,AOD}})$ and zenith arrival (departure) angle $\theta_{\text{LOS,ZOA}}(\theta_{\text{LOS,ZOD}})$, given by

$$\widehat{r}_{\text{rx,LOS}}^{T} = \begin{bmatrix} \sin\left(\theta_{\text{LOS,ZOA}}\right)\cos\left(\phi_{\text{LOS,AOA}}\right) \\ \sin\left(\theta_{\text{LOS,ZOA}}\right)\sin\left(\phi_{\text{LOS,AOA}}\right) \\ \cos\left(\theta_{\text{LOS,ZOA}}\right) \end{bmatrix} \tag{6.7}$$

and

$$\widehat{r}_{\text{tx,LOS}}^{T} = \begin{bmatrix} \sin\left(\theta_{\text{LOS,ZOD}}\right)\cos\left(\phi_{\text{LOS,AOD}}\right) \\ \sin\left(\theta_{\text{LOS,ZOD}}\right)\sin\left(\phi_{\text{LOS,AOD}}\right) \\ \cos\left(\theta_{\text{LOS,ZOD}}\right) \end{bmatrix}. \tag{6.8}$$

In each transmission time interval (TTI) t, the elements $h_{u,s}(\tau,t)$, equation (6.1), are arranged in a multi-dimensional array $\underline{\mathbf{h}} \in \mathbb{R}^{U\times S\times T}$, where U and S are the number of receive and transmit antenna elements, respectively, and T is the number of taps. Applying the Fourier transform to $\underline{\mathbf{h}}$ we get $\underline{\mathbf{H}} \in \mathbb{R}^{U\times S\times C}$, where C is the number of subcarriers. Considering an RB k as the minimum scheduling unit in the frequency domain, i.e., a set of subcarriers that must be scheduled together, and that the subcarriers in an RB are correlated, then for each RB we consider only the central subcarrier. Thus, in the following, we call $\widehat{\mathbf{H}}_k \in \mathbb{R}^{U\times S}$ a subarray of $\underline{\mathbf{H}}$, where its third dimension corresponds to the the central subcarrier of RB k.

Finally, the effective $\mathbf{H}_k$ of the channel in RB k is defined as:

$$\mathbf{H}_k = \sqrt{S_{SF}L_k}\widehat{\mathbf{H}}_k, \tag{6.9}$$

where S_{SF} is the shadow gain (log-normally distributed with standard deviation σ_{SF}) and L_k is the path loss relative to frequency f_k of the central subcarrier of RB k. Table 6.2 presents the path loss expression L_k and standard deviation σ_{SF} for LOS/NLOS and urban macro (UMa)/urban micro (UMi) scenarios, where 3D distance d_{3D} is in meters and frequency f_k is in GHz.

Table 6.2 – Path loss L_k and standard deviation σ_{SF} from shadow fading (in Table 7.4.1-1 of [84]).

	UMa	UMi
LOS	$L_k = 28 + 22\log_{10}(d_{3D}) + 20\log_{10}(f_k)$ $\sigma_{SF} = 4\text{dB}$	$L_k = 32.4 + 21\log_{10}(d_{3D}) + 20\log_{10}(f_k)$ $\sigma_{SF} = 4\text{dB}$
NLOS	$L_k = 32.4 + 20\log_{10}(d_{3D}) + 30\log_{10}(f_k)$ $\sigma_{SF} = 7.8\text{dB}$	$L_k = 32.4 + 20\log_{10}(d_{3D}) + 31.9\log_{10}(f_k)$ $\sigma_{SF} = 8.2\text{dB}$

Source: Created by the author.

6.5 Physical layer measurements

Some physical layer metrics available at the GTEL toolbox that were used in this work are the reference signal received power (RSRP) and the signal to interference-plus-noise ratio (SINR) [90]. They are defined as:

- RSRP: it is the linear average over the power contributions (in watts) of the resource elements carrying either SSBs or channel state information reference signals (CSI-RSs) within the considered measurement frequency bandwidth.
- SINR: a metric quantifying the relative strength of a desired signal compared to the background noise and interference affecting it. It is the linear average over the power

contributions (in watts) of the resource elements carrying either SSBs or CSI-RSs divided by the linear average of the noise and interference power contribution (in watts) over the same resources.

In the following subsections, it is shown the expressions of the SINR perceived by the UEs when they are connected through an IAB node, an NCR, or a RIS. The equations are formulated for the DL, but a similar approach can be used for the UL. Furthermore, IAB operates in in-band mode. For this, consider that a PRB is the minimum allocable frequency block, where, as already defined, one PRB is composed of 12 subcarriers in the frequency domain and, in time domain, of 14 OFDM symbols (one time slot). The available frequency band is split into K PRBs.

6.5.1 SINR of UEs served by IAB nodes

The useful power $S^{IAB}_{u_x,k}$ received by UE u_x served by an IAB node, e.g., IAB node r_x, at PRB k can be expressed as:

$$S^{IAB}_{u_x,k} = \gamma_{r_x,u_x,k} \cdot p_{r_x,u_x,k}, \tag{6.10}$$

where $p_{r_x,u_x,k}$ is transmit power used by IAB node r_x to transmit useful signal to UE u_x at PRB k; and $\gamma_{i,j,k} = \mathbf{d}_{j,k}\mathbf{H}_{i,j,k}\mathbf{f}_{i,k}$ denotes the combined effect of the channel $\mathbf{H}_{i,j,k}$ after the transmission and reception filters $\mathbf{f}_{i,k}$ and $\mathbf{d}_{j,k}$, respectively, applied to a signal transmitted by node i to node j at PRB k.

The interference signals on UE u_x comes from two types of sources: backhaul links and access links. More precisely, signals belonging to the first type are transmitted at PRB k by a given IAB node, e.g., IAB node r_i, to its serving gNB b_i. Moreover, signals belonging to the second type are transmitted in the access links for other UEs, e.g., UE u_y, at PRB k. The transmitter q_y is its serving node, which can be either another IAB or a macro gNB. Thus, the interference $I^{IAB}_{u_x,k}$ perceived by UE u_x at PRB k is equal to:

$$I^{IAB}_{u_x,k} = \sum_{(r_i,b_i)\in\mathcal{R}\times\mathcal{B}} \gamma_{r_i,b_i,k} \cdot p_{r_i,b_i,k} + \sum_{\substack{(u_y,q_y)\in\mathcal{U}\times(\mathcal{R}\cup\mathcal{B}),\\ y\neq x}} \gamma_{q_y,u_x,k} \cdot p_{q_y,u_y,k}, \tag{6.11}$$

where $\mathcal{R}$, $\mathcal{B}$ and $\mathcal{U}$ are the sets of IABs nodes, gNBs and UEs in the system, respectively.

Finally, the SINR $\rho^{IAB}_{u_x,k}$ perceived by UE u_x at PRB k is

$$\rho^{IAB}_{u_x,k} = \frac{S^{IAB}_{u_x,k}}{I^{IAB}_{u_x,k} + \sigma^2_k}, \tag{6.12}$$

where σ^2_k is the noise component at PRB k.

Figure 6.4 – Possible links that a UE receives in scenario with more than one NCR.

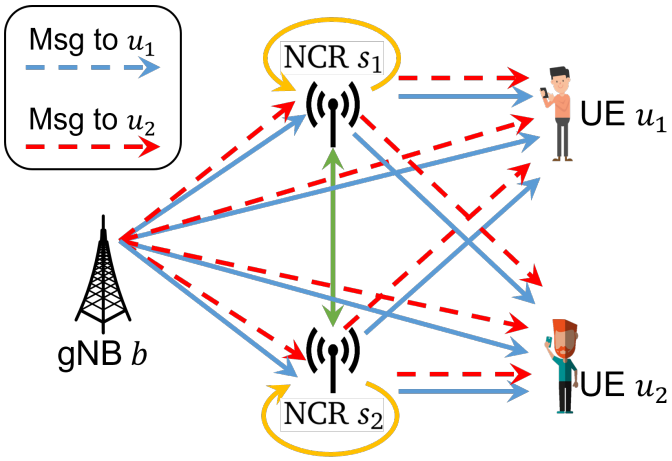

Source: Created by the author.

6.5.2 SINR of UEs served through NCRs

Figure 6.4 illustrates the links that the UEs can receive in a scenario with one gNB controlling more than one NCR. In our implementation, it is neither considered the link between NCRs (green arrow) nor the NCR self-interference (yellow arrows). Regarding the interference between NCRs, this can be mitigated during the deployment phase by avoiding placing one in the coverage area of the other. Concerning the NCR self-interference, it can be mitigated by placing the NCR antenna arrays with angular distance between them equal to or higher than 120 degrees, this phenomenon is mitigated [44].

Consider a UE u_x which is connected to gNB b_x through NCR s_x. The useful power $S^{NCR}_{u_x,k}$ received at PRB k by UE u_x can be split into two parts, i.e., the direct link from the gNB and the link through the NCR. It can be expressed as:

$$S^{NCR}_{u_x,k} = \gamma_{b_x,u_x,k} \cdot p_{b_x,u_x,k} + \gamma_{s_x,u_x,k} \cdot g_{s_x,k} \cdot \gamma_{b_x,s_x,k} \cdot p_{b_x,u_x,k}, \tag{6.13}$$

where $p_{b_x,u_x,k}$ is the transmit power used by gNB b_x to transmit useful signal at PRB k, and $g_{s_x,k}$ is the fixed power gain applied by NCR s_x at PRB k.

The interference can be split into three sets. The first one is composed by signals received directly from other gNBs, e.g., gNB b_i with $i \neq x$, which were transmitted at PRB k to others UEs u_y. The second set is composed by copies of the signals that belong to the first set and that were amplified by an NCR. Signals from others gNBs that are captured by NCR which is not connected to them. The third set is composed by the amplified noises from all NCR with exception of the one whose the UE u_x is connected through. Thus, the interference $I^{NCR}_{u_x,k}$ perceived by UE u_x at PRB k is equal to:

$$I_{u_x,k}^{NCR} = \sum_{\substack{(u_y,b_y)\in\mathcal{U}\times\mathcal{B},\\ y\neq x}} \gamma_{b_y,u_x,k}\cdot p_{b_y,u_y,k} + \sum_{\substack{(u_y,b_y)\in\mathcal{U}\times\mathcal{B},\\ y\neq x}} \sum_{s_i\in\mathcal{S}} \gamma_{s_i,u_x,k}\cdot g_{s_i,k}\cdot \gamma_{b_y,s_i,k}\cdot p_{b_y,u_y,k} + \sigma_k^2 \cdot \sum_{\substack{s_i\in\mathcal{S},\\ y\neq x}} \gamma_{s_i,u_x,k}\cdot g_{s_i,k}, \quad (6.14)$$

where $\mathcal{S}$ is the set of NCRs.

The overall noise power $N_{u_x,k}$ received by UE u_x at PRB k is the noise component added of the noise component amplified by the NCRs whose the UE u_x is connected through. It can be expressed as:

$$N_{u_x,k} = \sigma_k^2(1+\gamma_{s_x,u_x,k}\cdot g_{s_x,k}). \quad (6.15)$$

Finally, the SINR $\rho_{u_x,k}^{NCR}$ perceived by UE u_x at PRB k is

$$\rho_{u_x,k}^{NCR} = \frac{S_{u_x,k}^{NCR}}{I_{u_x,k}^{NCR}+N_{u_x,k}}. \quad (6.16)$$

6.5.3 SINR of UEs served through RISs

Consider a UE u_x which is connected to gNB b_x through RIS t_x. The useful power $S_{u_x,k}^{RIS}$ received at PRB k by UE u_x can be split into two parts as in the NCR case, i.e., the direct link from the gNB and the link through the RIS. It can be expressed as:

$$S_{u_x,k}^{RIS} = \gamma_{b_x,u_x,k}\cdot p_{b_x,u_x,k} + \eta_{b_x,u_x,k}\cdot p_{b_x,u_x,k}, \quad (6.17)$$

where $\eta_{i,j,k} = \mathbf{d}_{j,k}\mathbf{H}_{t_x,j,k}\boldsymbol{\Theta}\mathbf{H}_{i,t_x,k}\mathbf{f}_{i,k}$ denotes the combined effect of the channel when signal is received through RIS. $\mathbf{H}_{i,t_x,k}$ is the channel between transmitter i, whose precoder is $\mathbf{f}_{i,k}$, and the RIS t_x at PRB k. The matrix of reflection coefficients is given by $\boldsymbol{\Theta}$ and its calculation is based on [54]. $\mathbf{H}_{t_x,j,k}$ is channel between RIS t_x and receiver j, whose combiner is $\mathbf{d}_{j,k}$ at PRB k.

As in the NCR case, we neither consider the RIS self-interference or intereference between RISs. This is because, in practice, a passive RIS relies on LOS links, and in outdoor urban environments where there are huge number of obstacles, these links between RISs are highly unlikely.

Furthermore, similar to what was done in equation (6.14), except by the third term that represents the amplified noise, the interference received by UE u_x is:

$$I_{u_x,k}^{RIS} = \sum_{\substack{(u_y,b_y)\in\mathcal{U}\times\mathcal{B},\\ y\neq x}} \gamma_{b_y,u_x,k}\cdot p_{b_y,u_y,k} + \sum_{\substack{(u_y,b_y)\in\mathcal{U}\times\mathcal{B},\\ y\neq x}} \sum_{t_i\in\mathcal{T}} \eta_{b_y,u_x,k}\cdot p_{b_y,u_y,k}, \quad (6.18)$$

where $\mathcal{T}$ is the set of RISs.

Finally, the SINR $\rho^{RIS}_{u_x,k}$ perceived by UE u_x at PRB k is

$$\rho^{RIS}_{u_x,k} = \frac{S^{RIS}_{u_x,k}}{I^{RIS}_{u_x,k} + \sigma^2_k}, \tag{6.19}$$

where the σ^2_k is the noise component at PRB k.

6.6 Initial access and resource management

Concerning the initial access, the RSRP was used as metric to define the serving node of an UE. The selection was based on the node providing the strongest RSRP.

Concerning resource management, this work focused on the allocation of frequency, time, space and power. Regarding the power allocation, it was considered equal power allocation (EPA) between the RBs. With respect to scheduling in time, frequency and space, the allocation in these domains was performed together by the round robin (RR) algorithm. The RR iteratively schedules the UEs' bearers waiting the longest time in the queue. The RR was chosen since it is a well-known scheduler, which enables an interested reader to reproduce the performance evaluations.

6.7 Link adaptation

Link adaptation consists of dynamically adjusting transmission parameters, such as modulation and coding schemes (MCSs), to match the conditions of the UEs' radio links. In the presence of good propagation conditions, a high order modulation scheme with low coding redundancy, such as MCS 15, can be used to increase the transmission data rate while in the presence of signal fade, the system selects a more robust modulation scheme and a higher coding rate, such as MCS 1 to maintain both connection quality and link stability without increasing the signal power [91].

Table 6.3 presents the mapping of channel quality indicator (CQI) into MCS adopted in NR and standardized in [92]. Note that larger CQI indexes, i.e., better channel conditions, allow to transmit more bits on each OFDM symbol and to use the channel more efficiently.

Differences in MCS imply different block error rate (BLER) performances, which can be seen in figure 6.5. It represents the relationship between SNR, BLER and MCS. Note that for the same SNR, a higher MCS index represents higher BLER, which means that a given MCS requires a certain SNR to operate with an acceptably low BLER.

Table 6.3 – CQI and MCS mapping standardized in [92].

CQI index	**Modulation**	**Code rate (x 1024)**	**Rate (Bits/symbol)**	**CQI index**	**Modulation**	**Code rate (x1024)**	**Rate (Bits/symbol)**
0		Out of range		8	16QAM	490	1.9141
1	QPSK	78	0.152	9	16QAM	616	2.4063
2	QPSK	120	0.234	10	64QAM	466	2.7305
3	QPSK	193	0.377	11	64QAM	567	3.3223
4	QPSK	308	0.602	12	64QAM	666	3.9023
5	QPSK	449	0.877	13	64QAM	772	4.5234
6	QPSK	602	1.176	14	64QAM	873	5.1152
7	16QAM	378	1.477	15	64QAM	948	5.5547

Source: [88]

Figure 6.5 – Relationship between SNR, BLER and MCS.

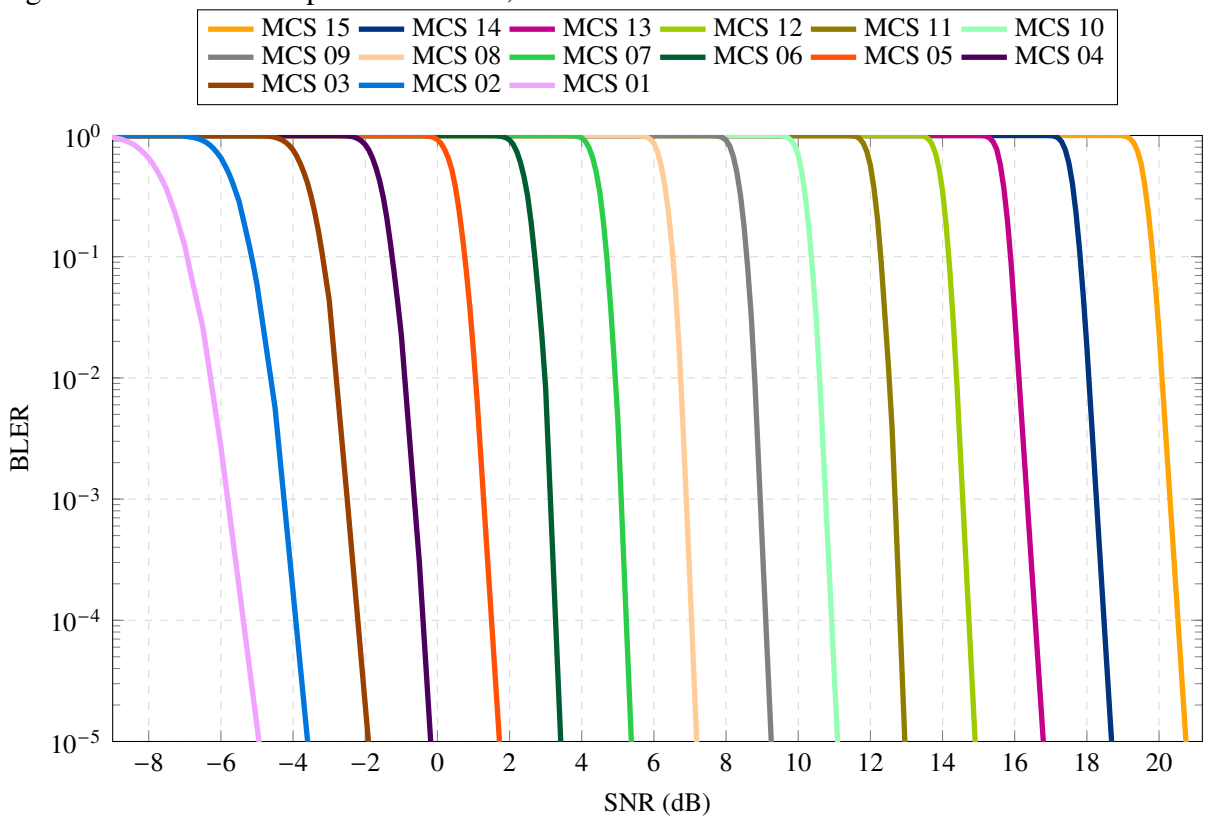

Source: [88]

7 COMPARISON OF THE HETNET PERFORMANCE IN SPORT EVENT

Taking into account the concepts already presented regarding IAB, NCR, and RIS, this chapter presents a performance comparison between a scenario without them, called herein as macro only scenario, and other scenarios with the deployment of one of them either as fixed nodes or as mobile nodes mounted in an UAV. The details concerning the specific system model and the adopted parameters are presented in sections 7.1 and 7.2, respectively. The results are presented and discussed in section 7.3.

7.1 Specific system model

Based on use case “5.11.2.2 - Use case: User outside the vehicle” presented on 3GPP TR 22.839 [93] “Study on Vehicle Mounted Relays”, it is considered a scenario where an outdoor sport event takes place, i.e., a bike race. As illustrated in figure 7.1, a simplified Madrid grid scenario [85] is considered. Cameramen riding motorcycles broadcast live videos of the race. Half of the cameramen are in one street, while the others are in the parallel one.

More precisely, the scenario consisted of 120 m $\times$ 120 m blocks surrounded by 3 m width sidewalks and 14 m width streets. The UEs, i.e., cameramen’s equipments, were initially positioned in the left block, half of them in the upper middle street and the others in the lower middle street, as illustrated in figure 7.1. Besides that, the UEs traversed 3 blocks at a speed of 40 km/h.

In this scenario, six different deployments are considered. The first one considers the existence of only two traditional macro gNBs, the black nodes in figure 7.1. The second, third and fourth deployments consider, besides the traditional macro gNB, the deployment of a fixed IAB node, of a fixed NCR or of a fixed RIS, respectively (IAB and NCR are blue nodes, while the RISs are the yellow ones in figure 7.1). Due to inherit RIS characteristic of reflection, it is strategically placed at a different position to benefit its property. The other two scenarios, i.e., fifth and sixth, consider the possibility of, besides the traditional macro gNB, deploying an IAB node or a NCR mounted on a mobile UAV, respectively, to follow the cameramen.

Regarding the fixed IAB node and fixed NCR, presented in the second and third deployments, respectively, as shown in figure 7.1, they are deployed alligned with the gNB, but two blocks away. Furthermore, they have three antenna arrays to provide a better street coverage. The antenna arrays are spaced by 120° from each other in order to minimize the interference between them. One of the antenna arrays, called herein as backhaul antenna array, steers towards the gNB. The other two, called herein as access antenna arrays, points towards the street where the cameramen are moving, with an angular distance of 120° between them. Unlike these fixed nodes, mobile UAV only has two antenna arrays to avoid excess weight, one for the backhaul link and other for the access links.

Figure 7.1 – Scenario with each of the 3 possible deployments which are serving the cameramen on the motorcycle. The deployments are only gNB, or with fixed or UAV HetNet.

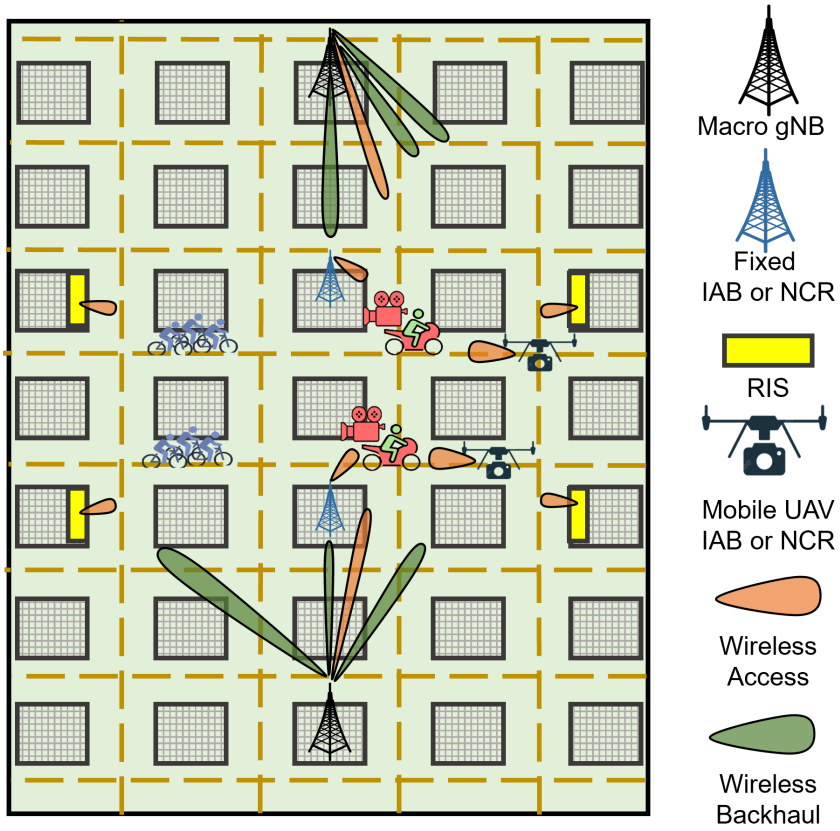

Source: Created by the author.

Concerning the RISs (present in the fourth deployment), as already mentioned, they are deployed in a position different of the fixed IAB nodes and fixed NCRs due to the reflection characteristics. Moreover, the choice of 4 RISs (instead of 2, as the number of fixed IAB nodes and NCRs in the second and third deployments, respectively) aims at improving the coverage and at matching the amount of fixed nodes' access antenna arrays of IAB and NCR.

Specifically for RIS, the matrix of reflection coefficients $\mathbf{\Theta}$ is calculated with the gNB beamforming $\mathbf{f}_{b_x,k}$, inspired by the suboptimal algorithm presented in [54]. The condition for this algorithm is a LOS in the channel $\mathbf{H}_{b_x,t_x,k}$ between gNB b_x and RIS t_x, i.e., $\text{rank}(\mathbf{H}_{b_x,t_x,k}) = 1$, and a MISO communication, i.e., RIS assists a multi-antenna gNB that is communicating with single antenna UE. The objective of the algorithm is to maximize the signal strength received by the UE u_x which is expressed as

$$p_{b_x,u_x,k} \cdot |(\mathbf{H}_{t_x,u_x,k}\mathbf{\Theta}\mathbf{H}_{b_x,t_x,k} + \mathbf{H}_{b_x,u_x,k})\mathbf{f}_{b_x,k}|^2, \tag{7.1}$$

where the terms $\mathbf{H}_{t_x,u_x,k}\mathbf{\Theta}\mathbf{H}_{b_x,t_x,k}$ and $\mathbf{H}_{b_x,u_x,k}$ represent the portion of the signal strength received by UE u_x through the RIS link and through the direct link, respectively. In [54], the gNB calculates the two suboptimal values for $\mathbf{f}_{b_x,k}$, i.e.,

$$\mathbf{f}_{b_x,k}^{(1)} = \frac{\mathbf{H}_{b_x,u_x,k}^{H}}{||\mathbf{H}_{b_x,u_x,k}^{H}||} \tag{7.2}$$

and

$$\mathbf{f}_{b_x,k}^{(2)} = \frac{[\mathbf{H}_{b_x,t_x,k}^{H}]_m}{||[\mathbf{H}_{b_x,t_x,k}^{H}]_m||}, \tag{7.3}$$

where $\mathbf{f}_{b_x,k}^{(1)}$ is the beamforming vector that maximizes a direct transmission from gNB to UE (not using RIS), and $\mathbf{f}_{b_x,k}^{(2)}$ is the beamforming vector that maximizes a transmission from gNB to UE through RIS (neglecting the direct link gNB-UE). Since it is considered that $\mathbf{H}_{b_x,t_x,k}^{H}$ has rank 1, i.e., the NLOS components are negligible compared to the LOS component, thus for the calculation of $\mathbf{f}_{b_x,k}^{(2)}$, it can be used any column m of $\mathbf{H}_{b_x,t_x,k}^{H}$, i.e., $[\mathbf{H}_{b_x,t_x,k}^{H}]_m$. $\mathbf{f}_{b_x,k}^{(1)}$ and $\mathbf{f}_{b_x,k}^{(2)}$ are two maximum ratio transmission (MRT) precoders as shown above. However, in our implementation, it is chosen $\mathbf{f}_{b_x,k}^{(1)}$ and $\mathbf{f}_{b_x,k}^{(2)}$ from a codebook, where each precoder is one column of a discrete fourier transform (DFT) matrix. The matrix of reflection coefficients $\mathbf{\Theta}$ is calculated such that the direct signal between gNB-UE and the reflected signal gNB-RIS-UE arrive at the UE in phase. Thus,

$$\arg(\theta_{n,i}) = \arg(\mathbf{H}_{b_x,u_x,k}\mathbf{f}_{b_x,k}^{(i)}) - \arg([\mathbf{H}_{t_x,u_x,k}]_n) - \arg(\mathbf{H}_{b_x,t_x,k}\mathbf{f}_{b_x,k}^{(i)}), \tag{7.4}$$

where $|\theta_{n,i}|$ is the reflection coefficient associated with the n-th RIS antenna element and $i \in \{1,2\}$. Finally, based on the two solutions, i.e., $(\mathbf{f}_{b_x,k}^{(1)}, \mathbf{\Theta}_1)$ and $(\mathbf{f}_{b_x,k}^{(2)}, \mathbf{\Theta}_2)$, it is chosen $i = i^*$, such that

$$i^* = \underset{i\in\{1,2\}}{\arg\max} \left\{ p_{b_x,u_x,k} \cdot |(\mathbf{H}_{t_x,u_x,k}\mathbf{\Theta}_i\mathbf{H}_{b_x,t_x,k} + \mathbf{H}_{b_x,u_x,k})\mathbf{f}_{b_x,k}^{(i)}|^2 \right\}. \tag{7.5}$$

We remark that this algorithm optimizes the transmission for one specific UE. Thus, to use this algorithm in a multi-user scenario, one needs to select a UE to which the transmission with the RIS will be optimized. In this work, we have used the RR scheduler to perform this selection. Even though the transmission is optimized for a given UE, other UEs close to it will also be benefited. We call herein a cluster the set with the selected UE and its neighbors that are also benefited by the transmission through the RIS.

7.2 Simulation assumptions

As presented in chapter 6, the considered channel model was based on 3GPP channel model standardized in [94] and [69]. Concerning the frequency domain, the carrier was centered at 28 GHz with bandwidth of 50 MHz. Other channel characteristics are listed in Tables 7.1 and 7.3.

With respect to the link adaptation, it was considered a target BLER of 10% and the CQI/MCS mapping curves standardized in [92]. An outer loop strategy was considered to avoid the increase of the BLER. More precisely, when a transmission error occurred, the estimated SINR is decreased by 1 dB, however, when a transmission occurred without error, the estimated SINR had its value added by 0.1 dB. Tables 7.2 and 7.3 present other simulation parameters.

Table 7.1 – Characteristics of the links in same cell.

Link in same cell	**Scenario**	**LOS/NLOS**
gNB - UE	Urban Macro [94]	NLOS
gNB - Fixed IAB/NCR/RIS	Urban Macro [94][69]	LOS/NLOS
gNB - Mobile UAV w/ IAB/NCR	Urban Macro [69]	LOS
IAB/NCR/RIS - UE	Urban Micro [94][69]	LOS
Mobile UAV w/ IAB/NCR - UE	Urban Micro [69]	LOS
UE - UE	Urban Micro [94]	LOS
Link in different cell	**Scenario**	**LOS/NLOS**
gNB - UE	Urban Macro [94]	NLOS
gNB - Fixed IAB/NCR/RIS	Urban Macro [94][69]	NLOS
gNB - Mobile UAV w/ IAB/NCR	Urban Macro [69]	LOS
IAB/NCR/RIS - UE	Urban Micro [94][69]	NLOS
Mobile UAV w/ IAB/NCR - UE	Urban Micro [69]	LOS
UE - UE	Urban Micro [94]	NLOS

Source: Created by the author.

Table 7.2 – Entities characteristics.

Parameter	**Macro gNB**	**Fixed IAB/NCR**	**Fixed RIS**	**UAV IAB/NCR**	**UE**
Height	25 m	10 m	40 m	40 m	1.5 m
Transmit power	35 dBm	32 dBm	-	29 dBm	24 dBm
Antenna array	URA 8×8	URA 4×4 (3 panels)	URA 8×8	URA 4×4 (2 panels)	Single Antenna
Antenna elem. pattern	3GPP 3D [84]	3GPP 3D [84]	3GPP 3D [84]	3GPP 3D [84]	Omni
Max. antenna elem. gain	8 dBi	8 dBi	8 dBi	8 dBi	0 dBi
Speed	0 km/h	0 km/h	0 km/h	40 km/h	40 km/h

Source: Created by the author.

Table 7.3 – Simulation parameters.

Parameter	**Value**
Carrier frequency	28 GHz
System bandwidth	50 MHz
Subcarrier spacing	60 kHz
Number of subcarriers per PRB	12
Number of PRBs	66
Slot duration	0.25 ms
OFDM symbols per slot	14
Channel generation procedure	As described in [84, Fig.7.6.4-1]
Path loss	Eqs. in [84, Table 7.4.1-1]
Fast fading	As described in [84, Sec.7.5] and [84, Table 7.5-6]
AWGN density power per subcarrier	-174 dBm/Hz
Noise figure	9 dB
Number of UEs	8
CBR packet size	3072 bits
NCR gain	60 dB

Source: Created by the author.

7.3 Simulation results

This section presents the simulation results for the described scenario and conditions. It is divided into two parts. Subsection 7.3.1 considers the case where all HetNet nodes have a LOS link in the backhaul. Subsection 7.3.2 analyzes the impact that NLOS backhaul link causes in fixed IAB and NCR.

7.3.1 Case 1: LOS backhaul link

Figures 7.2 and 7.3 present the cumulative distribution function (CDF) of the SINR in DL (equations 6.12, 6.16 and 6.19) and UL, respectively. In the baseline scenario, i.e., the macro only scenario (dotted green curves), the UEs achieved lower values of SINR, particularly in the UL. In this direction, 80% of UEs connections had SINR lower than 2.6 dB. This result is explained by the distance between gNB and UEs (higher than 2 blocks, i.e., more than 300 m away) and the low UE transmit power. This highlights the need of improving UL links. Furthermore, we can see in figures 7.2 and 7.3 that deploying IAB nodes and NCRs as either fixed or mounted on mobile UAVs and RIS improved the SINR of the UEs in both UL and DL.

Focusing on the scenarios with fixed nodes (dashed curves), the IAB outperformed NCR and NCR outperformed RIS. One reason for this is the fact that the SINR of NCR, i.e., equation 6.16, takes into account the quality of the backhaul link, while the SINR of IAB, i.e., equation 6.12, does not. In the presented results, as listed in table 7.1, NCR had a LOS backhaul link. With NLOS backhaul, the performance difference between fixed NCR and fixed IAB is higher, as it will be presented latter. This highlights the importance of having a LOS backhaul when deploying NCRs.

Concerning specifically the UL (figure 7.3), the UEs with lower SINR had a slightly higher SINR with NCR compared to the case with IAB. This is justified by the interference of the IAB backaul in the UEs UL transmissions. In the IAB case, when the UEs operated in UL, the backhaul operated in the DL. This was not the case in the NCR scenario, where backhaul and access links operated in the same direction.

Comparing NCR and RIS, unlike NCR, the SINR of RIS, i.e., equation 6.19, did not have an amplification. It merely reflected the signal without amplification, highlighting the critical role of LOS propagation for the RIS to achieve beneficial outcomes.

Regarding specifically the scenario with RIS, we can see that the lower part of the curves is similar to the macro only case, while the higher part achieved higher values of SINR. This is justified by the fact that some UEs had higher gain than others. As explained at section 7.1, the RIS communication was optimized for an specific UE. This UE's neighbors were also benefited by the RIS, but, aside this cluster of them, the other UEs communicated directly with the macro BS, as in the macro only case, which explains the similar behaviors of the RIS and macro only curves in the low percentiles.

Comparing the cases with either IAB or NCR mounted in an UAV, the IAB was

Figure 7.2 – CDF of SINR in DL.

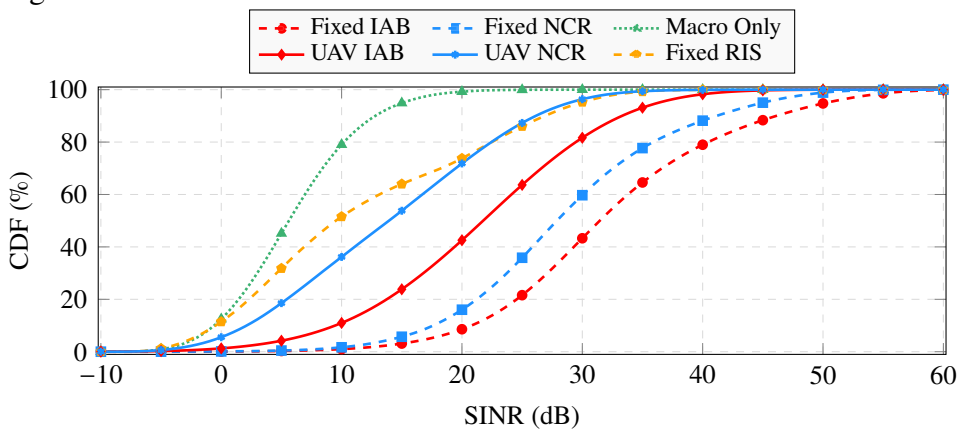

Source: Created by the author.

Figure 7.3 – CDF of SINR in UL.

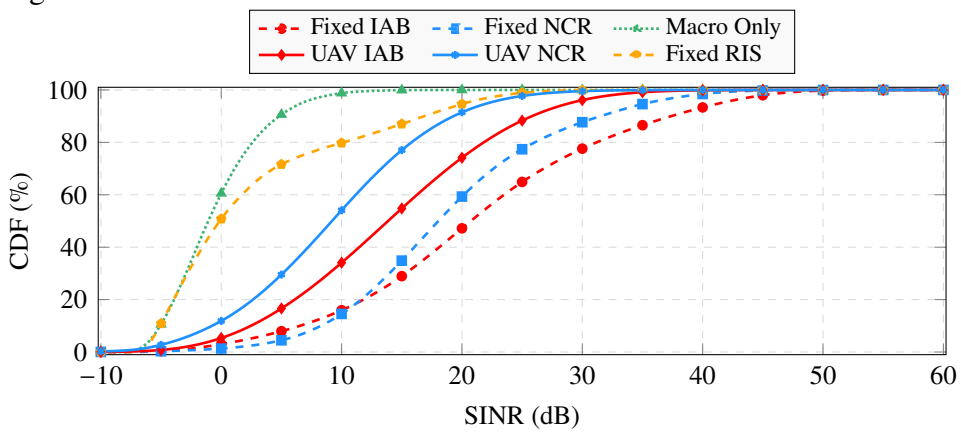

Source: Created by the author.

Table 7.4 – Impact of interference (in dB) in the system for each scenario through the difference between SNR and SINR at the 10^{th} and 90^{th} percentiles.

		Only Macros	**Fixed IAB**	**Fixed NCR**	**Fixed RIS**	**UAV IAB**	**UAV NCR**
DL	10^{th}	0.60 dB	6.07 dB	1.72 dB	2.40 dB	2.79 dB	0.89 dB
	90^{th}	0.98 dB	4.85 dB	1.69 dB	1.04 dB	1.35 dB	1.82 dB
UL	10^{th}	0.11 dB	12.63 dB	0.35 dB	0.11 dB	6.71 dB	0.16 dB
	90^{th}	0.11 dB	5.66 dB	0.21 dB	0.35 dB	4.48 dB	0.14 dB

Source: Created by the author.

superior than NCR in both directions, i.e., DL and UL. By having LOS backhaul, it was expected that the path loss in the backhaul would be small and therefore the UAV NCR's gain would be enough to compensate it, but this was not the case. Comparing the fixed and mobile, i.e., UAV, IAB and NCR cases, fixed nodes achieved higher values of SINR in the access link than the mobile UAV nodes. In DL, this is explained by the fact that the transmit power of fixed nodes is the double of the transmit power of the mobile UAV nodes. In UL, this is due to the lower distance between UEs and fixed serving nodes compared to the distance between UEs and mobile UAV nodes. Additionally, fixed nodes had the double of access panels than the mobile UAV nodes, which had only one access panel.

Table 7.4 presents the impact of interference through the difference between SNR

and SINR in each scenario. Only macros case was the one with lower level of interference. This is expected because the interference sources were only the gNB and UEs from the other cell in DL and UL, respectively.

Figure 7.4 presents the sources of interference from nodes with wireless backhaul, that is illustrated as green dashed arrow, in DL and UL. Furthermore, it is shown the area where the UEs corresponding to the 10^{th} and 90^{th} percentiles of SINR were placed, herein called UE 10^{th} and UE 90^{th}, respectively.

IAB (fixed and mounted on UAV) was the node which caused higher level of interference. The reason for that is backhaul link sharing the same resources with access link in the same cell. So, in addition to the other sources of interference also presented in the other scenarios, in the IAB case there was one source more. Figures 7.4a and 7.4b depict the sources of interference of fixed IAB in DL and UL, respectively, and figures 7.4e and 7.4f, from UAV IAB in DL and UL, respectively. Particularly, when access link was in UL, the impact of interference in IAB was higher than in DL. That did not happen in others scenarios. It was due to the backhaul link being in DL at this moment with a LOS link and the transmit node being gNB, which has higher transmit power. In that way, gNB' signal interfered directly in UEs' signals that were received by IAB. On the other hand, when the access was in DL, the IAB's MT part was transmitting in UL to gNB. Despite the MT panel is turned away from the UEs, its back lobe interferes the UEs. Furthermore, the influence of interference affected more fixed IAB than UAV IAB due to the higher fixed IAB's transmit power.

Regarding the fixed IAB and fixed NCR, figures 7.4a and 7.4b depict the IAB's sources of interference in DL and UL, respectively, and figures 7.4c and 7.4d, the NCR's sources of interference in DL and UL, respectively. These figures also indicate the position of UEs in 10^{th} and 90^{th} percentile of SINR. The UEs 10^{th} were located in front of side blocks, while the UEs 90^{th}, in front of central block. As the access' panels from IAB/NCR were pointing towards the side blocks from the other cell, the UEs 10^{th} suffered more with interference than the UEs 90^{th} in both cases and directions. In DL, the panels produced a transmission gain, while, in UL, produced a reception gain. The UEs 90^{th} received a signal from the panel's endfire producing a lower gain. Fixed IAB experienced more interference in UL, as was explained above, while fixed NCR experienced more in DL. The reason why the fixed NCR case caused more interference in DL was the fact that the transmit power of gNB was higher than that of UEs. So, in UL, the UEs' signals arrived too weak in gNB from the other cell.

As RIS is in other position and is optimized to benefit UEs belonging to a cluster, the UEs 10^{th} and 90^{th} are in a different distribution. On the one hand, because of the clustering, the UEs 90^{th} were the ones that were in the center of the cluster. On the other hand, the UEs 10^{th} were the ones that were in margins of the cluster. So, as the UEs are moving along the street, this distribution is tracking them. Figures 7.4i and 7.4j depicts the UEs' distribution and interference signals in DL and UL, respectively. In DL, UEs 10^{th} suffered more with interference than UEs 90^{th}. This happened because beam direction that most benefited the UEs 90^{th} from the neighbor

Figure 7.4 – Sources of interference.

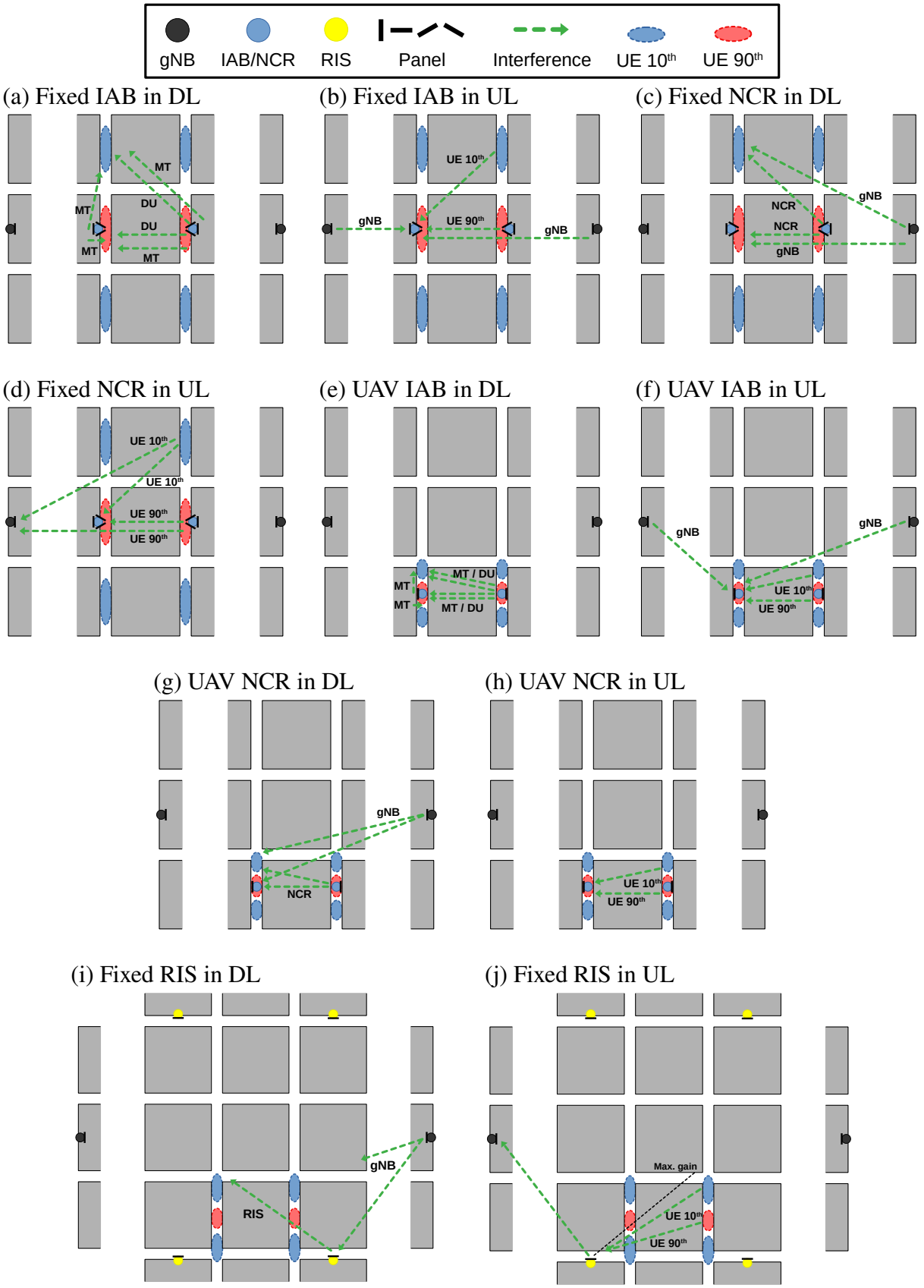

Source: Created by the author.

Figure 7.5 – Interference produced by MT panel's backlobe

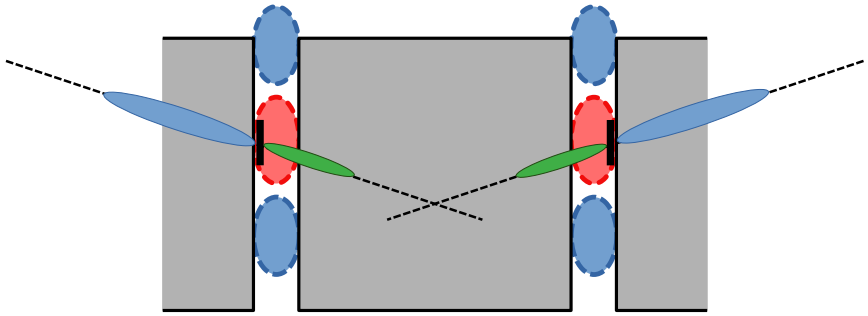

Source: Created by the author.

cell was pointing towards the margins of the UEs' cluster from the given cell, i.e., UEs 10^{th}. In UL, there was an inversion of who suffered more with interference. UEs 90^{th} experienced more interference than UEs 10^{th}. The reason is similar to the DL. As it was mentioned the beam direction that most benefited the UEs' cluster in given cell was pointing towards the UEs 10^{th}. Therefore, even these UEs had an omnidirectional transmission, the wavefront which most interfered with the UEs 90^{th} was from them. Moreover, the fact that DL had more interference than UL follows the same explanation of fixed NCR.

In UAV cases, the UEs 10^{th} and 90^{th} distribution are similar to RIS case. Figures 7.4e and 7.4f depict UAV IAB cases in DL and UL, respectively, and figures 7.4g and 7.4h, UAV NCR cases in DL and UL, respectively. As the access panel is pointed down, UAV will most benefit the UEs that are under this panel, i.e., UEs 90^{th}. The UEs 10^{th} are in the margins of that. In DL, the UEs 10^{th} were most impacted by UAV IAB, while the UEs 90^{th} were most impacted by UAV NCR. In UAV NCR case, the most powerful beam was the one that was pointing to UEs 90^{th} (UEs under the panel), consequently this signal caused more interference in the UEs that were closer in the other cell, i.e., UEs 90^{th}. However, in UAV IAB case, when access link was in DL, the MT part was transmitting to gNB, thus, the backlobe from panels of the given and neighbor cell were producing interference in UEs. As in the most part of the street, the panels from UAV IAB and gNB were not aligned, as shown in the figure 7.5, the interference affected more the UEs in the margins, i.e., UEs 10^{th}. In UL, the explanation for both cases is similar to UAV NCR in DL. Thus, the UEs 90^{th} caused more interference in UEs 10^{th}, because they were closer to other UAV.

Figures 7.6 and 7.7 present the CDF of the UEs' throughput in DL and UL, respectively. With respect to the throughput of the baseline solution, i.e., the macro only scenario, conclusions similar to the SINR analyses can be drawn. The UEs achieved lower values of throughput, particularly in the UL. In UL, 80% of UEs connections had throughput lower than 5 Mbps. Furthermore, similar to the SINR, the UEs' throughput in the macro only scenario was lower than in the cases with either IAB, NCR and RIS.

Comparing fixed IAB and fixed NCR cases, on the one hand, the UEs with already high throughput were more benefited by the NCR than by the IAB. This was due to the TDD scheme and HD mode of IAB. When a gNB transmitted a packet, in the IAB case, the UEs needed at least 2 TTIs to receive the transmitted packet, while in the NCR case, it only needed 1 TTI. On

Figure 7.6 – CDF of throughput in DL.

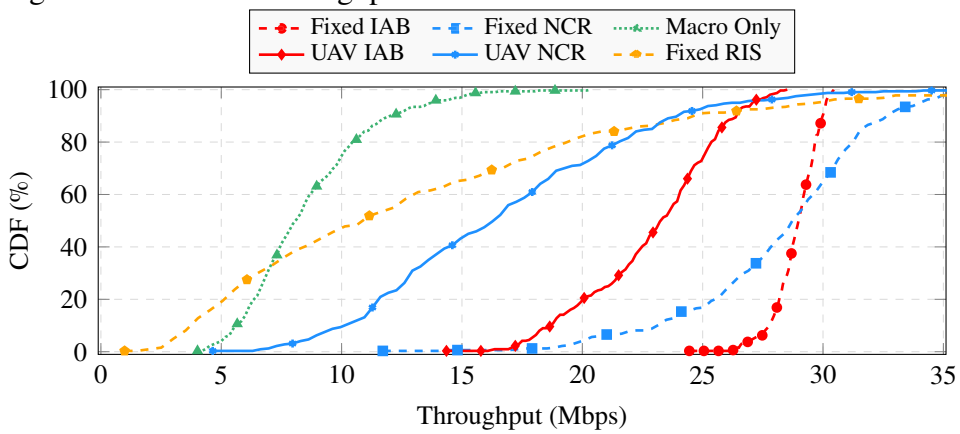

Source: Created by the author.

Figure 7.7 – CDF of throughput in UL.

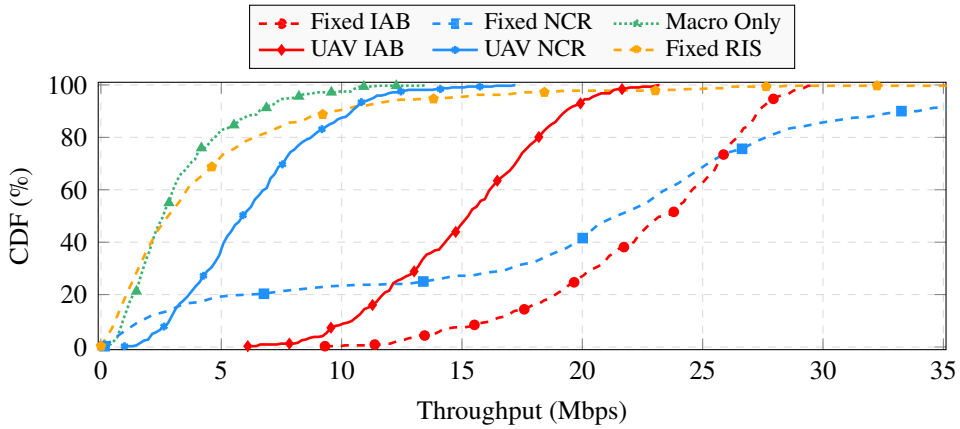

Source: Created by the author.

the other hand, the UEs with low throughput were more benefited by the IAB nodes than by the NCRs. The reason for this is that, with IAB, backhaul and access links are independent, while for the NCR, a transmission must be simultaneously successful in both backhaul and forward links, otherwise a retransmission must be performed. Thus, higher chances to need to repeat the complete transmission when using a NCR with either a bad backhaul link or a bad forward link.

Comparing the results in terms of throughput in DL and UL, we see that UEs with low throughput achieved higher gains in DL, while the UEs with high throughput achieved higher gains in UL. More precisely, in the 10^{th} percentile of the throughput, compared to the macro only case, the gains of the IAB were 22.12 Mbps (397.67%) and 15.32 Mbps (1859.76%) in the DL and the UL, respectively. For the NCR, they were 17.45 Mbps (317.02%) and 0.87 Mbps (114.63%), for the DL and UL, respectively. In the 90^{th} percentile, they were 18.05 Mbps (149.50%) and 20.86 Mbps (312.42%), for the IAB in DL and IAB in UL, respectively, and 20.76 Mbps (172.08%) and 27.17 Mbps (411.36%) for the NCR in DL and NCR in UL, respectively. The reason for this behavior is because, in DL, the UEs that were in the edge cell were receiving the signals from serving node with more power due to IAB/NCR, while, in UL, the UEs that were close to IAB/NCR had their signals received with a good quality due to the short distance, leading not to a bottleneck by the low transmit UEs power.

Figure 7.8 – MCS of UAV IAB in DL.

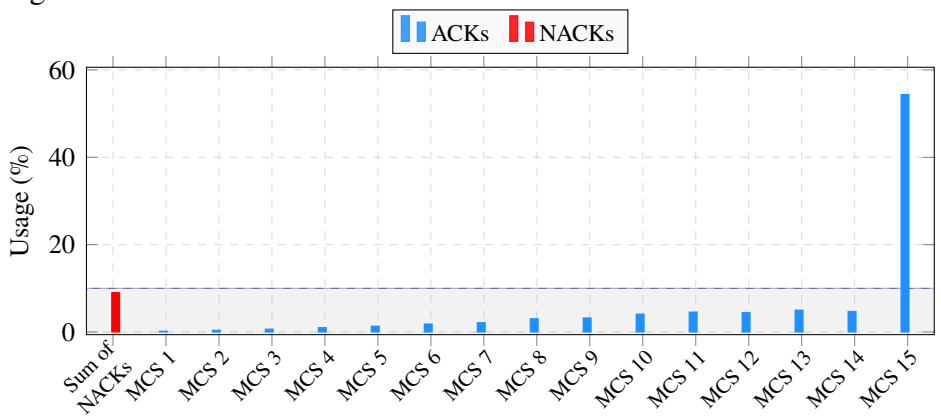

Source: Created by the author.

Figure 7.9 – MCS of UAV NCR in DL.

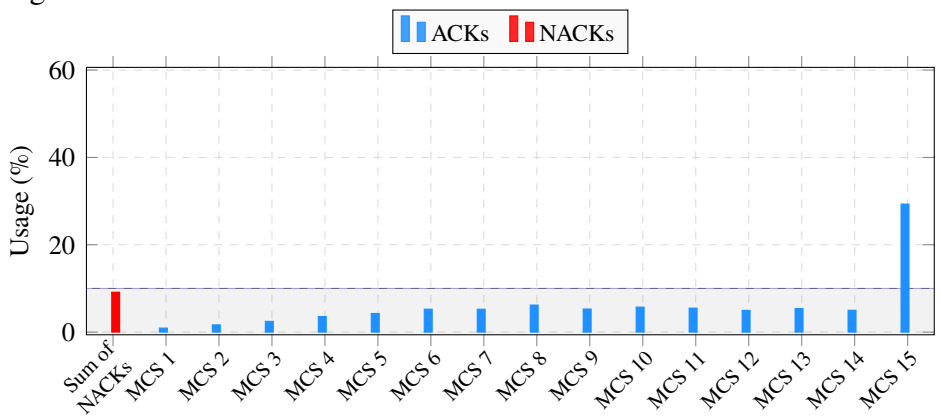

Source: Created by the author.

Concerning the RIS throughput, RIS improved the throughput of the majority of the UEs, even if it did not amplify the signal that was reflected. This was because it was able to create another path between gNB and UE to allow the signal to overcome possible obstacles presented in the LOS path. However, there were some UEs who had a worse throughput in the RIS case compared to the macro only case. This occurred because the RIS optimized the performance of a cluster of UEs, and due to their slightly spread, the gNB might have overestimated the SINR of UEs who were poorly covered by the RIS beam. This led to failed transmissions and re-attempts with adjusted SINR estimations.

Considering the UAV cases, UAV IAB outperformed UAV NCR in terms of throughput. Contrasting with the fixed case, the UAV NCR transmit power and gain were not enough to obtain a high SINR and, consequently, UAV NCR had to select lower MCSs than UAV IAB in both directions, as can be seen in figures 7.8 and 7.9, that present the MCS of UAV IAB and UAV NCR in DL, respectively, and figures 7.10 and 7.11, the MCS of UAV IAB and UAV NCR in UL, respectively. These figures present the percentage of acknowledges (ACKs) for each MCS and the aggregated percentage of no acknowledges (NACKs). ACK and NACK represent the successful and failed transmission, respectively.

Finally, Figures 7.12 and 7.13 present the Jain's fairness index in terms of UEs'

Figure 7.10 – MCS of UAV IAB in UL.

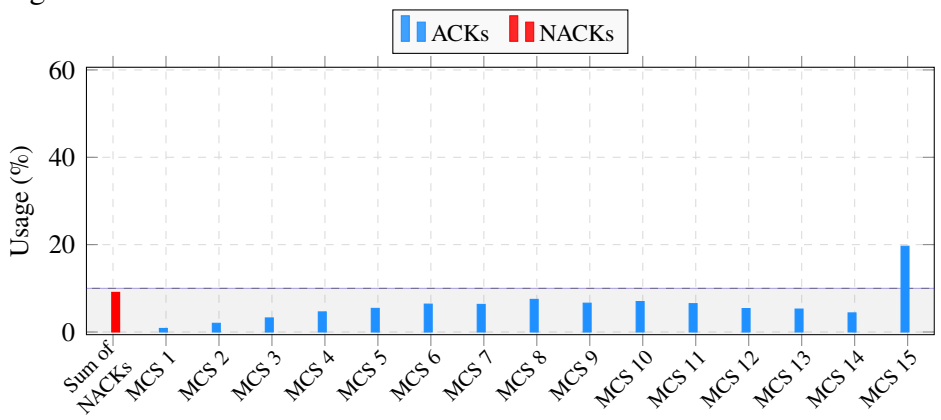

Source: Created by the author.

Figure 7.11 – MCS of UAV NCR in UL.

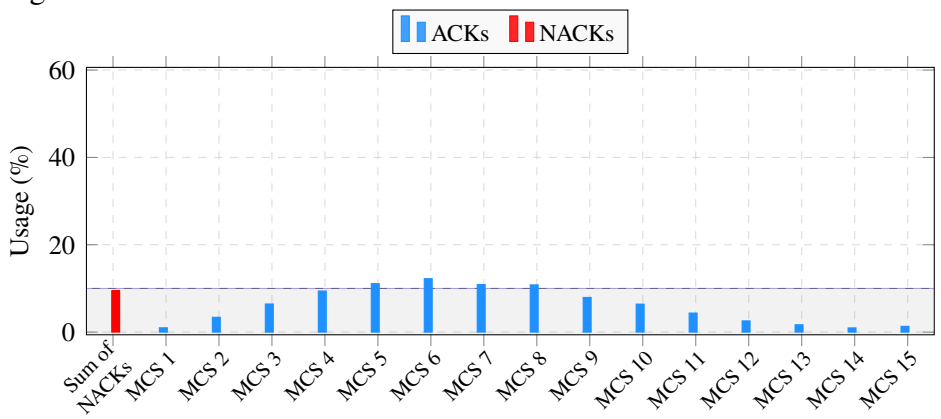

Source: Created by the author.

throughput in DL and UL, respectively. RIS had the lowest fairness between the UEs. This is due to the fact that RIS implementation benefited just a set of UEs to which the signal reflected by RIS highly improved the UEs' SINR, while, the other UEs in the system continued with low SINR being served by the gNB. In the IAB case, as explained before, UEs with high SINR gain had their gain in terms of throughput limited by the TDD schemes and HD mode (at least 2 TTIs to execute a transmission). This made the system fairer, by avoiding some UEs to have a really high throughput gain.

In summary, in this specific scenario, the fixed deployment of IAB nodes was the solution that improved the most the SINR and throughput of the worst 50% UEs in the macro only scenario. Moreover, the deployment of IAB and NCR as mobile UAVs also presented good results, but not as good as the ones achieved but the fixed deployment of IAB and NCR. In the considered study, the deployment of RIS was the solution with lower gains in terms of SINR and throughtput. Despite that, it still outperformed the macro only scenario.

In terms of impact of interference, the node which most increased the interference level was IAB (fixed and UAV). The others nodes increased a little the interference. Therefore, it is important to upgrade the IAB systems with techniques that mitigates the interference. Some possibilities are mentioned in following. The first one is to split the IAB spectrum into access

Figure 7.12 – Jain's fairness index in DL.

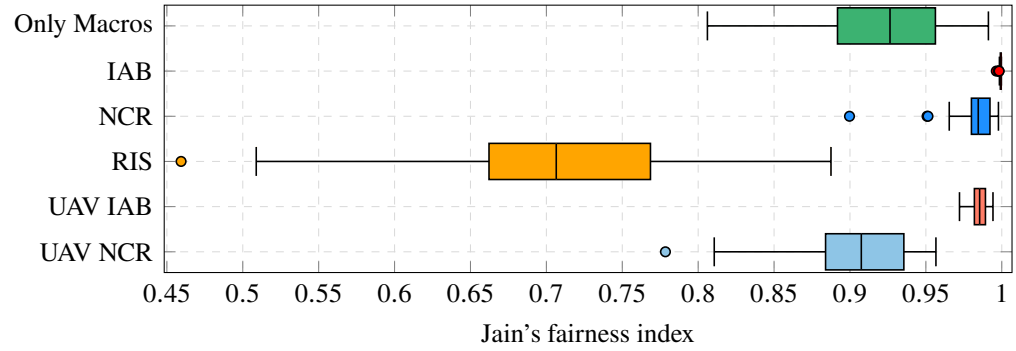

Source: Created by the author.

Figure 7.13 – Jain's fairness index in UL.

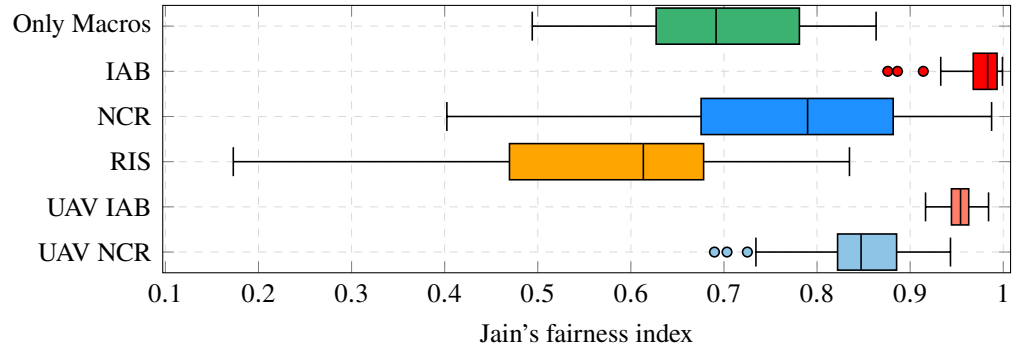

Source: Created by the author.

band and backhaul band, i.e., called as out-of-band. This solution has a trade-off between more band and less interference. As the IAB is able to estimate the access and backhaul channels, the second solution is to mitigate the interference in UL based on non-orthogonal multiple access (NOMA) and successive interference cancellation (SIC). The access and backhaul link would be considered as NOMA transmission and, with IAB channel estimations, the IAB DU part would cancel the backhaul link to have the access link, while the IAB MT part would cancel the access link to have the backhaul link. Finally, third one is to use power control allocation to reduce the power level in the system, consequently, the interference level too.

7.3.2 Case 2: Impact of NLOS backhaul link in IAB/NCR

Figure 7.14 presents the CDF of the SINR in DL (equations 6.12 and 6.16) with NLOS backhaul link for fixed IAB/NCR. It is also included the fixed IAB/NCR and UAV IAB/NCR with LOS backhaul link. They are presented again to show the losses that NLOS backhaul may bring for each solution.

Comparing the performance of the fixed nodes, the IAB outperformed the NCR. The main reason is the fact that the SINR of IAB, as it was expressed in equation (6.12), does not take into account the backhaul link in the useful power $S^{IAB}_{u_x,k}$, different from the NCR. Furthermore, with the change from LOS to NLOS, NCRs have a loss in SINR of 30.05 dB and 21.13 dB in 90^{th} and 10^{th} percentile, respectively. Despite the fact that IAB does not consider the backhaul link in the useful power $S^{IAB}_{u_x,k}$ and, when access link is DL, the backhaul link is not

Figure 7.14 – CDF of SINR of fixed IAB and NCR with LOS/NLOS backhaul in DL.

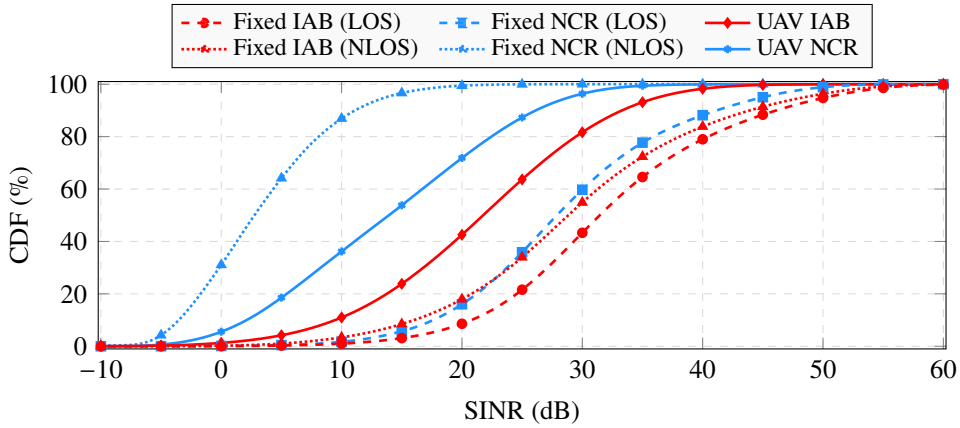

Source: Created by the author.

an interference source, there is a slight loss in change from LOS to NLOS. IAB have a loss in SINR of 2.21 dB and 4.76 dB in 90th and 10th percentile, respectively. As SINR only counts the happening transmissions, thus, in LOS case, the backhaul was with intensive traffic of bits for UEs, always having data to send, while, in the NLOS case, the IAB only transmitted bits what it had. This benefits more the UEs with high SINR, what justifies the impact to be lower these UEs.

Concerning with UAV nodes, they also had a superior performance than fixed NCR. This highlights the importance of network planning. A dense urban scenario, where there are many sources of blockage, is an opportunity to deploy IAB/NCR mounted in UAV, which has more chances of LOS backhaul link.

Figures 7.15 presents the CDF of the UEs' throughput in DL in NLOS backhaul link case for IAB/NCR. It is also included the fixed IAB/NCR and UAV IAB/NCR with LOS backhaul link. With respect to the throughput of the fixed NCR solution, conclusions similar to the SINR analyses can be drawn. The UEs achieved lower values of throughput. Furthermore, with the change from LOS to NLOS, NCR have a loss in throughput of 25.02 Mbps (77%) and 22.29 Mbps (96%) in 90th and 10th percentiles, respectively. Regarding fixed IAB, the change from LOS to NLOS make the throughput spread in the plot. This confirms the fact that backhaul was a bottleneck in the system. Furthermore, with the change from LOS to NLOS, IAB have a loss in throughput of 1.49 Mbps (5%) and 25.93 Mbps (93%) in 90th and 10th percentiles, respectively. Corroborating with what was presented in SINR.

Regarding the MCS of fixed nodes, figures 7.16a and 7.16d present the MCS of NCR's access in LOS and NLOS, respectively. In NLOS, it was necessary to change the MCS of the majority of the transmissions from MCS 15 to about MCS 4 due to the losses in backhaul. Figures 7.16b and 7.16e present the MCS of IAB's access for the LOS and NLOS backhaul cases, respectively. As the access links did not change, the MCS was similar in both cases. Figures 7.16c and 7.16f present the MCS of IAB's backhaul in LOS and NLOS, respectively. These results clearly present the impact caused by the change in backhaul condition. While, in LOS backhaul link, the majority of the transmissions used MCS 15, in NLOS backhaul link, the choice of

Figure 7.15 – CDF of throughput of fixed IAB and NCR with LOS/NLOS backhaul in DL.

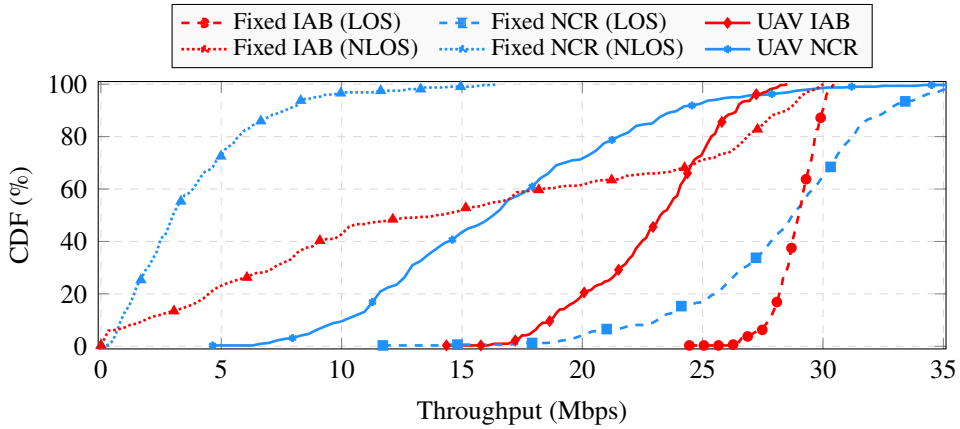

Source: Created by the author.

MCS was more uniformly distributed between them. It caused a bottleneck in data traffic in the backhaul.

In summary, the impact of changing the backhaul link affected the two nodes, i.e. IAB and NCR. On the one hand, NCR had a severe impact since the useful power for UE considers the two links, i.e., backhaul and access links. On the other hand, the backhaul became a bottleneck for IAB causing the decrease of the UEs' data rate. UAV showed up as an alternative in a dense urban scenario where the LOS backhaul link is not guaranteed. Next chapter focuses on the performance of fixed NCR with NLOS backhaul link and the impact on the interference in a neighbor cell.

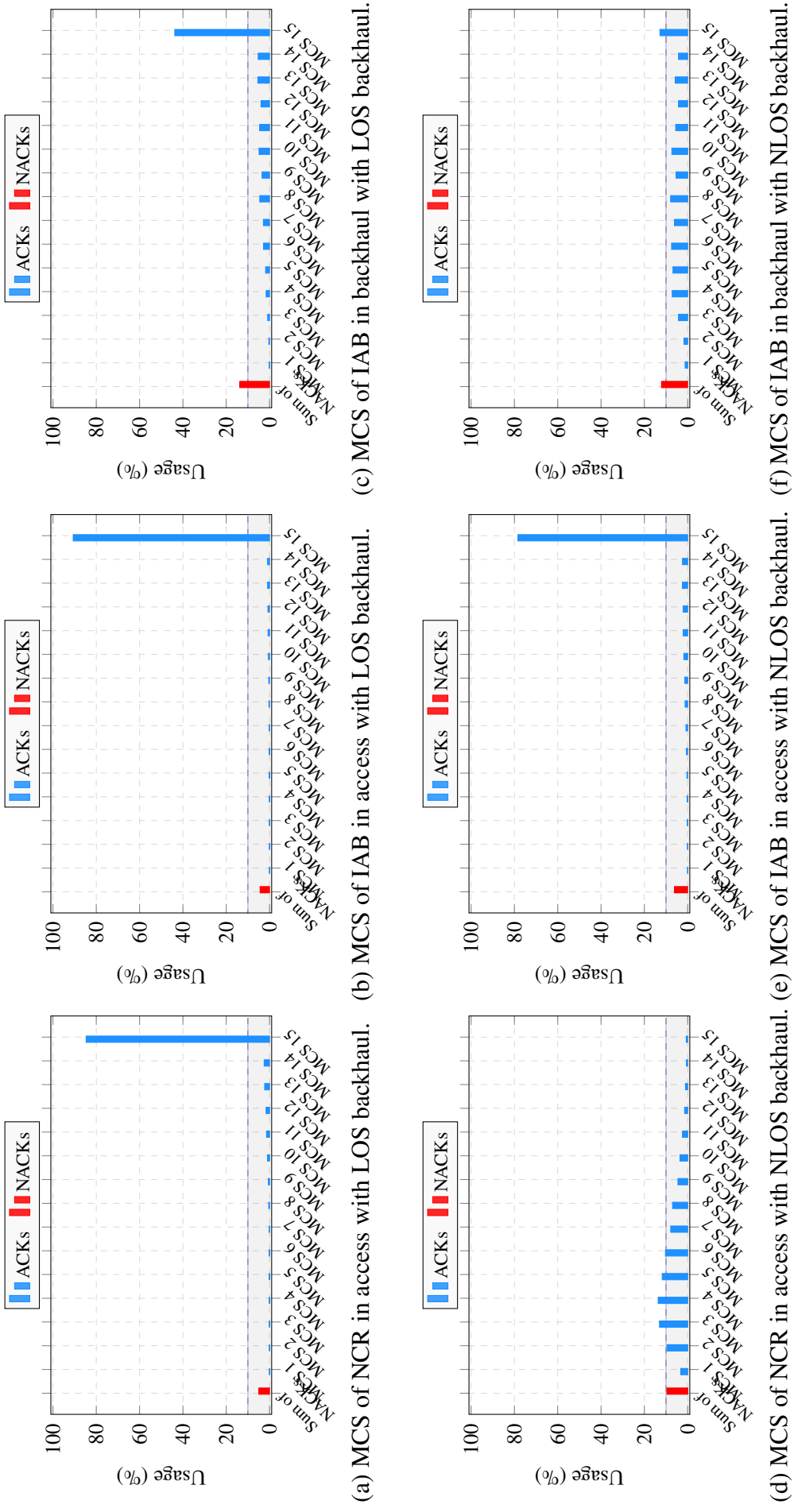

(a) MCS of NCR in access with LOS backhaul. (b) MCS of IAB in access with LOS backhaul. (c) MCS of IAB in backhaul with LOS backhaul.

(d) MCS of NCR in access with NLOS backhaul. (e) MCS of IAB in access with NLOS backhaul. (f) MCS of IAB in backhaul with NLOS backhaul.

Figure 7.16 – NCR protocol stack.

8 PERFORMANCE IMPROVEMENT OF SERVING CELL WITH NCR AND INTERFERENCE IMPACT ON NEIGHBOR CELLS

8.1 Specific system model

As illustrated in figure 8.1, consider a scenario with two gNBs, i.e., b_1 and b_2, operating at the same frequency. The inter-site distance (ISD) between them is equal to $2R$. Also, consider that there is one UE close to each cell edge, i.e., UEs u_1 and u_2 at cells of gNBs b_1 and b_2, respectively. In the cell of gNB b_2, an NCR is deployed between b_2 and UE u_2 to enhance the link serving u_2 as shown in figure 8.1. Moreover, consider that UE u_1 always connects directly to gNB b_1, while UE u_2 connects to gNB b_2 either directly or through the NCR.

Figure 8.1 – Scenario with two gNBs (distant $2R$ from each other) and two UEs, connected to different gNBs. Moreover, it is considered that one of the gNBs controls an NCR, which is deployed between its controller gNB and its serving UE.

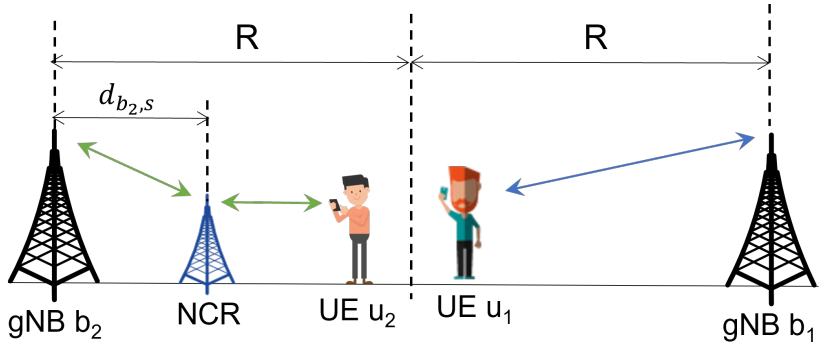

Source: Created by the author.

When gNB b_2 serves UE u_2 via NCR s, the NCR transmit power $p_{s,u_2,k}$ to UE u_2 on PRB k is equal to the NCR total receive power amplified by a gain $g_{s,k}$, limited by the NCR maximum transmit power $p_{s,k}^{\text{MAX}}$ per PRB.

Remind that, as defined in chapter 6, $\gamma_{i,j,k} = \mathbf{d}_{j,k}\mathbf{H}_{i,j,k}\mathbf{f}_{i,k}$ denotes the combined effect (applied to a signal transmitted by node i to node j at PRB k) of the channel $\mathbf{H}_{i,j,k}$ after the transmission and reception filters $\mathbf{f}_{i,k}$ and $\mathbf{d}_{j,k}$, respectively. Thus, we define the NCR total receive power as the sum of the useful power $S_{s,k} = \gamma_{b_2,s,k} \cdot p_{b_2,u_2,k}$, the noise $N_{s,k} = \sigma_k^2$ and the interfering power $I_{s,k} = \gamma_{b_1,s,k} \cdot p_{b_1,u_1,k}$.

So, the transmit power $p_{s,u_2,k}$ of NCR s on PRB k to UE u_2 can be expressed as

$$p_{s,u_2,k} = \min\left\{p_{s,k}^{\text{MAX}}, g_{s,k}\left(S_{s,k} + N_{s,k} + I_{s,k}\right)\right\}. \tag{8.1}$$

We consider that the NCR gain $g_{s,k}$ can be either fixed or dynamic[1]. When using the

[1] Only NCR fixed gain has been specified by the 3GPP. So, while we try to mimic the model specified by 3GPP Rel-18, the considered setup may have differences with Rel-18 NCR.

dynamic gain, the NCR transmit power $p_{s,u_2,k}$ is always equal to the NCR maximum transmit power $p_{s,k}^{\mathrm{MAX}}$. For this, the dynamic gain is defined as the ratio between the NCR maximum transmit power, i.e., $p_{s,k}^{\mathrm{MAX}}$, and NCR total receive power, i.e., the sum of the useful power $S_{s,k}$, the noise $N_{s,k}$ and the interfering power $I_{s,k}$. We remark that the NCR does not need to know the values of $S_{s,k}$, $I_{s,k}$ and $N_{s,k}$, separately. It just need to know their sum, which is known since it is the total input power that it receives. Thus, the dynamic gain $g_{s,k}^{\mathrm{DYN}}$can be expressed as

$$g_{s,k}^{\mathrm{DYN}} = \frac{p_{s,k}^{\mathrm{MAX}}}{S_{s,k} + N_{s,k} + I_{s,k}}. \tag{8.2}$$

Regarding the fixed gain, i.e., $g_{s,k}^{\mathrm{FIX}}$, it amplifies the total received power with a fixed value, e.g., 90 dB. When the fixed gain implies an NCR total transmit power higher than its ceiling $p_{s,k}^{\mathrm{MAX}}$, the NCR works in a saturated mode. In this mode, it behaves similar to the dynamic gain, where the NCR transmit power $p_{s,u_2,k}$ is equal to the NCR maximum transmit power $p_{s,k}^{\mathrm{MAX}}$.

In the scenario considered in this chapter, regarding $S_{u_i,k}$, on the one hand, for UE u_1, the only useful signal received is the one coming from gNB b_1, thus

$$S_{u_1,k} = \gamma_{b_1,u_1,k} \cdot p_{b_1,u_1,k}. \tag{8.3}$$

On the other hand, u_2 may receive two components of useful signal, one coming directly from b_2 and other being amplified and forwarded by the NCR, as presented in equation (6.13) in a general form.

Similarly, concerning the interference component, in the considered scenario, on the one hand, for UE u_2 there is only one source of interference, which is the signal sent by gNB b_1 to UE u_1. On the other hand, for UE u_1, there are two sources of interference, which are the the signal sent by gNB b_2 to UE u_2 and its version amplified by NCR s. As presented in chapter 6, the precise value of these interference components can be obtained from equation equation (6.14).

Finally, regarding the noise component, for UE u_1, we have

$$N_{u_1,k} = \sigma_k^2, \tag{8.4}$$

and for UE u_2, it is given by equation (6.15).

8.2 Simulation assumptions

As presented in chapter 6, the considered channel model was based on 3GPP channel model standardized in [94] and [69]. Concerning the frequency domain, the carrier was centered at 28 GHz with subcarrier spacing of 60 kHz. Regarding the time domain, the slots had a duration of 0.25 ms. A TDD scheme was adopted, where downlink and uplink slots alternated in time. Other channel characteristics are listed in tables 8.1 and 8.2.

With respect to the link adaptation, it was considered a target BLER of 10% and the CQI/MCS mapping curves standardized in [92]. An outer loop strategy was considered to avoid

Table 8.1 – Characteristic of the links

Link	**Scenario**	**LOS/NLOS**
gNB - UE	Urban Macro	NLOS
gNB - NCR	Urban Macro	NLOS
NCR - UE	Urban Micro	LOS

Source: Created by the author.

Table 8.2 – Simulation parameters.

Parameter	**Value**
Carrier frequency	28 GHz
Subcarrier spacing	60 kHz
Number of subcarriers per RB	12
Number of RBs	1
Slot duration	0.25 ms
OFDM symbols per slot	14
Channel generation procedure	As described in [84, Fig.7.6.4-1]
Path loss	Eqs. in [84, Table 7.4.1-1]
Fast fading	As described in [84, Sec.7.5] and [84, Table 7.5-6]
AWGN density power per subcarrier	-174 dBm/Hz
Noise figure	9 dB
CBR packet size	3072 bits
Inter-site distance (2R)	400 m
Distance between gNB and UE	150 m

Source: Created by the author.

Table 8.3 – Entities characteristics.

Parameter	**Macro gNB**	**NCR**	**UE**
Height	25 m	10 m	1.5 m
Transmit power	16.8 dBm	13.8 dBm	5.8 dBm
Antenna array	URA 8×8	URA 8×8 (2 panels)	Single Antenna
Antenna element pattern	3GPP 3D [84]	3GPP 3D [84]	Omni
Max. antenna element gain	8 dBi	8 dBi	0 dBi

Source: Created by the author.

the increase of the BLER. More precisely, when a transmission error occurred, the estimated SINR decreased 1 dB, however, when a transmission occurred without error, the estimated SINR had its value added by 0.1 dB.

The gNBs and the NCR transmissions were performed with a DFT codebook based beamforming, where for each transmission a beam management was performed in order to identify the best transmitter beam to be used when serving the UEs. Other nodes characteristics are presented in table 8.3.

Figure 8.2 – Impact of NCR position on the SNR (90th percentile) of both UEs for two types of NCR gain, i.e., dynamic and fixed.

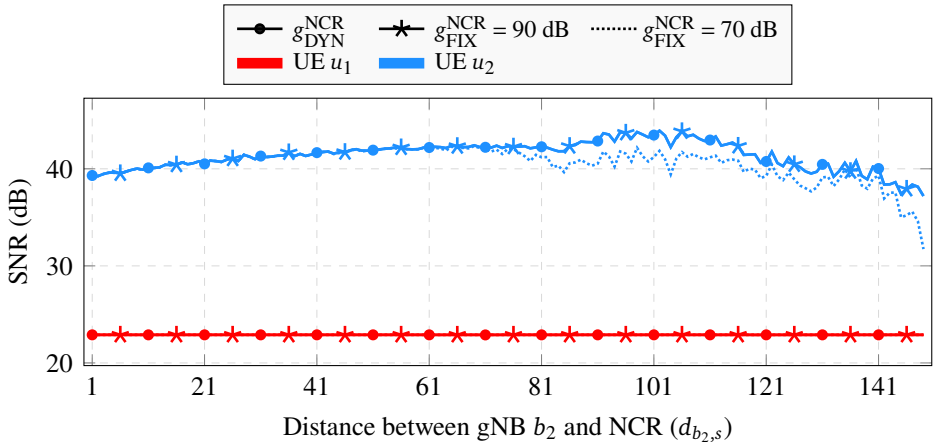

Source: Created by the author.

Figure 8.3 – Impact of NCR position on the SNR (10th percentile) of both UEs for two types of NCR gain, i.e., dynamic and fixed.

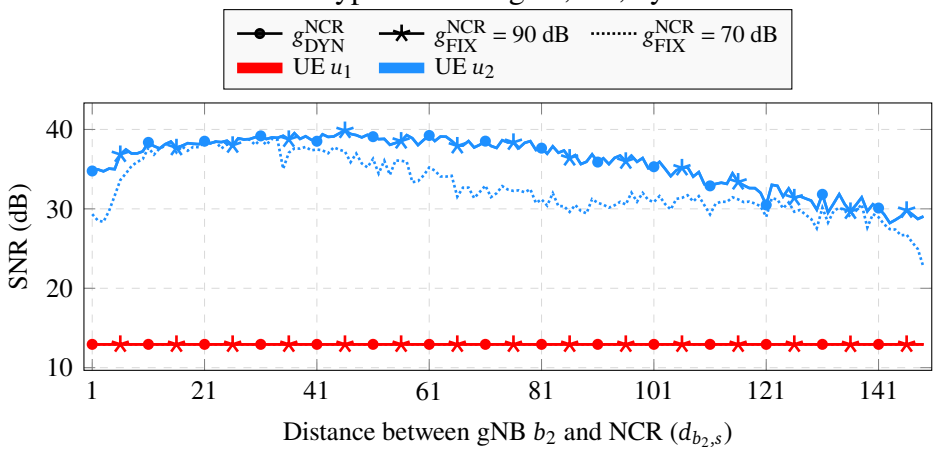

Source: Created by the author.

8.3 Simulation results

Figures 8.2 and 8.3 show the impact of NCR position on the SNR (90th percentile and 10th percentile, respectively) of UEs u_1 and u_2. Both figures present the results for the two possibilities of the NCR gain: dynamic and fixed. For the fixed case, we considered two gain values: 70 dB and 90 dB. Considering the positions of u_2 and b_2 fixed, the x-axis represents the possible distance between the NCR and b_2. As expected, the SNR of u_1 does not depend on the position of the NCR. Also, notice that the SNR of u_2, in the beginning, increases and, after a certain distance, starts to decrease. This is due to the product of the two pathlosses in equation (6.13), that are incorporated in the matrix channels $\mathbf{H}_{s,u_2,k}$ and $\mathbf{H}_{b_2,s,k}$ in $\gamma_{s,u_2,k} = \mathbf{d}_{u_2,k}\mathbf{H}_{s,u_2,k}\mathbf{f}_{s,u_2}$ and $\gamma_{b_2,s,k} = \mathbf{d}_{s,k}\mathbf{H}_{b_2,s,k}\mathbf{f}_{b_2,k}$, respectively. Thus, unlike what one could expect, deploying a NCR closer to the serving UE does not always mean a better connection. In other words, one could expect that the closer a UE is to a NCR the higher its SNR would be due to the shorter distance, and so lower the path loss, however as shown in figures 8.2 and 8.3, this is not true.

Due to the symmetry of the scenario presented in figure 8.1, without the NCR, u_1 and

Figure 8.4 – Impact of NCR position on the SINR (90th percentile) of both UEs for two types of NCR gain, i.e., dynamic and fixed.

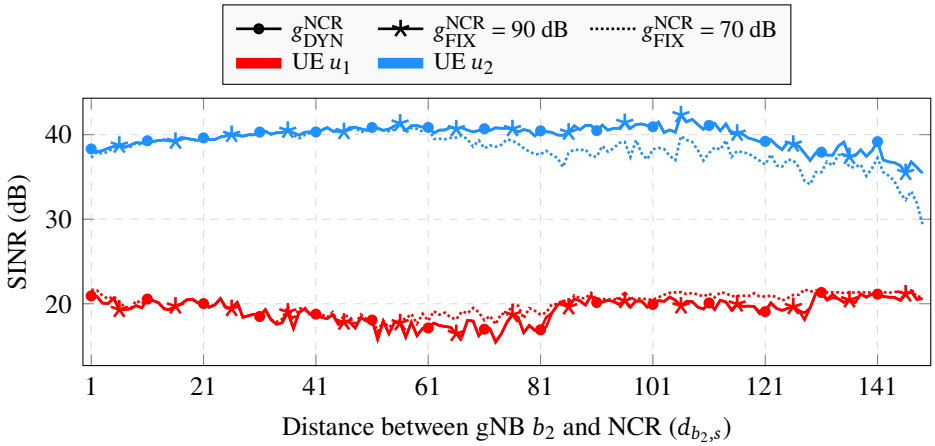

Source: Created by the author.

Figure 8.5 – Impact of NCR position on the SINR (10th percentile) of both UEs for two types of NCR gain, i.e., dynamic and fixed.

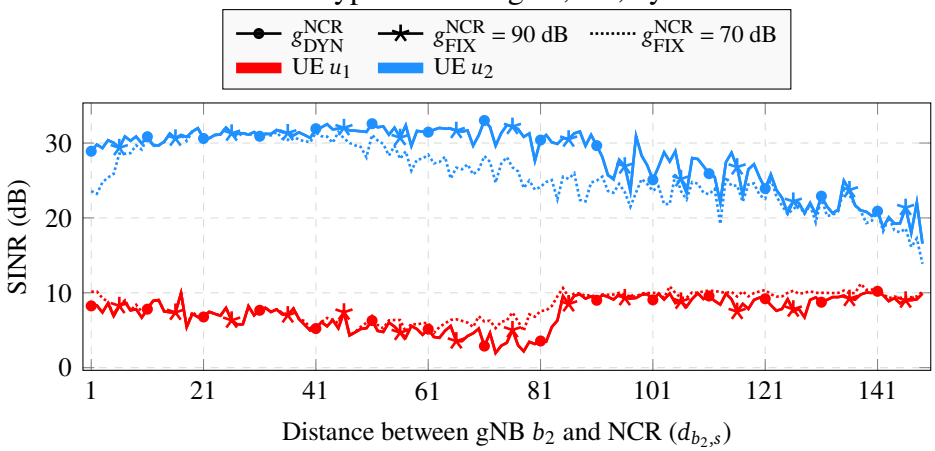

Source: Created by the author.

u_2 should present similar values of SNR and SINR. Thus, by comparing the curves related to u_1 and u_2 in figures 8.2 and 8.3, we can see that the deployment of an NCR considerably improves the SNR perceived by u_2. More specifically, compared to the SNR of u_1, the SNR perceived by u_2 increases in at least 15 dB due to the deployment of the NCR. Moreover, notice that the case with fixed NCR gain equal to 90 dB presented results similar to the dynamic case, which means that for 90 dB, the NCR operated in its saturated mode.

Figures 8.4 and 8.5 are similar to figures 8.2 and 8.3, the main difference is that figures 8.4 and 8.5 focus on SINR instead of SNR. Notice, in figures 8.4 and 8.5, the trend discontinuity on the SINR of u_1 when the distance between the NCR and b_2 is approximately 81 m. This is explained by the change in the interference coming from the NCR. More specifically, around that distance the beam used by the NCR to serve u_2 changes creating a new interference pattern on u_1. Figure 8.6 illustrates this behavior.

Figure 8.6 presents the impact of the distance between b_2 and the NCR on the interference suffered by u_1 (y-axis of left-hand side) and on the beam index that is used to serve

Figure 8.6 – Comparison between the interference and amplified noise by NCR in the u_1 and the change in the codebook indexes of the NCR-Fwd.

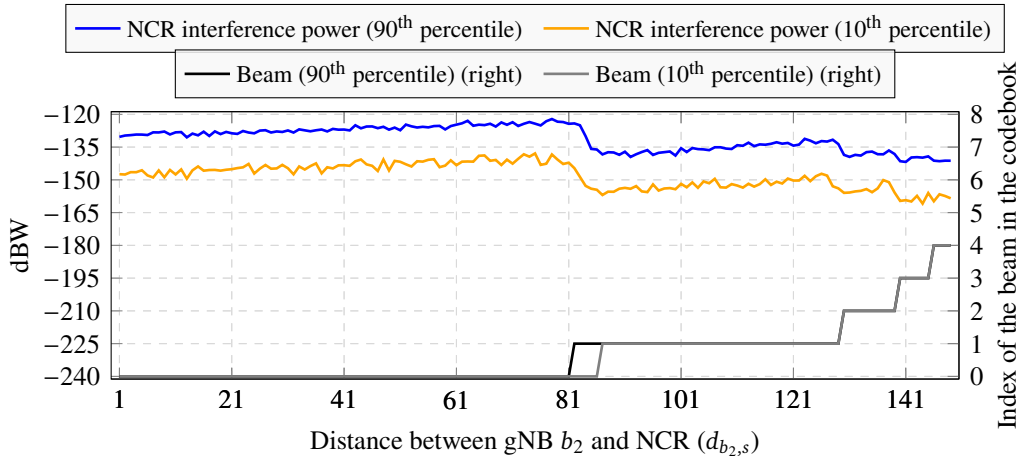

Source: Created by the author.

u_2 (y-axis of right-hand side). In this figure, we can notice that the interference suffered by u_1 has a discontinuity when the distance between b_2 and the NCR is around 81 m. Around this position, the NCR beam serving u_2 changes from 0 to 1. Beam 0 points in a direction closer to u_1 than Beam 1, that is why when changing from Beam 0 to Beam 1, the interference decreases. This can be seen as a spatial filtering.

Furthermore, notice, in figure 8.6, that within the distance ranges 0 m to 81 m and 81 m to 150 m, the interference suffered by u_1 increases when the NCR distance between b_2 and the NCR increases. This is explained by the approximation of the NCR to u_1.

Finally, Figs. 8.7 and 8.8 present the impact of the distance between b_2 and the NCR on the spectral efficiency of the transmissions to u_1 and u_2. The maximum spectral efficiency that a transmission could achieve is:

$$= \frac{\dfrac{\text{subcarriers per PRB} \cdot \text{symbols per PRB} \cdot \text{effective rate}}{\text{PRB time} \cdot \text{PRB bandwidth}}}{} = \frac{12 \cdot 14 \cdot 5.5547}{0.25 \cdot 10^{-3} \cdot 12 \cdot 60 \cdot 10^{3}} = 5.18 \text{ bits/s/Hz}, \tag{8.5}$$

where 5.5547 corresponds to the effective rate associated to the CQI index 15 in [92]. Remark that u_2 achieves the maximum spectral efficiency in the majority of the considered cases, while u_1 achieves lower values, but that are still high enough to allow the communication.

Figure 8.7 – Spectral efficiency (90$^{\text{th}}$ percentile) of the both UEs and with different types of NCR gain.

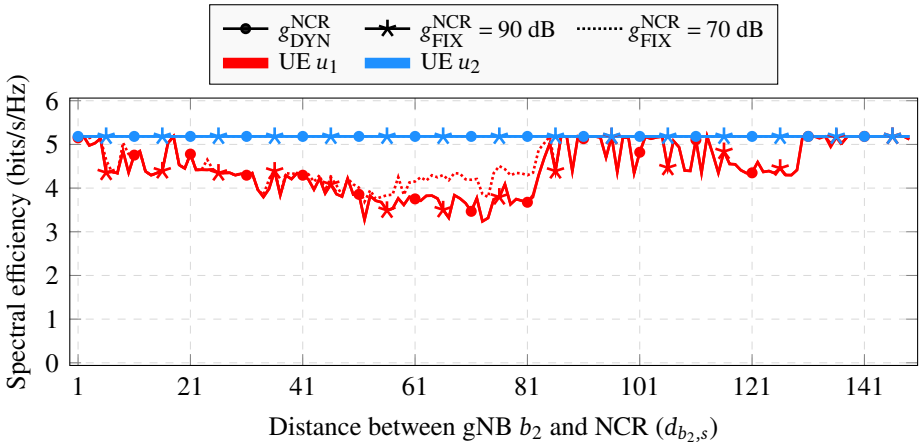

Source: Created by the author.

Figure 8.8 – Spectral efficiency (10$^{\text{th}}$ percentile) of the both UEs and with different types of NCR gain.

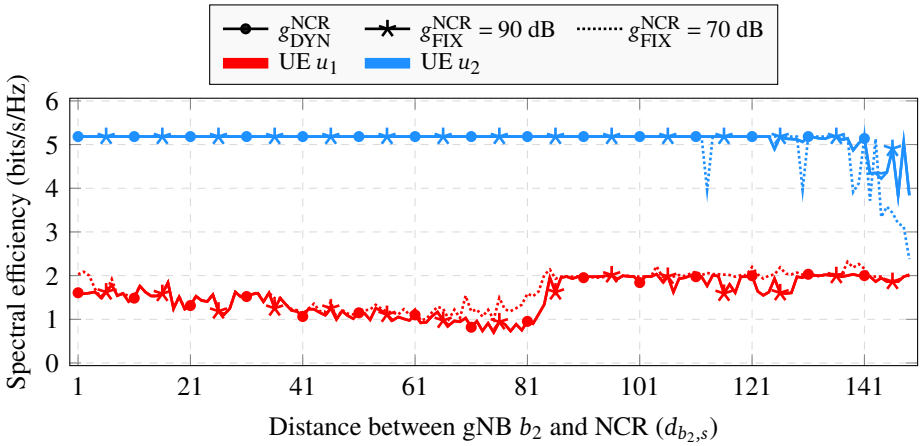

Source: Created by the author.

9 CONCLUSION

In light of the growing need for network densification, nodes with wireless backhaul have emerged as a compelling solution. This is due to its advantages compared to traditional gNBs, such as, lower price and shorter time required to be deployed, as it was presented in chapter 1. This work provided an overview of some of these wireless backhaul nodes, i.e., IAB, NCR and RIS.

Chapter 2 discussed the IAB concept. It was presented an overview of the topic, addressing its architecture, node integration to the network and use of the spectrum. It was shown the new sublayer protocol BAP that is responsible for identification and routing in IAB. Finally, it was presented a literature review of some important research in the area.

Chapter 3 presented the NCR. It were discussed the main aspects related to the evolution from RF repeater to NCR. It was shown that the NCR architecture is divided in two part, i.e, NCR MT and NCR Fwd. Furthermore, it was also presented the content of the side control information, e.g., beamforming information, timing information, information on UL-DL TDD configuration and ON-OFF information. Finally, it was presented some research's topics about NCR.

Chapter 4 addressed the RIS concept. It was presented the possible RIS operation mode, such as, reflection, refraction, absorption and backscattering. Architecture and RIS path loss were also presented. Moreover, some works in this area were discussed.

Chapter 5 presented some aspects related to UAVs. It was shown that UAV can operate in two modes, i.e., aerial BS/relay or aerial UE. UAVs were classified according to their altitude of operation, wing design and network deployment. Furthermore, a literature review was presented on UAVs that give aerial mobility to nodes with wireless backhaul.

Chapter 6 presented the common link and system level models that were utilized in this work. It was shown the adopted simulation toolbox as its main features. Some of the detailed aspects were: 5G physical layer (comparing with 4G LTE), 5G channel model, physical layer measurements and resource allocation. It also was formulated the expression of SINR for IAB, NCR and RIS in scenario with multiples nodes.

Chapter 7 analyzed the performance of wireless backhaul nodes in a scenario where an outdoor sport event was taking place. It was compared the performance of the deployment of fixed IAB, fixed NCR fixed RIS, mobile IAB and mobile NCR. Furthermore, it was also analyzed the deployment of these nodes mounted on UAVs to address potential NLOS backhaul links of the fixed terrestrial deployments due to blockages. Moreover, it was studied the impact of NLOS backhaul link in comparison to LOS backhaul link in fixed IAB and NCR cases.

Based on the presented analyses, it was concluded that both fixed and mobile (UAV-mounted) deployments of IAB and NCR and fixed RIS offer effective solutions for extending coverage to UEs placed at cell edge, obstructed areas and beyond. These technologies also enable

the quick deployment of new cells, thereby enhancing connectivity in high-demanding zones.

The deployment of network elements on mobile UAVs is an interesting solution. This approach can be particularly valuable in scenarios where establishing a LOS link between a gNB and an IAB/NCR/RIS is hindered by obstructions. Moreover, the change from NLOS to LOS in IAB and NCR fixed deployments yielded a significant impact on their performance. The most affected was NCR due to direct influence of backhaul in useful power for UEs. Thus, it is important to highlight that these technologies rely on a network planning. Each environment will require a specific network topology with or without the coexistence of these nodes.

Chapter 8 focused on the deployment of a NCR and its impact on a neighbor cell. More specifically, it was evaluated the impact of different positions for the NCR and of the considered value of the NCR gain. As expected, the NCR improved the link quality of its serving UE. However, unlike what one could expect, deploying a NCR closer to its serving UE did not necessarily meant a better connection. There is a trade-off given by the product between its distance to its serving gNB and its distance to the UE that it is serving. It was also shown that the interference caused on neighbor cells can be mitigated by spatial filtering by means of appropriate beam management.

REFERENCES

1 ERICSSON. **Mobile data traffic outlook**. Available from: <https://www.ericsson.com/en/reports-and-papers/mobility-report/dataforecasts/mobile-traffic-forecast>. Visited on: 10 May 2024.

2 3GPP. **NR; NR and NG-RAN Overall description; Stage 2**. [S.l.], Dec. 2019. v.15.8.0. Available from: <http://www.3gpp.org/ftp/Specs/html-info/38300.htm>. Visited on: 17 Feb. 2020.

3 FLAMINI, R. et al. Towards a Heterogeneous Smart Electromagnetic Environment for Millimeter-Wave Communications: An Industrial Viewpoint. **IEEE Transactions on Antennas and Propagation**, v. 70, n. 10, p. 8898–8910, Feb. 2022. DOI: 10.1109/TAP.2022.3151978.

4 RANGAN, S.; RAPPAPORT, T. S.; ERKIP, E. Millimeter-Wave Cellular Wireless Networks: Potentials and Challenges. **Proceedings of the IEEE**, v. 102, n. 3, p. 366–385, 2014. DOI: 10.1109/JPROC.2014.2299397.

5 AYOUBI, R. A. et al. **Network-Controlled Repeaters vs. Reconfigurable Intelligent Surfaces for 6G mmW Coverage Extension**. Nov. 2022. arXiv: 2211.08033.

6 MONTEIRO, V. F. et al. Paving the Way Towards Mobile IAB: Problems, Solutions and Challenges. **IEEE Open Journal of the Communications Society**, v. 3, p. 2347–2379, Nov. 2022. DOI: 10.1109/OJCOMS.2022.3224576.

7 3GPP. **Overview of 3GPP Release 10**. [S.l.], June 2014. v.0.2.1. Available from: <https://www.3gpp.org/ftp/Information/WORK_PLAN/Description_Releases/Rel-10_description_20140630.zip>.

8 JABER, M. et al. 5G Backhaul Challenges and Emerging Research Directions: A Survey. **IEEE Access**, v. 4, p. 1743–1766, 2016.

9 CZEGLEDI, C. B. et al. **Demonstrating 139 Gbps and 55.6 bps/Hz Spectrum Efficiency Using 8×8 MIMO over a 1.5-km Link at 73.5 GHz**. In: PROCEEDINGS of the IEEE MTT-S International Microwave Symposium (IMS). [S.l.: s.n.], 2020. P. 539–542.

10 TEZERGIL, B.; ONUR, E. Wireless Backhaul in 5G and Beyond: Issues, Challenges and Opportunities. **IEEE Communications Surveys and Tutorials**, v. 24, n. 4, p. 2579–2632, 2022.

11 3GPP. **NR; Study on Integrated Access and Backhaul (Release 16)**. [S.l.], Dec. 2018. v.16.0.0. Available from: <http://www.3gpp.org/ftp/Specs/html-info/38874.htm>. Visited on: 13 Apr. 2021.

12 3GPP. **NR; Integrated access and backhaul radio transmission and Reception**. [S.l.], Sept. 2023. v.18.2.0. Available from: <http://www.3gpp.org/ftp/Specs/html-info/38174.htm>. Visited on: 16 June 2023.

13 MADAPATHA, C. et al. On Integrated Access and Backhaul Networks: Current Status and Potentials. **IEEE Open Journal of the Communications Society**, v. 1, p. 1374–1389, Sept. 2020. DOI: 10.1109/OJCOMS.2020.3022529.

14 3GPP. **Study on NR network-controlled repeaters**. [S.l.], Sept. 2022. v.18.0.0. Available from: <http://www.3gpp.org/DynaReport/38867.htm>.

15 RWS-210019: NR Smart Repeaters. [S.l.: s.n.], 2021. Qualcomm.

16 ETSI. **Reconfigurable Intelligent Surfaces (RIS); Use Cases, Deployment Scenarios and Requirements**. [S.l.], Apr. 2023. V1.1.1. Available from: <https://www.etsi.org/deliver/etsi_gr/RIS/001_099/001/01.01.01_60/gr_RIS001v010101p.pdf>.

17 WU, Q. et al. Intelligent Reflecting Surface-Aided Wireless Communications: A Tutorial. **IEEE Transactions on Communications**, v. 69, n. 5, p. 3313–3351, 2021.

18 WEN, C.-K. et al. Shaping a Smarter Electromagnetic Landscape: IAB, NCR, and RIS in 5G Standard and Future 6G. **IEEE Control Systems Magazine**, v. 8, n. 1, p. 72–78, 2024.

19 3GPP. **NR; Integrated access and backhaul radio transmission and Reception**. [S.l.], Dec. 2020. v.16.1.0. Available from: <http://www.3gpp.org/ftp/Specs/html-info/38174.htm>. Visited on: 13 Apr. 2021.

20 _____. **New WID on Enhancements to Integrated Access and Backhaul**. [S.l.], Mar. 2021. Meeting no. 91e. Available from: <https://www.3gpp.org/tp/TSG_RAN/TSG_RAN/TSGR_91e/DocsRP-210758.zip>. Visited on: 18 Apr. 2021.

21 POLESE, M. et al. Integrated Access and Backhaul in 5G mmWave Networks: Potential and Challenges. **IEEE Communications Magazine**, v. 58, n. 3, p. 62–68, Mar. 2020. DOI: 10.1109/MCOM.001.1900346.

22 3GPP. **NG-RAN; F1 general aspects and principles (Release 16)**. [S.l.], Apr. 2021. v.16.4.0. Available from: <https://www.3gpp.org/ftp/Specs/archive/38_series/38.470/38470-g40.zip>. Visited on: 18 Apr. 2021.

23 _____. **NR; Backhaul Adaptation Protocol (BAP) specification (Release 16)**. [S.l.], Mar. 2021. v.16.4.0. Available from: <http://www.3gpp.org/ftp/Specs/html-info/38340.htm>. Visited on: 15 Apr. 2021.

24 _____. **NG-RAN; Architecture description**. [S.l.], Sept. 2020. v.16.3.0. Available from: <http://www.3gpp.org/ftp/Specs/html-info/383401.htm>. Visited on: 14 Apr. 2021.

25 MADAPATHA, C. et al. On Topology Optimization and Routing in Integrated Access and Backhaul Networks: A Genetic Algorithm-based Approach. **IEEE Open Journal of the Communications Society**, v. 2, p. 2273–2291, Sept. 2021. DOI: 10.1109/OJCOMS.2021.3114669.

26 SIMSEK, M. et al. Optimal Topology Formation and Adaptation of Integrated Access and Backhaul Networks. **Frontiers in Communications and Networks**, v. 1, p. 1–12, Jan. 2021. ISSN 2673-530X. DOI: 10.3389/frcmn.2020.608088.

27 MADAPATHA, C. et al. **Constrained Deployment Optimization in Integrated Access and Backhaul Networks**. In: PROCEEDINGS of the IEEE Wireless Communications and Networking Conference (WCNC). [S.l.: s.n.], 2023. P. 1–6.

28 CARVALHO, F. I. G. et al. **Genetic Algorithm for Base Station Placement in Integrated Access and Backhaul Networks**. In: PROCEEDINGS of the IEEE Workshop on Communication Networks and Power Systems (WCNPS). [S.l.: s.n.], 2023. P. 1–7.

29 TRAN, Q.-H.; DUONG, T.-M.; KWON, S. Load Balancing for Integrated Access and Backhaul in mmWave Small Cells. **IEEE Access**, v. 11, p. 138664–138674, 2023.

30 GHODHBANE, C. et al. **Load-Efficiency-Balance Cell Selection Policy for IAB Networks**. In: PROCEEDINGS of the IEEE Personal, Indoor and Mobile Radio Communications (PIMRC). [S.l.: s.n.], 2023. P. 1–6.

31 YARKINA, N.; MOLTCHANOV, D.; KOUCHERYAVY, Y. Counter Waves Link Activation Policy for Latency Control in In-Band IAB Systems. **IEEE Communications Letters**, v. 27, n. 11, p. 3108–3112, 2023.

32 LIU, Y.; TANG, A.; WANG, X. Joint Incentive and Resource Allocation Design for User Provided Network Under 5G Integrated Access and Backhaul Networks. **IEEE Transactions on Network Science and Engineering**, v. 7, n. 2, p. 673–685, Apr. 2020. DOI: 10.1109/TNSE.2019.2910867.

33 LEI, W.; YE, Y.; XIAO, M. Deep Reinforcement Learning-Based Spectrum Allocation in Integrated Access and Backhaul Networks. **IEEE Transactions on Cognitive Communications and Networking**, v. 6, n. 3, p. 970–979, May 2020. DOI: 10.1109/TCCN.2020.2992628.

34 LAI, J. Y.; WU, W.-H.; SU, Y. T. Resource allocation and node placement in multi-hop heterogeneous integrated-access-and-backhaul networks. **IEEE Access**, v. 8, p. 122937–122958, July 2020. DOI: 10.1109/ACCESS.2020.3007501.

35 YIN, H.; ROY, S.; CAO, L. Routing and Resource Allocation for IAB Multi-Hop Network in 5G Advanced. **IEEE Transactions on Communications**, v. 70, n. 10, p. 6704–6717, 2022.

36 AN, J.; OU, X. **RL-based Distributed Parametric Resource Allocation Scheme for Multi-Hop IAB Networks**. In: PROCEEDINGS of the IEEE International Wireless Communications & Mobile Computing Conference (IWCMC). [S.l.: s.n.], 2023. P. 1076–1081.

37 SANA, M.; MISCOPEIN, B. **Learning Hierarchical Resource Allocation and Multi-agent Coordination of 5G mobile IAB Nodes**. In: PROCEEDINGS of the IEEE International Conference on Communications (ICC). [S.l.: s.n.], 2023. P. 4218–4223.

38 3GPP. **NR Repeaters**. [S.l.], Mar. 2021. TSG-RAN meeting no. 91e. Available from: <https://www.3gpp.org/ftp/tsg_ran/TSG_RAN/TSGR_91e/Docs/RP-210818.zip>. Visited on: 17 Mar. 2022.

39 XIN, J. et al. **A Survey on Network Controlled Repeater Technology**. In: PROCEEDINGS of the IEEE International Conference on Computer and Communications (ICCC). [S.l.: s.n.], 2022. P. 1097–1101.

40 CARVALHO, F. I. G. et al. **Network-Controlled Repeater - An Introduction**. Jan. 2024. arXiv: 2403.09601 [cs.NI].

41 LEONE, G. et al. **Towards Reliable mmWave 6G RAN: Reconfigurable Surfaces, Smart Repeaters, or Both?** In: PROCEEDINGS of the International Symposium on Modeling and Optimization in Mobile, Ad Hoc, and Wireless Networks (WiOPT). Turin, Italy: [s.n.], Sept. 2022. P. 1–9. DOI: 10.1109/AERO.2015.7118906.

42 AYOUBI, R. A. et al. **Network-Controlled Repeaters vs. Reconfigurable Intelligent Surfaces for 6G mmW Coverage Extension: A Simulative Comparison**. In: PROCEEDINGS of the IEEE Mediterranean Communication and Computer Networking Conference (MedComNet). [S.l.: s.n.], 2023. P. 196–202.

43 GUO, H. et al. **A Comparison between Network-Controlled Repeaters and Reconfigurable Intelligent Surfaces**. Nov. 2022. arXiv: 2211.06974 [cs.NI].

44 DONG, K. et al. **Advanced Tri-Sectoral Multi-User Millimeter-Wave Smart Repeater**. In: PROCEEDINGS of the IEEE Mediterranean Communication and Computer Networking Conference (MedComNet). [S.l.: s.n.], 2023. P. 205–210.

45 SOUSA, D. A. et al. **Beam Squinting Compensation: An NCR-Assisted Scenario**. Jan. 2024. arXiv: 2402.10368 [eess.SP].

46 ETSI. **Reconfigurable Intelligent Surfaces (RIS); Technological challenges, architecture and impact on standardization**. [S.l.], Aug. 2023. V1.1.1. Available from: <https://www.etsi.org/deliver/etsi_gr/RIS/001_099/002/01.01.01_60/gr_RIS002v010101p.pdf>.

47 _____. **Reconfigurable Intelligent Surfaces (RIS); Communication Models, Channel Models, Channel Estimation and Evaluation Methodology**. [S.l.], June 2023. V1.1.1. Available from: <https://www.etsi.org/deliver/etsi_gr/RIS/001_099/003/01.01.01_60/gr_RIS003v010101p.pdf>.

48 TANG, W. et al. Wireless Communications With Reconfigurable Intelligent Surface: Path Loss Modeling and Experimental Measurement. **IEEE Transactions on Wireless Communications**, v. 20, n. 1, p. 421–439, 2021.

49 GOMES, P. R. B. et al. Channel Estimation in RIS-Assisted MIMO Systems Operating Under Imperfections. **IEEE Transactions on Vehicular Technology**, v. 72, n. 11, p. 14200–14213, 2023.

50 GUO, Y. et al. Efficient Channel Estimation for RIS-Aided MIMO Communications With Unitary Approximate Message Passing. **IEEE Transactions on Wireless Communications**, v. 22, n. 2, p. 1403–1416, 2023.

51 MOLAZADEH, A.; MAROUFI, Z.; ARDEBILIPOUR, M. **A Deep Neural Network-based Method for MmWave Time-varying Channel Estimation**. In: PROCEEDINGS of the IEEE International Conference on Information and Knowledge Technology (IKT). [S.l.: s.n.], 2022. P. 1–7.

52 AMRI, M. M. et al. Sparsity-Aware Channel Estimation for Fully Passive RIS-Based Wireless Communications: Theory to Experiments. **IEEE Internet of Things Journal**, v. 10, n. 9, p. 8046–8067, 2023.

53 GINIGE, N. et al. **Machine Learning-Based Channel Prediction for RIS-assisted MIMO Systems With Channel Aging**. May 2024. arXiv: `2406.07387 [cs.IT]`.

54 MUNAWAR, M.; LEE, K. Low-Complexity Adaptive Selection Beamforming for IRS-Assisted Single-User Wireless Networks. **IEEE Transactions on Vehicular Technology**, v. 72, n. 4, p. 5458–5462, 2023.

55 AMIRIARA, H. et al. IRS-User Association in IRS-Aided MISO Wireless Networks: Convex Optimization and Machine Learning Approaches. **IEEE Transactions on Vehicular Technology**, v. 72, n. 11, p. 14305–14316, 2023.

56 XU, H. et al. **Intelligent Reflecting Surface Aided Wireless Networks: Harris Hawks Optimization for Beamforming Design**. In: PROCEEDINGS of the IEEE International Conference on Computer and Communications (ICCC). [S.l.: s.n.], 2020. P. 200–205.

57 IBRAHIM, L. et al. Joint Beamforming Optimization Design and Performance Evaluation of RIS-Aided Wireless Networks: A Comprehensive State-of-the-Art Review. **IEEE Access**, v. 11, p. 141801–141859, 2023.

58 MENG, S. et al. Rank Optimization for MIMO Channel With RIS: Simulation and Measurement. **IEEE Wireless Communications Letters**, v. 13, n. 2, p. 437–441, 2024.

59 LIAN, Z. et al. A Novel Beam Channel Model for AIRS-Assisted Mobile-to-Mobile Communication Systems. **IEEE Internet of Things Journal**, v. 11, n. 7, p. 12307–12318, 2024.

60 CHEN, Y.; CHENG, W.; ZHANG, W. Reconfigurable Intelligent Surface Equipped UAV in Emergency Wireless Communications: A New Fading–Shadowing Model and Performance Analysis. **IEEE Transactions on Communications**, v. 72, n. 3, p. 1821–1834, 2024.

61 LIU, Y.; SARRIS, C. D. Efficient Computation of Scattered Fields From Reconfigurable Intelligent Surfaces for Propagation Modeling. **IEEE Transactions on Antennas and Propagation**, v. 72, n. 2, p. 1817–1826, 2024.

62 MU, X. et al. Simultaneously Transmitting and Reflecting (STAR) RIS Aided Wireless Communications. **IEEE Transactions on Wireless Communications**, v. 21, n. 5, p. 3083–3098, 2022.

63 NDJIONGUE, A. R. et al. Re-Configurable Intelligent Surface-Based VLC Receivers Using Tunable Liquid-Crystals: The Concept. **IEEE/OSA Journal of Lightwave Technology**, v. 39, n. 10, p. 3193–3200, 2021.

64 LI, H.; SHEN, S.; CLERCKX, B. Beyond Diagonal Reconfigurable Intelligent Surfaces: From Transmitting and Reflecting Modes to Single-, Group-, and Fully-Connected Architectures. **IEEE Transactions on Wireless Communications**, v. 22, n. 4, p. 2311–2324, 2023.

65 MOZAFFARI, M. et al. A Tutorial on UAVs for Wireless Networks: Applications, Challenges, and Open Problems. **IEEE Communications Surveys and Tutorials**, v. 21, n. 3, p. 2334–2360, 2019.

66 BANAFAA, M. K. et al. A Comprehensive Survey on 5G-and-Beyond Networks With UAVs: Applications, Emerging Technologies, Regulatory Aspects, Research Trends and Challenges. **IEEE Access**, v. 12, p. 7786–7826, 2024.

67 KURT, G. K. et al. A Vision and Framework for the High Altitude Platform Station (HAPS) Networks of the Future. **IEEE Communications Surveys and Tutorials**, v. 23, n. 2, p. 729–779, 2021.

68 3GPP. **Enhancement for Unmanned Aerial Vehicles (UAVs)**. [S.l.], 2018. v.17.1.0. Available from: <https://www.3gpp.org/ftp//Specs/archive/22_series/22.829/22829-h10.zip>.

69 _____. **Enhanced LTE support for aerial vehicles**. [S.l.], Jan. 2018. v.15.0.0. Available from: <https://www.3gpp.org/ftp//Specs/archive/36_series/36.777/36777-f00.zip>.

70 _____. **Study on supporting Unmanned Aerial Systems (UAS) connectivity, Identification and tracking**. [S.l.], Mar. 2021. v.17.1.0. Available from: <https://www.3gpp.org/ftp/Specs/archive/23_series/23.754/23754-h10.zip>.

71 _____. **Support of Uncrewed Aerial Systems (UAS) connectivity, identification and tracking; Stage 2**. [S.l.], Dec. 2023. v.17.6.0. Available from: <https://www.3gpp.org/ftp/Specs/archive/23_series/23.256/23256-i20.zip>.

72 LI, B.; FEI, Z.; ZHANG, Y. UAV Communications for 5G and Beyond: Recent Advances and Future Trends. **IEEE Internet of Things Journal**, v. 6, n. 2, p. 2241–2263, 2019.

73 DAI, M. et al. Unmanned-Aerial-Vehicle-Assisted Wireless Networks: Advancements, Challenges, and Solutions. **IEEE Internet of Things Journal**, v. 10, n. 5, p. 4117–4147, 2023.

74 TAFINTSEV, N. et al. Aerial Access and Backhaul in mmWave B5G Systems: Performance Dynamics and Optimization. **IEEE Communications Magazine**, v. 58, n. 2, p. 93–99, Feb. 2020. DOI: 10.1109/MCOM.001.1900318.

75 ZHANG, H. et al. **Autonomous Navigation and Configuration of Integrated Access Backhauling for UAV Base Station Using Reinforcement Learning**. In: PROCEEDINGS of the IEEE Future Networks World Forum (FNWF). [S.l.: s.n.], 2022. P. 184–189.

76 WANG, Y.; FAROOQ, J. Deep-Reinforcement-Learning-Based Placement for Integrated Access Backhauling in UAV-Assisted Wireless Networks. **IEEE Internet of Things Journal**, v. 11, n. 8, p. 14727–14738, 2024.

77 _____. **Optimal 3D Placement for Integrated Access Backhauling in UAV-Assisted Wireless Networks Using Reinforcement Learning**. In: PROCEEDINGS of the IEEE International Conference on Mobile Ad Hoc and Smart Systems (MASS). [S.l.: s.n.], 2023. P. 640–645.

78 PARK, H.; NGUYEN, T.-H.; PARK, L. **Federated Deep Learning for RIS-assisted UAV-enabled Wireless Communications**. In: PROCEEDINGS of the International Conference on ICT Convergence (ICTC). [S.l.: s.n.], 2022. P. 831–833.

79 YANG, H. et al. Learning-Based Reliable and Secure Transmission for UAV-RIS-Assisted Communication Systems. **IEEE Transactions on Wireless Communications**, p. 1–1, 2023.

80 TYROVOLAS, D. et al. Energy-Aware Trajectory Optimization for UAV-Mounted RIS and Full-Duplex Relay. **IEEE Internet of Things Journal**, p. 1–1, 2024.

81 LI, J. et al. UAV-RIS-Aided Space-Air-Ground Integrated Network: Interference Alignment Design and DoF Analysis. **IEEE Transactions on Wireless Communications**, p. 1–1, 2024.

82 UNDERSTANDING 3GPP - Starting with the Basics. [S.l.: s.n.]. https://www.qualcomm.com/news/onq/2017/08/understanding-3gpp-starting-basics. Visited on: 2024-04-27.

83 PESSOA, A. M. et al. A Stochastic Channel Model With Dual Mobility for 5G Massive Networks. **IEEE Access**, v. 7, p. 149971–149987, Oct. 2019. ISSN 2169-3536. DOI: 10.1109/ACCESS.2019.2947407.

84 3GPP. **Study on Channel Model for Frequencies from 0.5 to 100 GHz**. [S.l.], Sept. 2017. v.14.2.0. Available from: <http://www.3gpp.org/DynaReport/38901.htm>. Visited on: 26 Sept. 2017.

85 AGYAPONG, P. et al. **Simulation guidelines**. [S.l.], Oct. 2013. Available from: <https://metis2020.com/wp-content/uploads/deliverables/METIS_D6.1_v1.pdf>. Visited on: 20 Sept. 2021.

86 3GPP. **NR; Physical channels and modulation**. [S.l.], Jan. 2020. v.16.0.0. Available from: <http://www.3gpp.org/ftp/Specs/html-info/38211.htm>.

87 DHALMAN, E.; PARKVALL, S.; SKOLD, J. **5G NR The Next Generation Wireless Access Technology**. 2. ed. [S.l.]: Mara Conner, 2021. ISBN 978-0-12-822320-8.

88 MONTEIRO, V. F. **Addressing 5G enhanced mobile broadband and lean signaling based on dual-connectivity and channel hardening occurence**. 2018. PhD thesis – Federal University of Ceará.

89 DHALMAN, E.; PARKVALL, S.; SKOLD, J. **4G: LTE/LTE-Advanced for Mobile Broadband**. 2. ed. [S.l.]: Elsevier Science, 2014. ISBN 978-0-12-419985-9.

90 3GPP. **NR; Physical layer measurements**. [S.l.], Sept. 2018. Available from: <http://www.3gpp.org/ftp/Specs/html-info/38215.htm>. Visited on: 15 Oct. 2018.

91 FANTACCI, R. et al. Adaptive modulation and coding techniques for OFDMA systems. **IEEE Transactions on Wireless Communications**, v. 8, n. 9, p. 4876–4883, 2009.

92 3GPP. **NR; Physical layer procedures for data**. [S.l.], Dec. 2017. v.15.0.0. Available from: <http://www.3gpp.org/ftp/Specs/html-info/38214.htm>.

93 _____. **Study on Vehicle-Mounted Relays; Stage 1 (Release 18)**. [S.l.], Sept. 2021. v.18.0.0. Available from: <http://www.3gpp.org/ftp/Specs/html-info/22839.htm>. Visited on: 20 Oct. 2021.

94 _____. **Study on Channel Model for Frequencies from 0.5 to 100 GHz**. [S.l.], Mar. 2022. v.17.0.0. Available from: <http://www.3gpp.org/DynaReport/38901.htm>. Visited on: 26 Sept. 2017.